Aberystwyth University

Doctoral Thesis

Numerical simulation of surfactant motion in flowing foams and application to biological tissues

Candidate:
Francesca Zaccagnino

Supervisor:
Prof Simon Cox

Department of Mathematics

2019

Declaration

Word count of thesis: _____

This work has not previously been accepted in substance for any degree and is not being concurrently submitted in candidature for any degree.

Candidate Name: Date: Signed:

_____ _____ _____

This thesis is the result of my own investigations, except where otherwise stated. Where correction services[1] have been used, the extent and nature of the correction is clearly marked in a footnote(s).

Other sources are acknowledged by footnotes giving explicit references. A bibliography is appended.

Candidate Name: Date: Signed:

_____ _____ _____

I hereby give consent for my thesis, if accepted, to be available for photocopying and for inter-library loan, and for the title and summary to be made available to outside organisations.

Candidate Name: Date: Signed:

_____ _____ _____

[1] this refers to the extent to which the text has been corrected by others

"Panta rhei"

Summary of the Thesis

Department of Mathematics

Doctor of Philosophy

Numerical simulation of surfactant motion in flowing foams and application to biological tissues

by Francesca Zaccagnino

We present a numerical model to study the rheology of two-dimensional dry foams. In a foam flowing at high velocity, the tangential component of the velocity associated with the gradient of surfactant concentration is not negligible. We develop a dynamical model to investigate the influence of viscoelastic parameters on the film evolution. Particularly, we consider the surfactant transport and the consequent surface tension variation along each film. Moreover, experiments on a foam between two parallel plates suggest that the diffusion of curvature along the film controlled by external friction can not be neglected. Hence, we merge our surfactant transport (ST) model with the two-dimensional Viscous Froth (VF) model [45]. The VF+ST model is validated by fitting experimental data for the evolution of the length of a film after a topological rearrangement (T1). Extending the VF model, which allows us to estimate the drag coefficient, our VF+ST model predicts two additional parameters, the Gibbs elasticity and the surface viscosity. With the VF+ST model we can fit experimental data for both foam containing anionic surfactants or proteins [74].

Furthermore, we apply the VF+ST model to predict rheological parameters of a flowing two-dimensional dry foam. We implement situations in which hexagonal and disordered foams subjected to simple shear or oscillating strain. We highlight how the viscoelastic parameters of our model affect the distribution of topological rearrangements in the foam. Additionally, we calculate the shear

stress which offer a qualitative description of the transition of the foam from a solid-like to a liquid-like behaviour. Hence, starting from the stress-strain curves at different shear rates we predict the elastic shear modulus and the yield stress of the foam. In case of oscillating strain we investigate how the foam behaviour changes when varying the frequency or the amplitude of the applied strain and we calculate the storage and loss moduli. Overall, we analyse the effect of the viscoelastic parameters of our model on the rheological properties of the foam.

Finally, the model is applied to investigate the morphology of biological tissues. Well-known analogies between fluids and biological tissues make possible the application of our model to simulate experiments presented by Bonnet *et al.* [6]. They carried out an annular ablation on *Drosophila* pupa dorsal thorax epithelium. In agreement with the experimental results we find that after cutting the cell-cell junctions and relaxing the tissue to its configuration of mechanical equilibrium, the anisotropy in the tissue increases with the age of the *Drosophila* pupa. Also in this case we investigate the effect of our viscoelastic parameters on the tissue. We propose our model as a tool for further investigations on tissue morphology.

Note: The material of Chapter 2 has been published in the scientific journal *Physical Review E* [74].

Contents

Chapter 1

Introduction

Milkshakes, shaving cream and mayonnaise are all dispersions of one fluid in another. In particular, a foam is a dispersion of a gas in a liquid: the gas occupies most of the volume while the liquid constitutes the continuous network of soap films and their connections. The liquid contains surfactant molecules which arrange themselves at the gas/liquid interface, reducing the surface tension and stabilizing the same film. By changing either gas, liquid or surfactant molecules it is possible to create foams with different properties. The choice of gas or liquid, for example, can affect the ageing of the foam, and the surfactant molecules, with their particular chemical affinity for specific materials, can lead to foams suitable for a number of applications, from detergent products to mineral separation methods.

1.1 Foam applications

A foam is less dense than a liquid, so it can fill the same volume with less material and therefore lower costs. During the industrial process of cleaning, for example, treating materials with foam rather than liquid allows not only to reduce on production costs but also to dry quickly the material. Furthermore, the foam presents a large surface area per unit volume therefore, using only few grams of liquid, it is possible to generate foams with several square metres of interface. The extensive interface gives the foam various properties, for example, it is able to refract and reflect light in all directions and also to slow down sound propagation [15].

From a mechanical point of view, a foam behaves differently from the gas and liquid phases which constitute it. Foams are therefore classified as complex fluids. They can either behave like a solid, exhibiting viscoelastic or plastic deformations, or they can act like a liquid. In the latter case the foam can be used to fill cavities or to coat fibres and it can flow through veins or artificial tubes of different shapes reducing frictional losses in comparison with liquids.

Their lightness and all the other properties briefly summarized above make foams suitable for several application fields from the food industry to the medicine field.

The overall study of a foam requires a *multi-scale* approach. It is necessary to consider the foam scale, the film scale and also the scale at surfactant level, as it is sketched in Figure 1.1. From a macroscopic

point of view the foam is a solid with a certain volume; moving to a millimetre scale the bubbles can be distinguished and the geometrical and physical laws, which drive the packing of bubbles, have to be considered. Moreover, the micron and nanometre scales are equally important considering the liquid distribution in the soap films, the chemistry and the influence of the surfactant molecules on the stability of the gas/liquid interfaces and the related dissipation phenomena.

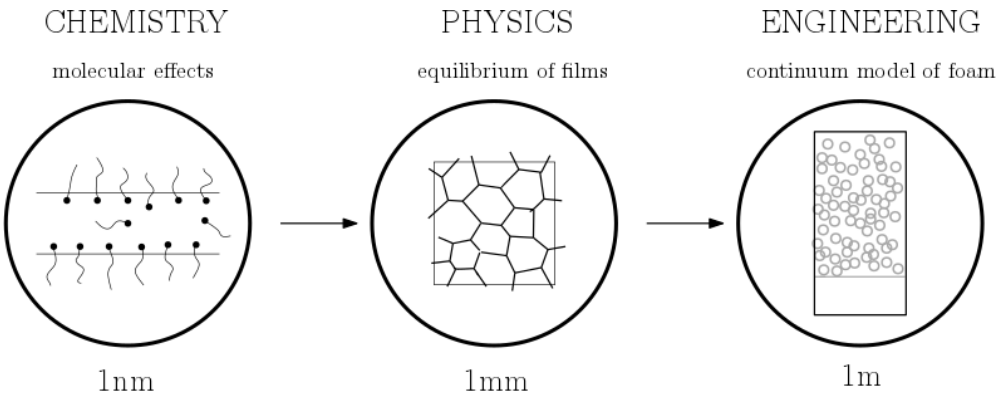

FIGURE 1.1: Multi-scale approach to foam study [71].

1.1.1 Why are flowing foams interesting?

Many foam applications are dedicated to food products, from the head on a beer to ice cream, which presents a more complex and variable structure and constitutes at the same time a foam and an emulsion. Nevertheless, a number of companies from different fields share the same interest: to achieve a deeper understanding about foam flow in order to produce not only softer ice cream but also to recover oil with greater efficiency.

In terms of oil recovery, the use of pressurized liquid to inject a geological formation and force out the oil can address limitations such as viscous instability or gravity override. Hence, standard techniques of oil recovery inject fluid less viscous than oil, implying the possibility of fingering phenomena[34], or rather, the creation of fluid fingers that penetrate through the oil. On the other hand, the injection of gas, which is less dense than the oil, may cause different challenges. The gas, for example, may rise to the top of the reservoir and consequentially override the oil. As a consequence, both viscous instability and gravity override reduce the efficiency of the oil recovery process. On the contrary, using foams the goal of increasing the percentage of oil swept during the process of oil recovery can be achieved. Moreover, through foams the interfacial tension forces are reduced using lower amount of chemicals and therefore, a huge reduction of process costs is realized.

Grassia *et al.* [34] developed a pressure-driven growth model to study the foam front of propagation during oil recovery processes. They investigated the shape of the foam front and found that the more uniform the foam front smaller the un-swept area in the oil reservoir. Nevertheless, the problem involves many variables, a complete understanding of the matter is still missing and foam properties for these type of applications need to be investigated further.

Moreover, flowing foam are also applied in medical field. There are, for example, endovenous microfoams to treat varicose veins. For such applications a sclerosant drug is mixed with air or a physiological gas (carbon dioxide) in order to create the microfoam that indeed constitutes

a treatment with lower concentrations of sclerosant [16]. Thanks to its physical and chemical characteristics the microfoam is able to push the blood further and act on the vein walls restoring them. Carugo *et al.* [16] explained the influence of rate of absorption of the foam, they also investigated the bubble size and the drainage process which stabilize the foam, although, also in microfoams viscous instability may happens.

Overall, a further understanding of the properties of flowing foams, which are defined through the shear modulus and the yield stress, as we explain in Chapter 3, requires a deeper investigation.

1.1.2 Biological tissue

In addition to natural and artificial foams other matters with similar structures exist. Cork, for example, is a natural solid foam, it is a highly anisotropic material, which presents a non-linear mechanical response when subjected to stress or strain. Its mechanical characteristics makes this material suitable for the wine industry.

Furthermore, biological cellular tissue exhibits structures very similar to foams. Particularly, any two-dimensional cellular tissue presents three-fold junctions and although foams do not exhibit division processes, the same type of numerical simulations are usually applied to study the growth and the sorting process of the tissue [71]. Bonnet *et al.* [6] investigated the *Drosophila* pupa dorsal thorax epithelium. They carried out a laser ablation of an circular region and they measured the relaxation time as well as the anisotropy of the stain and the stress to viscosity

ratio for the ablated area. Moreover, Rauzi *et al.* [61] explained the behaviour of the ablated junctions highlighting the correlation between the forces acting at the junction, right before and after the ablation, with a constant drag coefficient. Bonnet [6], applied the same considerations and developed a continuous linear visco-elastic model in order to estimate the relation between viscosity and friction starting from the tissue morphology.

In the literature there are several works where the tissue morphology is simulated through foam models, in particular vertex models [29] and Potts models [8, 24], which we describe respectively in Sections 1.4.2 and 1.4.1.3. As Bosveld *et al.* [8] showed, the Potts can describe cell-cell contact regulations taking into account the tension at the cell junctions. The Potts simulation supports the idea that mechanical tension is an important regulator of cell growth and proliferation, opening inspiring possibilities to the further study of cell tissue morphology.

1.2 Local equilibrium rules and general physics of foams

At the film scale a foam respects well known equilibrium laws, which describe the specific local structure. The condition of mechanical equilibrium is realized at a macroscopic level when all the components of forces and tensions acting in the foam are balanced and the foam reached a

steady state configuration. Here we offer a brief overview of the principal foam physical laws.

1.2.1 Laplace-Young Law

Of fundamental importance in the study foams is the surface tension γ. Considering an homogeneous liquid the work to create a new surface is proportional to the number of molecules brought from the liquid bulk to the liquid surface. The constant of proportionality between this work and the increase of surface area has the dimensions of a force per unit length and it is called surface tension. The surface tension is therefore strictly correlated to the bubble shape and the Young-Laplace law indeed expresses the correlation between the mean curvature of the interface and the drop of pressure, ΔP, across the same interface [15, 71]

$$\Delta P = \frac{2\gamma}{r} \qquad (\text{in} \quad 2D). \tag{1.1}$$

Figure 1.2 illustrates a two dimensional foam at equilibrium, the relation between the drop of pressure across the film, the curvature and the interfacial tension of the same film are represented.

Moreover, at the interface scale the surfactants have a significant role, their characteristic hydrophilic head and hydrophobic tails act on the interface properties. In particular, the thickness of the soap film decreases until the electrostatic repulsion and the Van Der Waals attraction, between the surfactant molecules, become equal. This interaction constitutes the disjoining pressure which ensures the mechanical equilibrium

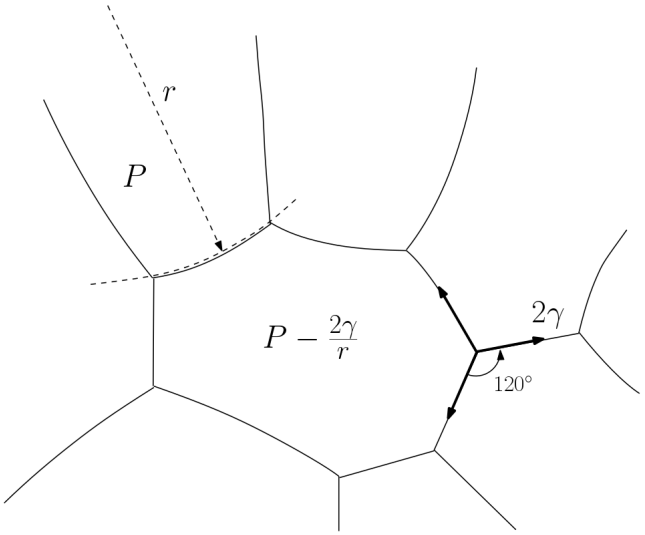

FIGURE 1.2: Laplace-Young law representation [71].

of the film and therefore its existence. Hence, the disjoining pressure prevents the film from shrinking to zero thickness and it generally has to be included in the equilibrium condition.

Nevertheless, in the present work we focus on dry foams whose film thickness is neglected and as a consequence the disjoining pressure plays no explicit role.

1.2.2 Plateau's Laws

The Plateau borders are the channels at the junctions between three edges where most of the foam liquid is concentrated. The Young-Laplace law allows the evaluation of the Plateau border cross section, which is sketched in Figure 1.4, considering the pressure P_{Pb} within the Plateau

border. This pressure, P_{Pb}, is much lower than the pressure within the bubbles.

In the dry limit the amount of liquid in the Plateau border is negligible and Plateau's laws add further essential rules to define the equilibrium configuration of the foam. Plateau's laws assert that the films of a dry foam can only meet threefold forming an angle of 120° between each other. Moreover, at each vertex no more than four edges, or six surfaces may meet creating a symmetric tetrahedral vertex, as is shown in Figure 1.3, where the arising angle of 109.5° is also indicated [15, 71].

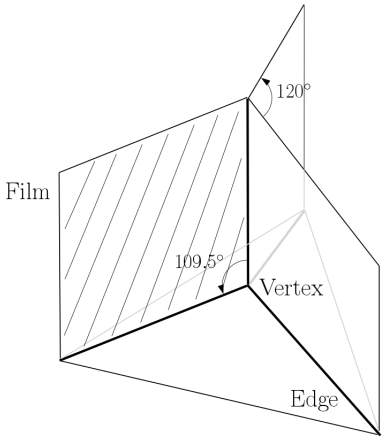

FIGURE 1.3: Tetrahedral vertex where four bubbles meet. Particularly, the four edges and six films, which converge at the same vertex are sketched. The characteristic angles of 109.5∘ at the vertex and 120∘ between the films are also indicated [71].

Furthermore, Plateau introduced an additional equilibrium rule concerning wet foams. He observed that a Plateau border joins smoothly the adjacent film creating a sharp cusp. This last consideration together with the Laplace-Young law, leads to the decoration theorem: a dry

foam structure can be decorated by a Plateau border at each threefold vertex in order to create an equilibrated wet foam structure. The theorem, whose validity is limited to the two-dimensional foam, has been applied to simulate wet foams [71].

1.2.3 Coarsening

The present work is focused mostly on two-dimensional dry foam. As mentioned, three films meet at Plateau borders, which in two-dimensional dry foam are simply vertices. Euler's law relates the numbers of polygonal bubbles P, edges E and vertices V by a precise rule, in the case of two dimensional foam: $P - E + V = 1$ [71]. According to Plateau's law each vertex is a threefold junction of three edges, moreover, every edge connects two vertices. It follows that $E = (3/2)V$ and as a consequence an infinite two-dimensional foam presents on average six sides per bubble.

Coarsening is driven by the difference in pressure between adjacent bubbles. In general each film is curved and bubbles with lower pressure are surrounded by concave films. Moreover, from Plateau's law it follows that convex bubbles must have fewer than six sides. On the other hand, a honeycomb foam, made up of hexagonal bubbles, presents straight edges, it means that the pressure within each bubble has to be equal and no diffusive coarsening happens. By contrast, in disordered foams the drop of pressure across the films drives a diffusion of gas from the convex bubbles to the concave ones. Von Neumann's law relates the rate of growth of the area A for a polygonal bubble of n sides with the coefficient of diffusion of gas in liquid, k_d:

$$\frac{dA_n}{dt} = k_d(n-6). \tag{1.2}$$

As a consequence, the convex bubbles shrink while the concave ones grow. In the present work we neglect coarsening, therefore the area of each bubble is kept constant.

1.2.4 Foam liquid fraction

A very important parameter generally used to classify foams is the liquid (or continuous phase) fraction ϕ_l, which refers to the proportion of liquid within the foam. When the liquid fraction is above a critical value of $\phi_l = 16\%$ the foam behaves as a bubbly liquid [4]. Contrarily the dry limit is defined as $\phi_l < 5\%$. As already mentioned, most of the liquid is contained in the Plateau borders, or rather the concave channel which is sketched in Figure 1.4.

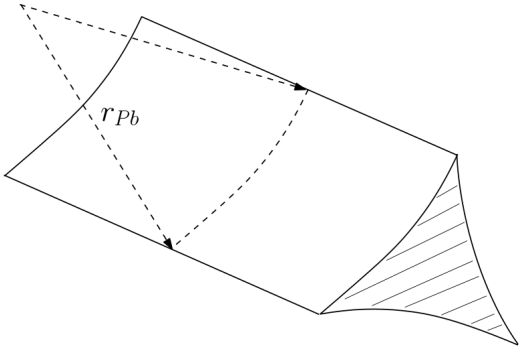

FIGURE 1.4: Representation of the Plateau border, where three films meet, the cross section is a concave triangle [71].

Knowing the radius of curvature r_{Pb} the cross section area of the Plateau border is calculated as follows [71]:

$$A_{Pb} = \left(\sqrt{3} - \frac{\pi}{2}\right) {r_{Pb}}^2. \tag{1.3}$$

In case of a two-dimensional foam with n bubbles of area A_n, the liquid fraction can be defined as the ratio between the area occupied by the liquid and the total bubble area $A_{tot} = nA_n$. In the previous section we mentioned that each bubble has, on average, six edges and each vertex is shared between three edges. It follows that the area occupied by the liquid is defined as $A_l = 2nA_{Pb}$ and the area of the Plateau border cross section is given by

$$\phi_l = \frac{A_l}{A_{tot}} = (2\sqrt{3} - \pi)\frac{{r_{Pb}}^2}{A_n}. \tag{1.4}$$

Whenever the study is restricted to a dry foam, A_n is approximated as the average area of the bubbles while the radius of the Plateau border is related to the minimum film length at which a topological rearrangement may happen.

Moreover, the localization of liquid within the foam is affected by an additional factor: drainage. Foam drainage describes the flow of liquid through the foam, which is driven by gravity and capillarity. Together with the other phenomena at surfactant level scale, drainage highly affects the foam stability as it leads to thinner films which are more likely to break and for the coarsening process to happen at a faster rate. Considering drainage is therefore very important for many industrial foam applications [40].

1.2.5 Two-dimensional experimental foam sample

A two-dimensional froth can be easily realized between two plexiglass plates with fixed separation [15]. Looking at the foam from the top it is possible to observe a two-dimensional foam, despite the experimental sample contains a quasi-three-dimensional foam, as shown in Figure 1.5. Hence, beyond the dynamics of the two-dimensional top view, the experiment allows the observation of the film thickness and its variations due to drainage phenomena. Nevertheless in the present work we neglect the film thickness and drainage, and we analyse the two-dimensional top view.

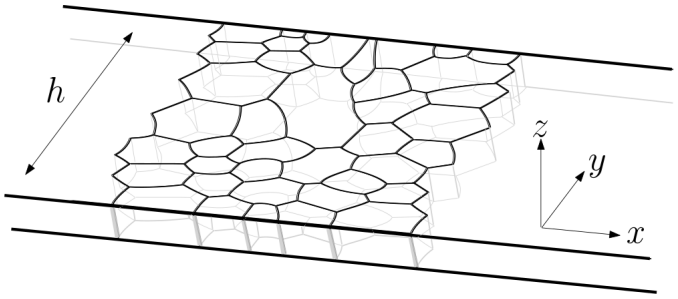

FIGURE 1.5: Dry foam between two plexiglass plates. Because the height between the two plates is much smaller than the plate width, we can treat the system as a two-dimensional one.

In Chapter 2 we describe an experiment realized with a simple dedicated device by collaborators from the INRA. We looked in particular at the elementary case of five films between two flat plates. The experiment has been carried out very carefully in order to allow the drainage of the liquid ensuring the stability of the five films. The five films observed at equilibrium are straight as a consequence of the atmospheric pressure acting on

both sides of the film. Nevertheless, the experiment shows that during the transition from an out of equilibrium configuration to an equilibrium configuration the lateral films exhibit a slight curvature. The curvature is due to the friction between the films and the plexiglass plates which, particularly in this type of experiments, can not be neglected, as also Langois *et al.* highlighted [48]. As a consequence, models which involve the drag coefficient are more appropriate in order to build a predictive tool able to analyse the foam behaviour.

1.3 Foam rheology

It has been known for a century that there are some materials which do not belong to the classical scheme of materials classification [49]. These particular materials are named complex fluids and present properties which are intermediate between ordinary solids and ordinary liquids, known as Newtonian fluids.

The relationship between stress and deformation in such materials is in many cases nonlinear and scalar parameters as viscosity and elastic modulus are not enough to describe accurately their mechanical properties [49]. In general these substances behave as elastic solids at short strains and liquids at larger strains, when eventually they start to flow and they are therefore called viscoelastic.

Another important distinguishing characteristic of complex fluids is their possibility to exhibit both isotropic and anisotropic behaviour. This is in

contrast, for example, to Newtonian fluids, which are defined as isotropic because they present mechanical properties independent of the orientation of the applied deformation. Examples of complex fluids include glass-forming liquids, polymer and micellar solutions as well as foams, emulsions and biofluids [49]. Blood is an example of biofluid: it is a suspension containing blood cells which act similarly to elastic solids or liquids as a function of the shear rate.

Rheology is the study of the flow of matter, as suggested by the word's etymology, from Greek $\rho\varepsilon\omega$ *-rhéō*, "flow" and $\lambda o\gamma\iota\alpha$ *-logia* , "study of". Similarly, a rheometer is the device to measure the rheological properties of complex fluids as a function of rate or frequency of deformation. Through a rheometer it is possible to impose a shear flow and measure the resulting stress or alternatively, to impose the shearing stress and measure the resulting deformation.

A foam, on a macroscopic scale, is defined as a complex fluid, it exhibits elasticity, plasticity and viscosity in relation to the applied stress, σ, or strain-rate, $\dot{\varepsilon}$. Hence, at small deformations the foam behaves as an elastic material and bubbles, which are elongated or squeezed due to application of strain or stress, can move back to their original shape. On the other hand, when the strain increases further the foam exhibits topological rearrangements, which are effectively plastic events. Figure 1.6 shows typical topological rearrangements within two-dimensional foams, such as the swap of neighbouring bubbles, known as a T1, or the collapse of a bubble which shrinks until disappearing, known as T2.

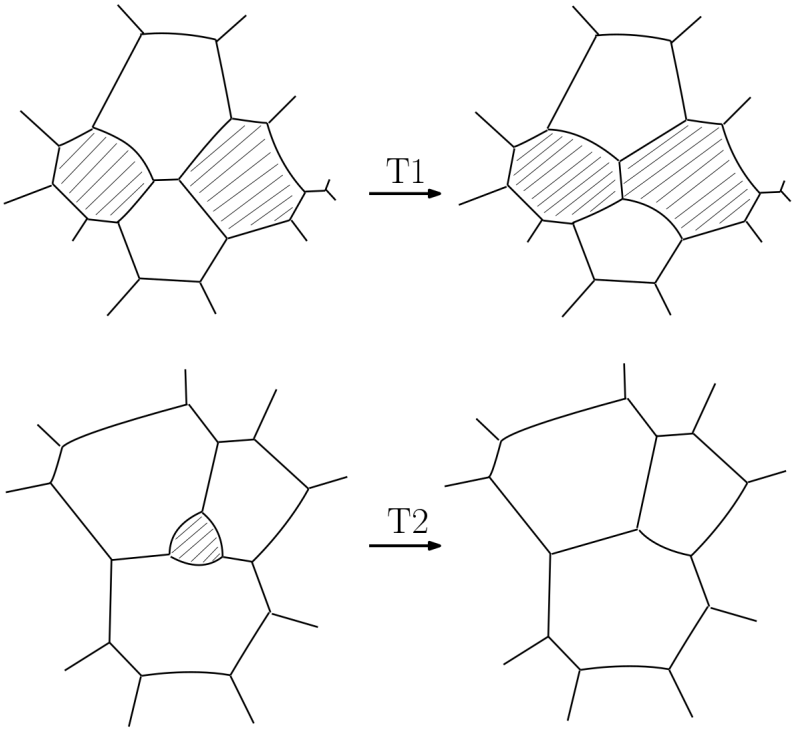

FIGURE 1.6: Representation of the topological rearrangements, T1 above and T2 below [71].

1.3.1 Dissipation mechanisms in foams

Foam rheological properties are affected by the interplay between dissipative processes and elastic storage mechanisms. How these two ingredients interact is still a matter of discussion. Buzza *et al.* [12] offered a detailed overview of the various mechanism of viscous dissipation in foams. They described viscous flow of liquid in films and Plateau borders, the intrinsic viscosity of the surfactant layer as well as the dissipation associated with the Marangoni effect. As explained by Edwards *et al.* [27], the Marangoni

effect consists of a convective surfactant transport within the foam film, in response to a surface tension gradient. Moreover, many other phenomena influence the film properties. When the interface is subjected to expansion or compression a flux of surfactant molecules between the interfacial layer and bulk arises. Generally, the adsorption-desorption phenomena last until an equilibrium configuration is reached.

In Chapter 2 we highlight that, within a film, diffusion generally happens much more slowly than convection. On the other hand, the surfactant molecules move not only across the bulk but also along the thin layer at the interface, for example as a consequence of stretching or shrinking deformations of the film. In the present work we look particularly at dissipative effects at the interfacial layer, introducing a surfactant drag coefficient which locally affects the film dynamics.

1.3.2 Rheological measurements

Fundamental to the analysis of rheological materials is the definition of the shear modulus and the yield stress, as explained by Weaire *et al.* [71], which leads to the calculation of the characteristic shear viscosity.

1.3.2.1 Shear viscosity

The simplest geometry for studying a shearing flow is a system of sliding plates, or rather a plane Couette geometry, see Figure 1.7

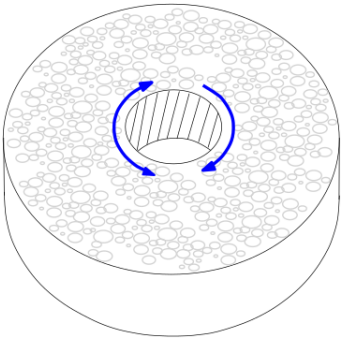

FIGURE 1.7: Couette geometry, this experimental set up allows the study of ether simple shear or oscillating shear imposing a different direction of rotation as indicated by the blue arrows [71].

In such systems the shear rate, $\dot{\varepsilon}$, is the ratio between the velocity of the moving plate and the gap between the two plates. The shear stress, σ, is the force per unit area exerted by the flowing foam on the plate surface. As a consequence, the shear viscosity, η, is defined as the ratio $\sigma/\dot{\varepsilon}$ [49]. The shear viscosity is a material property which measures the fluid's resistance to flowing. Differently from Newtonian fluids, complex fluids also exhibit elastic properties and in addition to the shear viscosity, they require a larger number of strain-rate dependent material properties in order to be characterized. Hence, we introduce in the following sections the shear modulus and the yield stress.

1.3.2.2 Storage and loss moduli

Another measurement to explore the influence of structure on the flow of complex fluids can be realized by imposing a small amplitude oscillatory strain. A sinusoidal strain is defined as $\varepsilon(t) = \varepsilon_0 \sin(\omega t)$, where ω is

the frequency of the oscillation in units of radians per seconds. When the strain amplitude ε_0 is small enough the deformation of the foam is elastic and consists in spontaneous relaxation of films. The shear stress generated on the foam also varies sinusoidally with time and its amplitude is proportional to the amplitude of the applied strain ε_0. In general the stress can be calculated as

$$\sigma(t) = \varepsilon_0[G'(\omega)\sin(\omega t) + G''(\omega)\cos(\omega t)]. \tag{1.5}$$

The term G' is called the storage modulus and it is in phase with the strain, while the term G'' is in phase with the rate of strain $\dot{\varepsilon}$ and is called the loss modulus. These two terms represent respectively the storage of elastic energy and the viscous dissipation of the same energy [49]. Figure 1.8 shows their prototypical trend in case of liquid-like and solid-like complex fluids. In case of solid-like materials $G' \gg G''$ and G' is almost

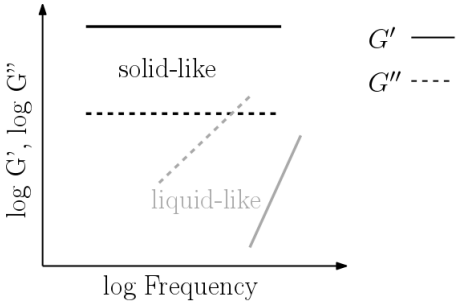

FIGURE 1.8: Characteristic trend of storage and loss moduli against frequency in case of solid-like and liquid-like complex fluids [49].

independent of the frequency, in contrast to liquid-like fluids which exhibit $G'' \gg G'$. Nevertheless, real complex fluids usually show behaviour intermediate between solid-like and liquid-like. Furthermore, real data

often present a crossover between the two moduli, where $G' = G''$. It is a detectable point which corresponds to the shift from a steady state shear viscosity towards a shear thinning region. The crossover strain rate $\dot{\varepsilon}_c$ may happen to be numerically very similar to the crossover frequency ω_c and they are both approximately equal to the inverse of the fluid's relaxation time τ, or rather the time necessary for the elastic structure in the fluid to relax [49].

In Figure 1.9 we report the shear modulus measured for the Gilette shaving cream [17]. The different symbols in Figure 1.9 corresponds to different ages of the foam, due to the coarsening the size of the bubbles increases with the time and the shear modulus drops. As we explain in Chapter 3, thanks to numerical simulations we can not only reproduce experimental data but also make predictions considering a range of parameters which are otherwise difficult to measure experimentally.

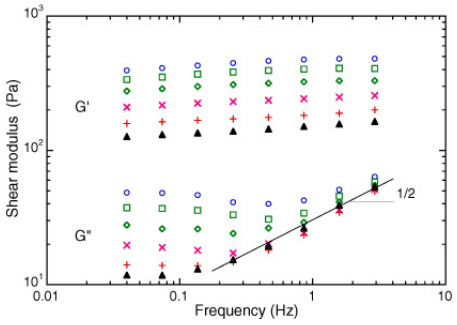

FIGURE 1.9: (From [17]) Shear modulus for the Gilette shaving cream versus frequency. The samples evolve due to coarsening and a sinusoidal shear stress of amplitude much smaller than the yield stress is applied. The symbols corresponds to different foam ages, from 15 min for the circles to 8 h for the triangles.

1.3.3 Yield stress

When a complex fluid is subjected to high stresses a process known as yielding or plastic deformation can occur. Yielding occurs above a yield stress, σ_Y, which depends weakly on strain rate $\dot{\varepsilon}$, temperature and other parameters such as liquid fraction and polidispersity. In the present work we completely neglect temperature effects, while we present in Chapter 3 our results and considerations concerning the relationship between σ_Y and $\dot{\varepsilon}$ in the presence of surfactant motion.

In theory, below σ_Y the material should deform reversibly. Nevertheless there are experiments which highlight the possibility of plastic deformations also at low stress [22]. On the contrary, above the yield stress the deformations can be only partially recovered, and the material therefore deforms irreversibly.

Figure 1.10 shows an idealised stress-strain curve, when a shear strain is applied to a liquid foam. Above σ_Y the stress drops during a phase called strain softening and then it may level out in a plateau value.

As mentioned, plastic events in foams consist of topological rearrangements. It may happen that the strain is not homogeneously distributed but localized to specific slip planes. Overall, we can define σ_Y as the stress that allows the foam to start flowing while the stress at the plateau is the stress that allows the foam to keep flowing.

A flowing foam can be modelled by means of the Bingham equation, $\sigma = \sigma_Y + \eta_P \dot{\varepsilon}$ which leads to evaluating the effective viscosity or rather the ratio between the applied shear stress σ and the strain rate ε.

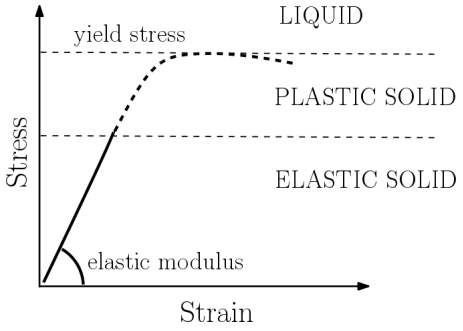

FIGURE 1.10: Characteristic stress-strain for a liquid foam, when an increasing shear strain is applied [71].

In case of foam also the Herschel-Bulkley constitutive equation is commonly used; It introduces a power law exponent, β, to the shear rate, $\sigma = \sigma_Y + \eta_P \dot{\varepsilon}^{\beta}$. In Chapter 3, we describe our results by applying the Herschel-Bulkley equation to fit our numerical data.

Nevertheless, the definition of the yield stress σ_Y in foams is still a source of controversy within the foam community; we discuss this later in the context our results.

1.4 Current numerical models for simulating disordered foam structure and dynamics

Although many techniques are available to simulate foams, there are still open questions to investigate in order to explain thoroughly foam behaviour. Through numerical simulations it is possible to study both dry

and wet foams on multiple levels. The position and shape of individual bubbles as well as the overall velocity profile and pressure gradient for a cluster of bubbles flowing in a channel can be traced. These data are useful to carry out statistics of foams and to analyse the characteristics of elasticity and plasticity within the foam. The available simulation methods allow to visualize and analyse additional information in order to study foams and other soft matter which display similar behaviours. In the following sections we briefly describe some of the numerical simulation techniques that have been developed for foams.

1.4.1 Quasi-static simulations

In a quasi-static simulation the foam evolves through a sequence of equilibrium configurations. The main assumption is that the gas in the foam is incompressible and the time-scale associated with the relaxation of equilibrium is faster than the time-scale associated with any external forcing. Moreover, the surface energy, or rather the tension, γ, is assumed to be constant everywhere and viscous dissipation is negligible [44]. Here we briefly describe the most popular models.

1.4.1.1 Surface Evolver

The idea has been implemented by Brakke [9], who created an open source software called Surface Evolver. The software can be use to simulate quasi-static two-dimensional and three-dimensional foams. It allows more

variation in terms of constraints and boundary conditions than other models and has been widely applied by the whole foam community.

The equilibration of the foam is driven by the local minimization of the surface energy E which can be calculated as the total film length, $\sum_k l_k$, or the total surface area, respectively in the case of two-dimensional and three-dimensional foams:

$$E = 2\gamma \sum_k l_k + \sum_k p_k (A_k - A_{k'}), \tag{1.6}$$

where p_k, A_k and A'_k are the pressure, the current area and the target area for each bubble k respectively.

In the literature there are many works realized using Surface Evolver, which analyse the structure of monodisperse and polydisperse foams [47], investigate simple shear flow [63], look at the flowing of foam past one or more obstacles [19] or study the sedimentation of discs in a two-dimensional foam [20].

1.4.1.2 2D-froth and PLAT

Kermode and Weaire [44] developed the model "2D-froth", matching restrictions on curvature to investigate foam rheology. The model, which uses a Voronoi construction [10] to generate the starting foam configuration, has been then extended to the case of wet foams with the PLAT code [5]. In the case of wet foams an extra variable, the pressure within the Plateau borders, has to be considered. In order to generate the wet

foam they apply the decoration theorem, which we mentioned in Section 1.2.2: they simply modified the Voronoi network used for the dry foam, replacing each vertex with a small three-sided Plateau border.

The equilibration process is simulated by iteration. At each step the coordinates of vertices and the pressure within each bubble are updated in order to satisfy the equilibrium laws described in previous sections.

Both the models, for dry and wet foams, involve topological rearrangements (T1s), which are trigged when the distance between two vertices is shorter than a critical minimum value.

1.4.1.3 The Potts method

The Potts is a stochastic method which allows fast computations providing good statistical data. Thanks to its simplicity this technique has become common to simulate cellular patterns either in physics or biology. The two-dimensional version of the model, developed to study foam rheology [41, 72], discretizes a continuous cellular pattern onto a discrete square lattice. An integer i, chosen from the set $(1, .., n)$, is defined at each lattice site, k, in order to label the n bubbles, as shown in Figure 1.11. The equilibration of the model is driven by the local energy minimization as in the quasi-static model. The Hamiltonian for the model is

$$H = J \sum_{sites\ k,l} (1 - \delta_{\sigma_k,\sigma_l}) + B \sum_{bubbles\ i} (A_i - A_{i_0})^2. \tag{1.7}$$

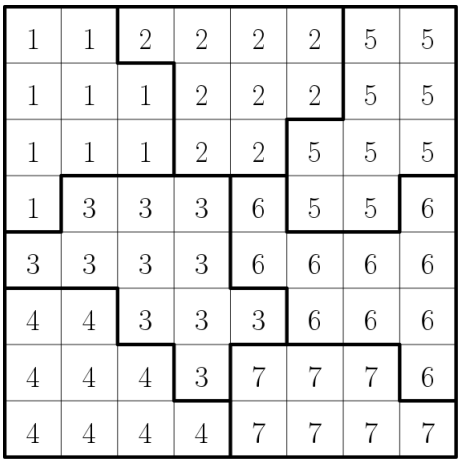

FIGURE 1.11: Representation of a two-dimensional foam by division of a square lattice with index values i = (1, 2, 3, 4, 5, 6, 7), thus 7 bubbles are shown.

The first sum is over neighbouring sites, k and l, representing the surface energy, where J is a coefficient proportional to the surface tension [24]. During the equilibration a randomly-chosen lattice point is randomly assigned the value of one of its nearest neighbours. If the change in surface energy $\delta_{\sigma_k,\sigma_l}$, which is calculated from the different cell boundaries of old and new configurations, is less than or equal to zero, the new configuration is kept. Otherwise, there is a probability of $\exp(-\delta_{\sigma_k,\sigma_l}/k_BT)$ that the new configuration is kept, where k_B is Boltzmann's constant and T the temperature of the system [72]. The second sum represents the area constraint and it is carried over all the bubbles. The term A_{i_0} is a target area for each bubble i.

Due to its simplicity and high simulation speed this model is often used to study foams with a large number of bubbles [24]. It also allows to

incorporate parameters such as temperature and to carry out direct measurements of T1 events, as well as study the two-dimensional foam flow around a circular obstacle [59]. Nevertheless, the model provides a representation of the foam which is less accurate than the one obtained through other models.

Despite quasi-static models have been proved to be a powerful tool to investigate foam rheology, moving to foam flowing at higher velocities, as for example microfluidic foams which flow in narrow channels, quasi-static models are not enough [13]. In such applications the viscous effects are not negligible therefore different kind of models have been developed.

1.4.2 The Vertex Model

The vertex model describes a two-dimensional dry foam through the motion of n vertices. The model considers a set of position vectors p_i for the vertices, which are connected to the three nearest vertices with straight edges, as shown in Figure 1.12. The vertex equation of motion involves both frictional and interfacial forces. Hence, the model considers a dissipation function, R, associated with the vertex motion and the interfacial free energy H. The equation of motion for each vertex is written in the following form

$$\frac{\partial R}{\partial v_i} + \frac{\partial H}{\partial p_i} = 0, \tag{1.8}$$

where v_i is the velocity of the vertex i and p_i is its position vector [55]. Furthermore, the topological processes are implemented to simulate the

foam dynamics. Thus, a T1 is trigged when the length of the edge between two vertices is shorter than a critical value. Cantat [13] extended the model by introducing the calculation of surface tension and surfactant concentration on each edge. Nevertheless, the concentration is assumed to be uniform along the edge and the surfactant exchange across the vertices is neglected.

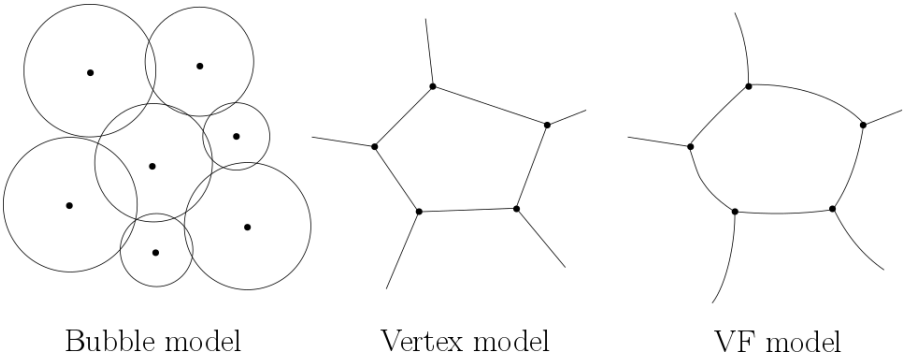

FIGURE 1.12: Sketch of few bubbles with the bubble model the Vertex model and the VF model.

Although the vertex model has been applied as a predictive tool in terms of foam rheology, the film curvature and the connected local dissipation phenomena are not taken into account. Moreover, the constraint of straight edges makes the model inapplicable to wet foams.

1.4.3 The Viscous Froth Model

The viscous froth model was developed by Kern *et al.* [45] in order to model dry foams. The model allows the study of foam coarsening and the examination of viscous drag effects in simple rheological cases.

Clusters of n bubbles are simulated through discretized films. Each bubble has a certain pressure P and films are subjected to interfacial tension γ, which is assumed to be constant everywhere in the foam. The viscous froth model is an extension of the Young-Laplace law. In addition to considering the relation between the gas pressure drop ΔP across films, for instance between adjacent bubbles, and the film curvature K, the viscous froth model introduces a term to describe the local dissipative force opposing the motion of the interface, as shown in Figure 1.13.

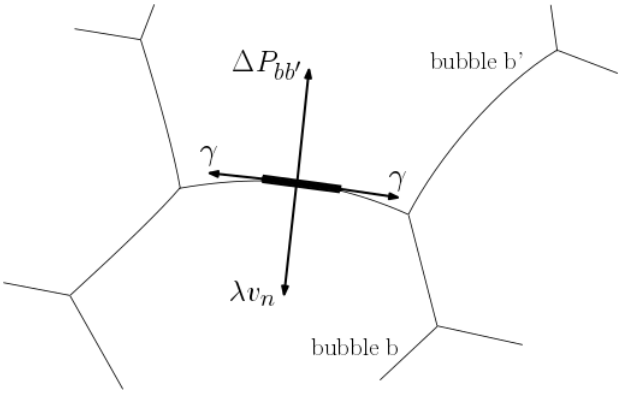

FIGURE 1.13: The forces acting on a segment of soap film, which are considered in the viscous froth model. In the case illustrated, the film moves upward [45].

The dynamic equation of a single film, in a direction normal to the film, is

$$\lambda {v_n}^{\alpha} = \Delta P - \gamma K, \tag{1.9}$$

where λ is the drag coefficient, and v_n the normal velocity. Differently from Frost *et al.* [31], who localized the drag dissipation only at each vertex, in the viscous froth model the friction effects are extended to

the whole foam, applying Eq.1.9 at each point of the discretized film. Generally, the model is simplified by setting $\alpha = 1$, although analysis of experiments for quasi-two-dimensional flowing foam established a range of values for α between 1/2 and 2/3 [14]. Furthermore, for the evolution of the structure, the vertex dynamics is calculated considering that both pressure and viscous forces vanish at the vertex and that an angle of 120° between films at each vertex is maintained.

In the present work we extend the viscous froth model considering the effect of dissipation due to the tangential displacement of surfactant molecules along the film. We present our model in Chapter 2.

1.4.4 The Bubble Model

The Bubble model was developed by Durian [26] and it represents bubbles by circular discs (or spheres in 3D). The model considers two ingredients to equilibrate the foam, a repulsive force F_n and a viscous force F_d. The first contribution F_n is a simple spring force, which acts in the direction of the line through the centres of adjacent bubbles. The discs overlapping length, Δ_{ij}, is used to calculate the modulus of the repulsive force between the pair of bubbles:

$$\bar{F}_n = k_e \frac{R_0}{R_i + R_j} \Delta_{ij} \bar{n}_{ij}, \tag{1.10}$$

where k_e is the coefficient of elasticity, R_0 is the average bubble radius of the whole foam while R_i and R_j are the radii of a pair of bubbles in contact, as shown in Figure 1.14.

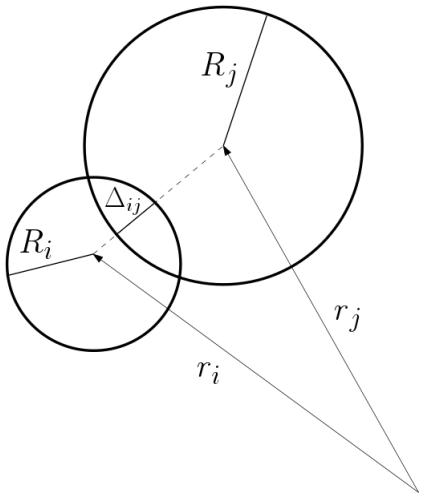

FIGURE 1.14: Two neighbouring disc-bubbles i and j are shown, Δ_{ij} is the overlapping length, which is calculated along the line through the bubble centres. R_i and R_j are the radii of a pair of bubbles in contact while r_i and r_j are the vectors to define the position of the centre for the two bubbles i and j.

The viscous force F_d involves a dissipation constant c_b and it acts in the direction of the difference of the velocity vectors $\bar{v}_i$ and $\bar{v}_j$. The force is therefore written as

$$\bar{F}_d = -c_b(\bar{v}_i - \bar{v}_j). \tag{1.11}$$

The Bubble model neglects inertia and, as a consequence, all forces are balanced on each bubble. Langois *et al.* [48] introduced a slight variation, differently from Durian, who set an average velocity for all the bubbles j surrounding the bubble i. Langois allowed each bubble to move independently, subject to the elastic and dissipative forces, obtaining results significantly different from Durian. They applied the model to investigate rheological properties of a wet foam.

Although the model is simple and computationally fast, it does not capture the foam geometry and therefore it is not suitable for the case of dry foams. On the other hand, it constitutes a tool to simulate disordered foams and to investigate the variation of foam liquid fraction.

1.4.5 The DySMaL Model

As mentioned before, the Bubble model studies wet foams by simplified forces between bubble centres. The DySMaL model introduces a new approach, modelling contacts between bubbles as simple viscous friction, an idea somehow analogous to the viscous froth model [43]. This new approach offers a detailed description of the bubble interfaces and allows the reproduction of simple experimental results with reasonable accuracy.

The DySMaL model is a particle-based model in which particles propagate in a carrier fluid. Despite the fluid is not directly simulated, its properties as density, pressure and viscosity μ are clearly taken into account within the viscous interaction between the bubbles. The dynamics of the bubbles are mainly due to surface tension and pressure, which act respectively in a direction parallel and normal to each segment. Additionally, the interactions between bubbles are modelled through viscous and elastic contact forces, $F_{V_{con}}$ and $F_{E_{con}}$, as shown in Figure 1.15. The viscous contact force depends on the relative velocity, $\bar{v}_{rel}$, between the bubbles in contact and is given by

$$F_{V_{con}} = -\mu \frac{\bar{v}_{rel}}{l_{int}} l_{con} d, \tag{1.12}$$

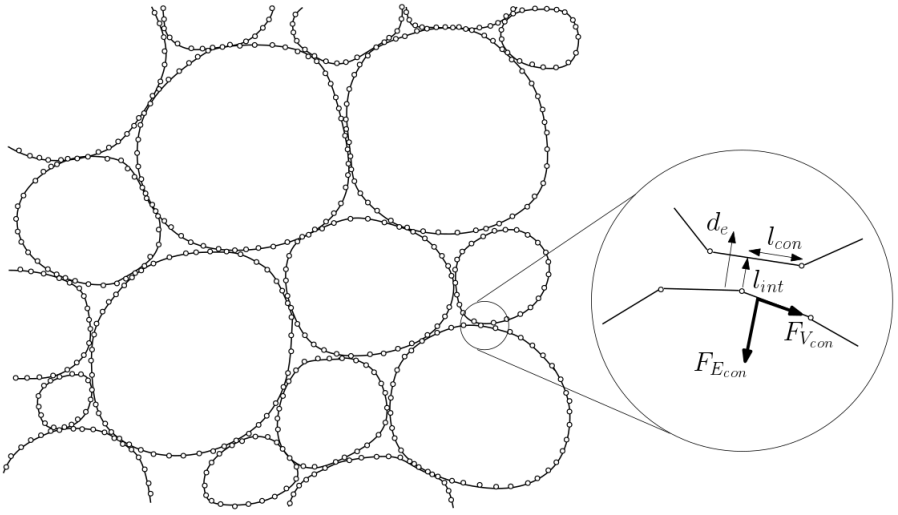

FIGURE 1.15: Deformable bubbles within a wet foam. On the right the contact viscous and elastic forces are shown, respectively $F_{V_{con}}$ and $F_{E_{con}}$. The shortest distance l_{int}, the overlapping length l_{con} and the contact range d_e are also indicated.

where l_{int} is the shortest distance between segments while $l_{con}d$ is the overlapping area, as shown in Figure 1.15. The repulsive force is instead written as an elastic force in the following form:

$$F_{E_{con}} = -k_e l_{con} d(1 - l_{int}/d_e)\bar{l}_{int}, \tag{1.13}$$

here k_e is the elastic contact modulus and d_e is the contact range. The ratio l_{int}/d_e prevents penetration of bubbles as long as $l_{int} < d_e$.

As already mentioned, the model is a powerful tool to investigate soft-matter dynamics. It leads to results which are coherent with experimental data in the case of foam subjected to linear shear, moreover, it offer the

possibility to study the interactions between foams and small solid objects [43].

1.5 Remarks

In this chapter, we presented the well-known fundamental laws for foam physics and we offered an overview of a few rheological key concepts. Moreover, we briefly described some of the existing models which have been developed to simulate and investigate both general foam physics and rheological properties. Although those models are able to capture several foam properties, none of them can completely predict all phenomena which affect foam dynamics. This thesis presents a new contribution that we add to the foam state of art.

The following chapters describe our model and some of its possible applications. We develop an extension of the viscous froth model (Chapter 2) introducing the variation of the surface tension along the films in order to consider the drag related to the surfactant molecules in the thin layer at the film interface. We use a simple experimental set up to realize a two-dimensional system of five films and we use the experimental measurements to validate our model.

We then apply the model to both disordered and ordered foams to investigate their rheological properties. We present our results in Chapter 3. Finally, we extend our model to the study of biological tissue, as we explain in Chapter 4.

Chapter 2

Film relaxation after a T1

An aqueous foam is a collection of gas bubbles in a surfactant-laden liquid. They are used widely, for example in ore separation, fire-fighting and interventional medicine [15], and therefore understanding the flow properties of this yield-stress fluid is important. The stability imparted to the thin films by the surfactant is tenuous, and as a foam flows the local concentration of surfactant may vary, leading to variations in surface tension and possible film collapse. The present chapter is dedicated to the study of the film relaxation after a T1, as a tool to investigate the stability of the films.

A dry foam is a foam characterized by low liquid fraction. The local geometry of the soap films, which is described by Plateau's laws [15], is determined by mechanical and thermochemical equilibrium conditions, and the Young-Laplace law describes the fundamental relationship between the curvature of the soap film and the pressure drop across as

we explained in Chapter 1. As a foam flows, the bubbles move past one another, leading to the film-scale topological processes of foam rearrangement.

It is quite straightforward to realize an experiment to study a single T1. Consider the evolution of five soap films between two flat plates which are connected by four pins [15], as shown in Figure 2.2. In a five films system a T1 can be thought of as an evolution from an initial non-equilibrium configuration toward a final equilibrium configuration.

The initial configuration collapses, due to the shrinking of the central film, into an unstable configuration in which four films meet at a point. Instantaneously a new film is created. The new film will stretch, while the lateral films shrink, until equilibrium is reached [15]. The films are subjected to the same air pressure on each side (so that we need not consider the effects of pressure). Nonetheless, during the relaxation of the structure the films are not straight: the lateral film, denoted l_2 in Figure 2.1, exhibits a non-zero curvature. This is due to the effects of drag with the flat plates bounding the films. Here we focus on this single T1: we investigate the evolution of the new film generated during the T1 in relation to the surface rheological properties of the film. In particular we look at the influence of the viscoelastic parameters on the film evolution toward the final equilibrium configuration.

We study the thin layer at the interface where the surfactant molecules tend to assume an ordered distribution. We focus purely on the interfacial phenomena and we neglect all the diffusion and absorption processes.

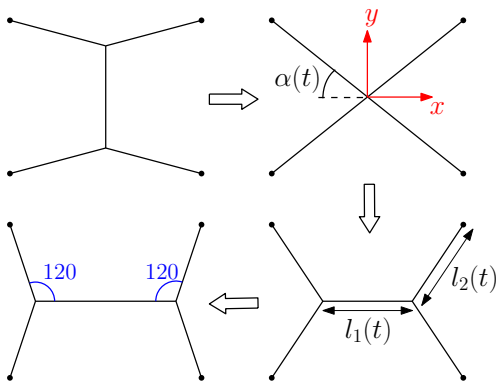

FIGURE 2.1: Topological T1 process: evolution from the starting configuration to the final one in which the surface tension forces are balanced and $\alpha = 60°$.

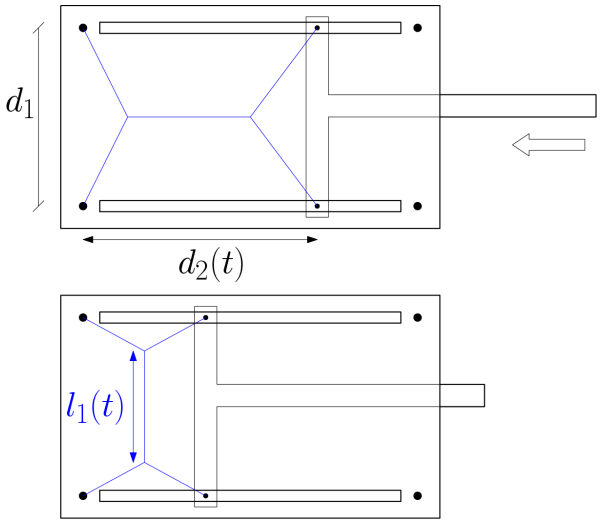

FIGURE 2.2: Device used for the experimental measurements.

We therefore consider an insoluble layer, by assuming that on each interface the rate of surface dilatation greatly exceeds the rate of surfactant transport to or from the bulk phase.

There are several quasi-static models that have been developed to simulate foam flow on the basis of energy minimization, we presented a few of them in Section 1.4.1. Here, we wish to investigate viscous phenomena, and so we instead choose a dynamical model in which the film shape and motion are determined by a force balance. The Viscous Froth (VF) model [45], which we presented in Section 1.4.3, was developed to extend quasi-static models of two-dimensional foam flow to include the viscous drag that is exerted on the soap films by the surfaces bounding the foam. It is adapted particularly to a bubble monolayer in a Hele-Shaw cell (between parallel glass plates), and shows how rate effects influence film shape [23].

However, the VF model considers surface tensions to be constant, so we add to the VF model a surfactant transfer (ST) model. As a consequence we are able to describe the variation of surface tension as a function of the concentration of surfactant molecules on each of the films of a foam. The evolution of surfactant concentration Γ and surface tension γ are related by the Langmuir equation of state:

$$\gamma = \gamma_{eq} - E \ln \frac{\Gamma}{\Gamma_{eq}}, \tag{2.1}$$

where E is the Gibbs elasticity, while γ_{eq} and Γ_{eq} are the values of the surface tension and the surfactant concentration at equilibrium. We also

introduce an additional viscous term which accounts for the motion of surfactants due to gradients in surface tension.

Our model extends the work of Durand and Stone (DS) [25], in which the dynamics of films after a T1 follows from a force balance (at the vertex) between the stretching and the shrinking films and a surfactant mass balance. As we explain in section 2.1, DS model consider straight films and assumes that on the lateral shrinking films, l_2 and l_3 in Figure 2.3, the surfactant concentration is constant and equal to surfactant concentration at the equilibrium Γ_{eq}.

Relaxing these rather strict assumptions, we will allow film curvature and variations in surface tension on all films. We will validate our new VF+ST model by fitting its predictions to experimental data for the evolution of the length of the newly created film after a T1 in systems containing different surfactants. Extending the VF model, which generates an estimate of the viscous drag coefficient, our VF+ST model predicts two additional parameters, the Gibbs elasticity and the surface viscosity, for each surfactant mixture. Although at very short times the VF model is able to fit the data for anionic surfactants, at long times the introduction of the additional viscous factors within the VF+ST model is crucial in order to fit data for both anionic surfactants and proteins.

2.1 Durand and Stone model

The DS model considers the three films l_1, l_2 and l_3, shown in Figure 2.3, and assumes them to be straight. The monotonic increase of the angle α (see Figure 2.1) between the lateral film, l_2, and the x axis, after a T1, drives the stretching of the newly-created central film, l_1.

The DS model also considers that on the shrinking interfaces the surfactant concentration (and hence surface tension) is constant, and so the equilibrium condition of equal film tensions, when films meet at $\frac{2\pi}{3}$, is only realised in the limit of $E \to 0$ (this result is compared with our own, later, in Figure 2.6).

In the force balance, the DS model combines the shear and dilatational viscosities, denoted by μ_s and k respectively, into a single surface dissipative term. The main equation of the DS model is written as follows:

$$2\gamma_{eq}\cos(\alpha(t)) - \gamma(t) - (\mu_s + k)\frac{\partial U}{\partial x} = 0. \tag{2.2}$$

The force balance on x-axis presents the double contribution of the constant surface tension, γ_{eq} from the lateral films, and the surface tension $\gamma(t)$ of the interface l_1.

The third term of the equation is the surface dissipative term, where U denotes the surface velocity which is assumed to be different from the velocity of the vertex, the x refers to the coordinate system in Figure 2.1. Eq. (2.2) indeed expresses the balance at the vertex between the surface tension contributions and a surface dissipative effects.

Durand and Stone fit experimental data for two surfactants: sodium dodecyl sulfate (SDS) and protein bovine serum albumin (BSA), in order to estimate the characteristic Gibbs elasticity and the sum of shear and dilatational viscosities for these foam films. The process of diffusion and adsorption between the bulk liquid and the film surface are neglected in the DS model and the results predicted through the model are in good agreement with values present in literature [51, 65].

As we said the DS model assumes that both the shrinking films, l_2 and l_3, have constant surfactant concentration equal to Γ_{eq}. However this assumption would only be realistic when considering a double interface for each film. In this case on the interface l'_2, due to the symmetry, there would not be an exchange of surfactants with the adjacent interface, l'_3 in Figure 2.3. Vice versa the films l_2 and l_3, considered in DS model, are in contact with the stretching film, l_1, therefore they have to present a time dependent surfactant concentration. As a consequence of the different lengths of the two adjacent films, l_1 and l_2, the mass balance should indeed lead to variation of surfactant molecules concentration on both films.

2.2 Surfactant transfer model

Here we model the variation of surfactant coverage Γ along the films. To allow film curvature, each film is discretized into a number of short straight segments. We define these segments to meet at *nodes* within

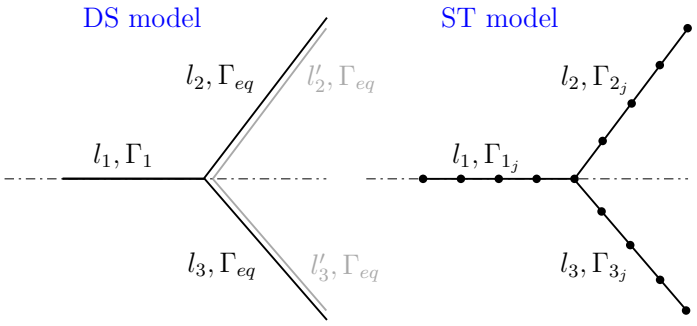

FIGURE 2.3: On the left, the film configuration considered in DS model, l_1 l_2 and l_3. The shrinking films, l_2 and l_3, have constant surfactant concentration, Γ_{eq}. The dot-dashed line represents the axis of symmetry. On the right, the configuration considered with the ST model. Each film l_i is discretized into several short straight segments l_{i_j}, each with a variable surfactant concentration Γ_{i_j}.

the film, and three segments meet at a *vertex*. We introduce subroutines to keep the average length of segments uniform, by subdividing and removing segments when they become too large or short respectively, ensuring that the number of surfactant molecules per film is conserved. In particular we check at each time that the segment length l_j is always $l_{min} \leq l_j \leq l_{max}$ where l_{min} is the length at which a T1 may occur (if the short segment directly connects two vertices). In this way we allow compression and stretching of films and, by choosing an appropriate time-step, ensure the stability of the numerical calculation.

We calculate the variation of surface tension γ by applying equation of state, Eq. (2.1), to each segment. We define a "convection equation", similar to the Marangoni effect [27], to describe the movement of surfactant molecules along each film as a consequence of gradients of surface tension. This takes the form of a rule for tangential motion of the nodes,

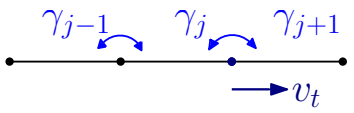

FIGURE 2.4: A film is discretized into several segments. Each segment has an initial number of molecules and surfactant concentration. Through Eqs.(2.1) and (2.3) we calculate the surface tension γ_j of each segment and the tangential velocity component v_t of each node.

which connect pairs of film segments, along the film, based on the difference in tension between the two segments. As a consequence, the segments contract when they have high surface tension, leading to an effective flow of surfactant within the film. This flow is subject to a viscous drag, and so our model balances the gradient of surface tension along each film with the tangential component of the surface velocity, v_t, multiplied by a factor μ, which we think of as a surfactant drag coefficient:

$$\mu v_t(s) - \frac{\partial \gamma}{\partial s} = 0, \tag{2.3}$$

where s is the curvilinear coordinate along the film. Similarly to the drag coefficient λ in the VF model our μ has the dimension of a force times $time/length^2$, we are indeed considering the tension as a line tension whose dimension is a force. The gradient of surface tension is known at each point, so we are able to apply this equation there, rather than considering only the balance at the vertex, as is done in the DS model.

The surfactant balance is imposed numerically: we assume a starting value for the surfactant concentration, we calculate the number of surfactant molecules N_{mol} per segment, through the expression $\Gamma_j = \frac{N_{mol}}{l_j}$,

and then we update the surfactant concentration of each segment, according to its deformation. We are therefore able to calculate the surface tension for each segment by means of Eq. (2.1), and then applying Eq. (2.3) gives the tangential velocity component for each point, see Figure 2.4.

2.2.0.1 Is diffusion of surfactant important?

Within a real foam film, surfactant molecules move in several ways. As we note above, we assume that surfactant transfer between the surface layer and the bulk is slow compared to the motion within the surface layer. Within the surface layer itself, surfactant molecules respond to gradients in concentration: this can take the form of a convective motion, limited by viscosity, as in Eq. (2.3), or a diffusive flow.

In order to highlight the qualitative behaviour of Eq. (2.3), we compare it with the result of solving a diffusion equation. We consider a single straight film of unit length with an initial Gaussian distribution for the concentration of surfactant molecules, centred on the middle of the film, and we compare the standard analytical solution for the diffusion equation with a numerical solution of Eq. (2.3).

Figure 2.5a shows the variation of surfactant concentration on each segment with time as it evolves towards the final, uniform distribution, calculated through Eq. (2.3). Figure 2.5b shows how the two phenomena, plotted in *dimensionless* form, are identical. Thus Eq. (2.3) is effectively acting as a diffusive process.

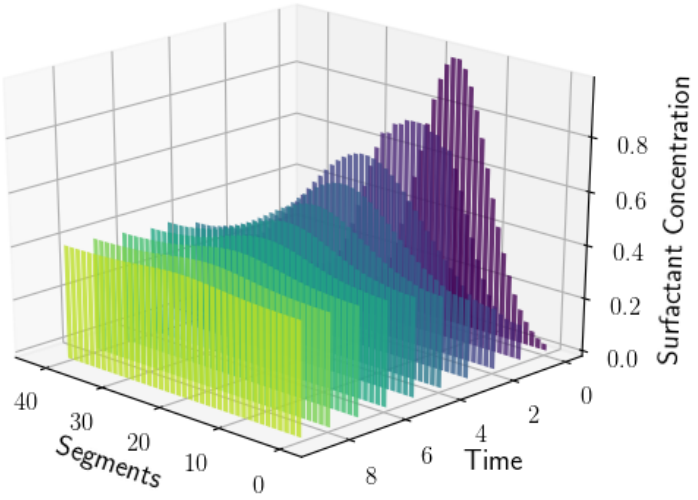

(a)

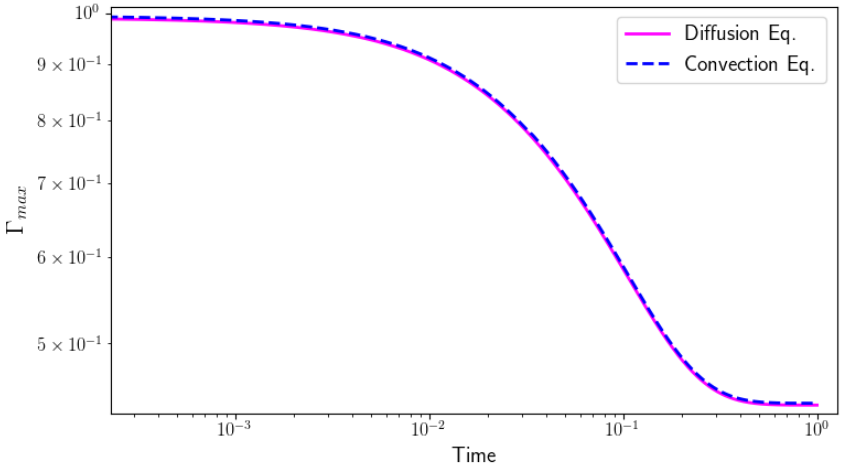

(b)

FIGURE 2.5: a) Variation of the concentration of surfactant molecules on a single straight film, starting from a Gaussian distribution, from the solution of Eq. (2.3) with $\mu = 1$. We show the variation of surfactant concentration on each segment with time as it evolves towards the final, uniform, distribution. b) Comparison of the maximum value of Γ between the numerical solution of Eq. (2.3) and the analytic solution of the diffusion equation with unit diffusion coefficient.

However, in *dimensional* form, the typical order of magnitude for the diffusion coefficient for surfactant motion is $10^{-10}[m^2\ sec^{-1}]$[54] while the surface viscosity μ is generally $10^{-3}[kg\ m^{-1}\ sec^{-1}]$[25].

This implies that in practice diffusion is much slower than convection, and so we therefore focus here on convective effects.

2.2.0.2 Vertex dynamics

The dynamics of a vertex is calculated through a force balance based on the orientation and tension of each of the three films that meet there. Given the length and surface tension of each of the three segments joining at the vertex, we calculate the vector $\underline{\gamma}_i = \frac{l_i}{|l_i|}\gamma_i$, where $i = 1, 2, 3$. The resultant surface tension force on the vertex is then obtained as the vector sum of the three components, $\underline{\gamma}_i$.

As in the VF model, described below, this net force is balanced by the friction experienced by the vertex and the neighbouring films due to the bounding flat plates which confine the films in our two dimensional system. The friction term is proportional to the vertex velocity, $\lambda\overline{v}_V$, with drag coefficient λ. Then

$$\lambda\underline{v}_V + \frac{\sum\underline{\gamma}_i}{\sum l_i} = 0. \tag{2.4}$$

The resultant surface tension is normalized with the sum of the lengths l_i of the three segment merging at the vertex. The normalization allows us

to take into account the change in length of segments in the discretization of the films.

While the viscous force in Eq. (2.3) represents the surfactant drag effects opposing the motion of surfactants, this viscous drag force takes into account the contact between films and bounding surfaces. Essentially Eq. (2.4) is an adaptation of the VF model, which we presented in Section 1.4.3, to the particular case of the threefold junction (see Appendix A.2).

2.2.0.3 Surfactant transfer at the vertex

Satomi *et al.* [66] highlight the non-negligible effect of surfactant transfer across the vertex. In section 2.5.2 we show (Figure 2.7a) that without transfer of surfactant between films the system will reach its final equilibrium configuration far from Plateau's conditions. Therefore, in contrast to the DS model, we assume a continuous exchange of surfactant across vertices.

We use the model introduced by Satomi *et al.* [67] to relate the amount of surfactant transferred across the vertex to the gradient of surface tension of adjacent films through a coefficient referred as a "Marangoni" coefficient, D_m. The quantity of molecules which moves across the vertex at each step, $\Gamma_i l_i$, is proportional to the difference in the surface tension on each neighbouring segment. With the notation of Figure 2.3, we have

$$\frac{d(\Gamma_i l_i)}{dt} = D_m(\gamma_i - \gamma_k), \tag{2.5}$$

where $i = 1, 2, 3$ are the indices for films at the vertex and $k = (i - 2)(mod\ 3) + 1$. Satomi *et al.* define D_m to be a function of the vertex size (i.e. liquid fraction), the surface and bulk viscosity and a characteristic system size. They consider a range of values for D_m between 1 and 5. Here, we deduce D_m from dimensional analysis of Eq. (2.5): we define D_m to be the ratio between the concentration of surfactant at equilibrium and the surfactant drag coefficient μ. Introducing the length-scale d_1, which is the distance between the pins to which the soap films are attached (see Figure 2.2), we have:

$$D_m = \frac{\Gamma_{eq}}{\mu d_1}.$$

By relating D_m to μ we reduce the total number of free parameters in our model.

2.3 Viscous Froth model + Surfactant transport

We now explain how we relax the other strong assumption of the DS model, that of *straight* films.

As explained by Satomi *et al.* [66], the two-dimensional Viscous Froth model (VF model) of Kern *et al.* [45] is a powerful tool to simulate the rheology of dry foam, in particular to describe the variation of curvature K along the film. In the present work we consider that all films are subjected to the same pressure on both sides so we neglect the pressure

term of Eq.(1.9). Hence we consider the following equation:

$$\lambda v_n = -\gamma(\Gamma)K. \tag{2.6}$$

As explained by Drenckhan *et al.* [23], quasi-static models fail to reproduce effects observed in some high velocity experiments of dry foam flowing in channels, while the VF model presents good agreement with experiments. Despite the good agreement, the VF model considers only normal forces acting on the films, while, as confirmed by Cantat *et al.* [14], in the case of higher velocities the presence of both normal and tangential viscous contributions must be included in any useful model. We therefore use the VF model to calculate the diffusion of curvature along the films, and instead of considering a constant surface tension, we introduce our calculation of surfactant transport.

2.4 Dimensionless variables

A simple dimensional analysis allows us to write a non-dimensional set of equations. We choose d_1 to be the reference length, which we take to be the distance between the pins, $d_1 = 4$cm (see Figure 2.2). Then our dimensionless variables are:

$$\tilde{l} = \frac{l}{d_1}, \; \tilde{K} = K d_1, \tag{2.7}$$

$$\tilde{\gamma} = \frac{\gamma}{\gamma_{eq}}, \; \tilde{\Gamma} = \frac{\Gamma}{\Gamma_{eq}}, \tag{2.8}$$

where K is the curvature while γ_{eq} and Γ_{eq} are the surface tension and the concentration of surfactant molecules at the equilibrium. We also define time scales for the three kinematic equations. As illustrated by Kern *et al.* [45], the time-scale related to the film relaxation for the VF model, T_λ, can be defined as

$$T_\lambda = \frac{\lambda {d_1}^2}{\gamma_{eq}}. \tag{2.9}$$

Dimensional analysis of the vertex dynamics, Eq. (2.4), leads to a time-scale $T_V = T_\lambda$, while for our surfactant drag equation, Eq. (2.3), we find

$$T_\mu = \frac{\mu {d_1}^2}{\gamma_{eq}}. \tag{2.10}$$

The three kinematic equations in dimensionless form are:

$$\tilde{v}_n = -\tilde{\gamma}\tilde{K} \quad (VF), \tag{2.11}$$

$$\tilde{v}_t = \frac{1}{\hat{\mu}}\frac{\partial \tilde{\gamma}}{\partial \tilde{s}} \quad (ST), \tag{2.12}$$

$$\underline{\tilde{v}}_V + \frac{\sum \underline{\tilde{\gamma}}_i}{\sum \tilde{l}_i} = 0. \tag{2.13}$$

In order to obtain the same time-scale for the three equations, we set $T_\mu = \hat{\mu} T_\lambda$, introducing the free parameter $\hat{\mu} = \frac{\mu}{\lambda}$ in Eq. (2.12). We assume that surfactant drag is weaker than friction with the boundary, choosing a range of values for $\hat{\mu}$ between 0.1 and 1, in section 2.5.2 to investigate the influence of viscous effects on the model's predictions.

In dimensionless form, the equation of state, Eq. (2.1), becomes

$$\tilde{\gamma} = 1 - \hat{E} \ln \tilde{\Gamma}, \tag{2.14}$$

leading to our second free parameter $\hat{E} = \frac{E}{\gamma_{eq}}$, which is related to the elastic properties of the films, represented by the Gibbs elasticity E. We estimate the order of magnitude of $\hat{E}$ to be one in the case of SDS [25]. The initial condition is that the initial surfactant concentration is Γ_{eq}, and hence the dimensionless surfactant concentration on each segment is $\tilde{\Gamma} = 1$. This means that all segments initially have surface tension $\tilde{\gamma} = 1$.

Eq. (2.5) for the surfactant transfer across the vertex becomes, in dimensionless form,

$$\frac{d(\tilde{\Gamma}_i \tilde{l}_i)}{d\tilde{t}} = \hat{D}_m(\tilde{\gamma}_i - \tilde{\gamma}_k), \tag{2.15}$$

where $\hat{D}_m = 1/\hat{\mu}$

To determine the relaxation dynamics of a system of soap films, we must solve Eqns. (2.11) – (2.15).

2.5 Results

In this section we describe the qualitative behaviour of the VF+ST model. In particular we compare its prediction of the variation of the film length, $l_1(t)$, after a T1 topological process with the predictions of

the simpler models described above. We will then determine the concentration of surfactant molecules and the consequent evolution of the surface tension in time, varying the free parameters $\hat{E}$ and $\hat{\mu}$.

2.5.1 Reference case

We first summarise, in Figure 2.6, the different models in terms of their prediction of the evolution of the film length in time. (i) For the DS model we take $\hat{E} = 0$ or 1 and the factor $\frac{\mu}{\gamma_{eq}} = 1$. (ii) To simulate the pure VF model, we apply Eq. (2.11) and Eq. (2.13) with all surface tensions equal to one. (iii) For the ST model we solve the system (2.12) – (2.15) with $\hat{E} = 1$ and $\hat{\mu} = 1$. (iv) For the VF+ST model we fix $\hat{E} = 1$ and $\hat{\mu} = 1$ and solve the system (2.11) – (2.15). When $\hat{E} = 0$ the VF+ST model is effectively reduced to the VF model.

Grassia *et al.* [33] showed that the DS model predicts a slow evolution at short times; this is because it allows slippage between the vertex velocity and the extension rate of surface fluid elements on the film, leading to the trend shown in Figure 2.6. Moreover, the film reaches its final equilibrium configuration, where the films meet at $\frac{2\pi}{3}$, only in the limit of $E \to 0$. This is due to the assumption of constant surfactant concentration on both the shrinking films, l_2 and l_3 (see Figure 2.3).

In contrast to the DS model, the VF model predicts a rapid rise of the film length towards the final length. Because the force balance at the vertex only depends on the lengths of the segments which join at the vertex, the condition of final equilibrium is quickly realised.

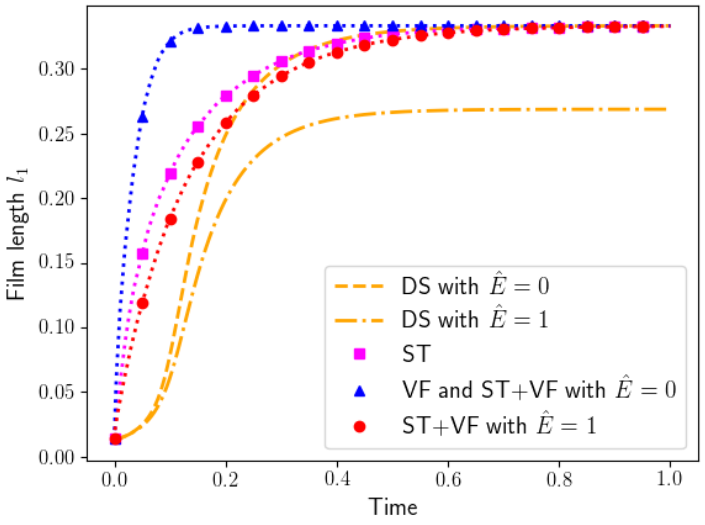

FIGURE 2.6: Variation of the film length l_1 with time, after a T1. We compare the length evolution for the described models, DS, ST, VF and ST+VF. For the DS model we report results for both $\hat{E} = 0$ and $\hat{E} = 1$. For the ST and ST+VF models both $\hat{E}$ and $\hat{\mu}$ are one.

Including the ST model takes into account the variation of the surface tension on each segment and the associated additional viscous effects. For this reason the balance at the vertex is reached more slowly, and consequently the film length evolves more slowly.

Not surprisingly the combination of these last two models, VF+ST, leads to an even slower length evolution.

2.5.2 The effects of surface viscosity with and without surfactant transfer across the vertex

In order to evaluate the effect of surface viscous components of our model we fix the elastic parameter $\hat{E} = 1$ and we vary $\hat{\mu}$ between 0.1 and 1.

2.5.2.1 Without surfactant transfer across the vertex

As a first step we consider how the system of soap films relax without surfactant transfer between films (across the vertex), i.e. when $\hat{D}_m$ is decoupled from $\hat{\mu}$ and then set to zero.

Figure 2.7a shows how, following a T1, the newly-created film l_1 starts to grow while the lateral film l_2 shrinks. Consequently, the surfactant concentration on the stretching film l_1 decreases while the concentration on the shrinking film l_2 increases. This is shown in Figure 2.7b where we plot the average surfactant concentration on both films. Figure 2.7b also shows, for each film, the value of Γ on the segments which meet at the vertex. The concentration Γ_{2_0} increases, due to the reduction of the film length, and then decreases as a consequence of the homogenisation of segment lengths within the same film.

As expected from Eq. (2.14), the opposite trend is found for the surface tension: γ increases on the stretching film l_1 and decreases on the shrinking film l_2, as shown in Figure 2.7c.

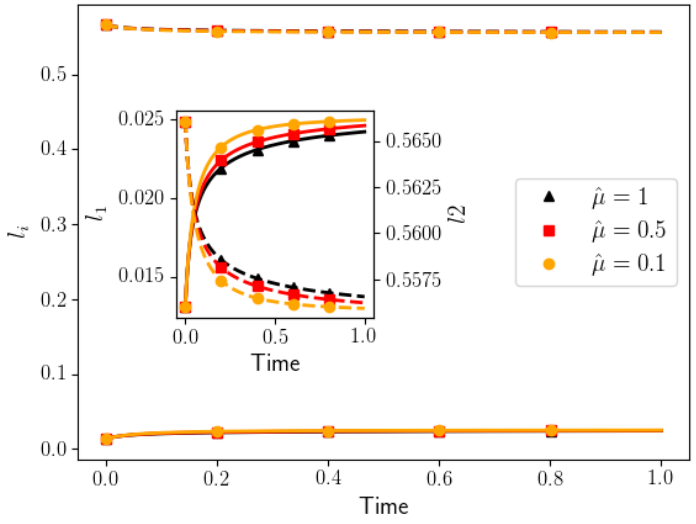

(a)

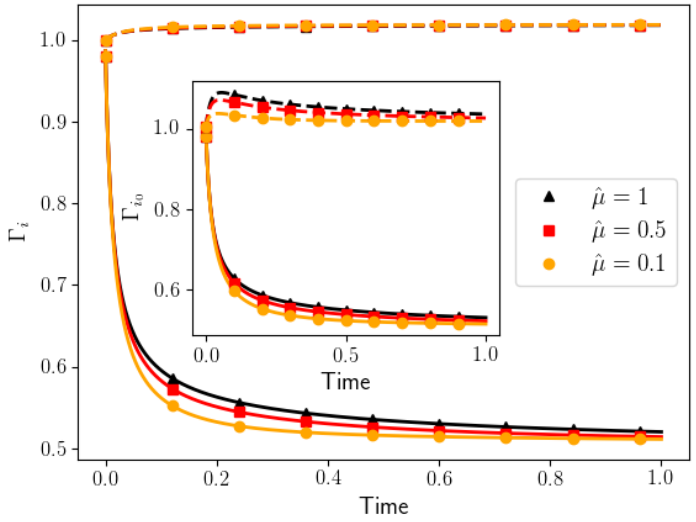

(b)

FIGURE 2.7: ST+VF model results for different $\hat{\mu}$, with $\hat{E} = 1$ and $D_m = 0$, for the stretching film l_1 (solid lines) and the shrinking film l_2 (dashed lines). a) Variation of film lengths. b) Variation of average surfactant concentration Γ_i. c) Variation of average surface tension γ_i. In b) and c) the insets show the same data for the segments which meet at the vertex, Γ_{i_0} and γ_{i_0}. The Figure continues on the next page.

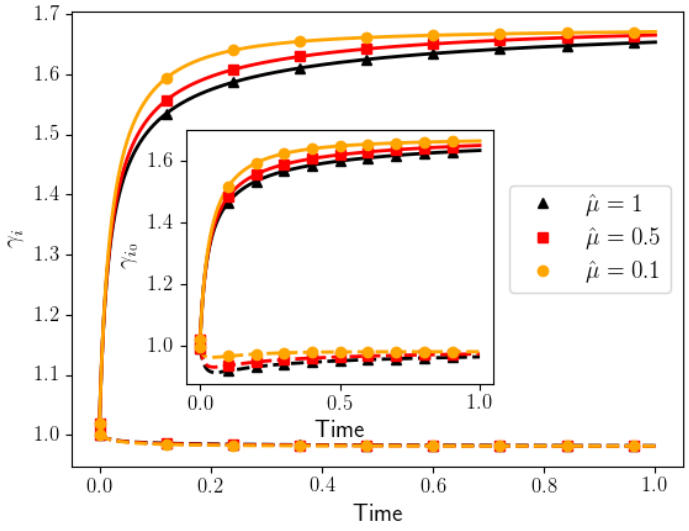

(c)

Moreover, Figure 2.7 shows how the viscous parameter $\hat{\mu}$ affects the film evolution. In particular, increasing the value of $\hat{\mu}$ slows down the relaxation, reducing the variation in film lengths, because the surfactant concentration is higher, and the tension consequently lower, close to the vertex.

Due to the condition $\hat{D}_m = 0$, suppressing surfactant transfer across the vertex, the relaxation of the film stops when the angles between the films are still far from $2\pi/3$, Figure 2.7a shows the remarkable lack of stretch of both films. This is caused by our assumption for the starting surfactant concentration value. We assume all films have a starting equilibrium concentration, Γ_{eq}. As a consequence the forces acting on the vertex are suddenly balanced, but the well-known Plateau's laws are not satisfied.

Because the T1 is an instantaneous process, it is not straightforward to estimate a coherent value for the surfactant concentration of the new created short film. We decide to assume Γ_{eq} as the starting value rather than fix an arbitrary value bigger than Γ_{eq} for the new film. In the next section we show how our assumption is physically meaningful if we allow mass transfer between adjacent films. The condition $\hat{D}_m \neq 0$ is therefore necessary in order to use our surfactant transfer model as a predictive tool.

2.5.2.2 With surfactant transfer across the vertex

To allow full relaxation to an equilibrium that obeys Plateau's rules we now relax the above condition, and introduce surfactant transfer across the vertex. Figure 2.8 shows the results when $\hat{D}_m = 1/\hat{\mu}$. Increasing $\hat{\mu}$ again decreases the rate of the length variation, shown in Figure 2.8a, because the lower surface tensions at the vertex takes more time to be balanced.

In Figure 2.8b we observe the influence of surfactant transfer across the vertex on surfactant concentration. As before, the initial trend is that the surfactant concentration on the newly-created film l_1 decreases as a consequence of it stretching. But this trend is soon reversed because of surfactant transfer across the vertex from the shrinking film, on which surfactant is building up. The relaxation then continues uniformly until the final equilibrium surfactant distribution is reached.

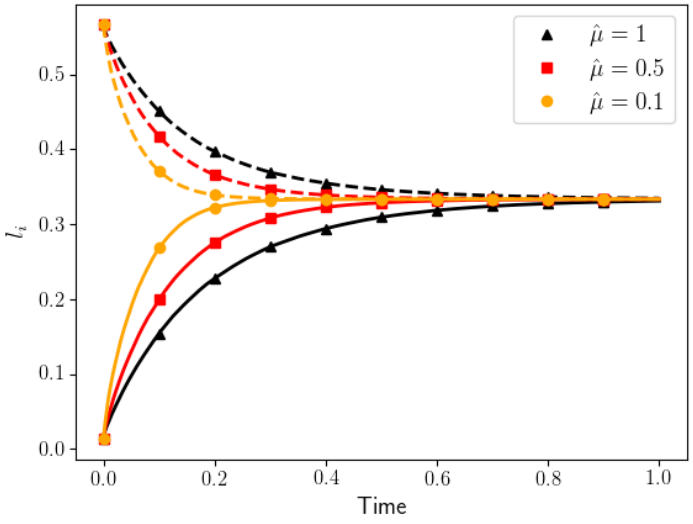

(a)

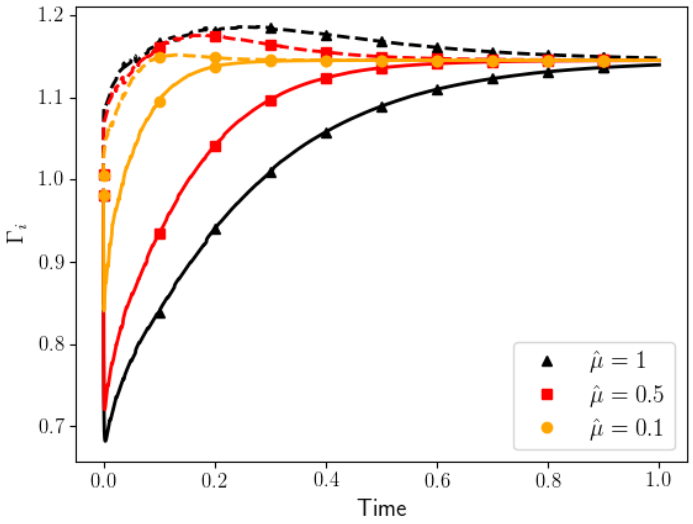

(b)

FIGURE 2.8: ST+VF model results with surfactant transfer across the vertex, with coefficient $\hat{D}_m = 1/\hat{\mu}$. Notation and other simulation details as for Figure 2.7.

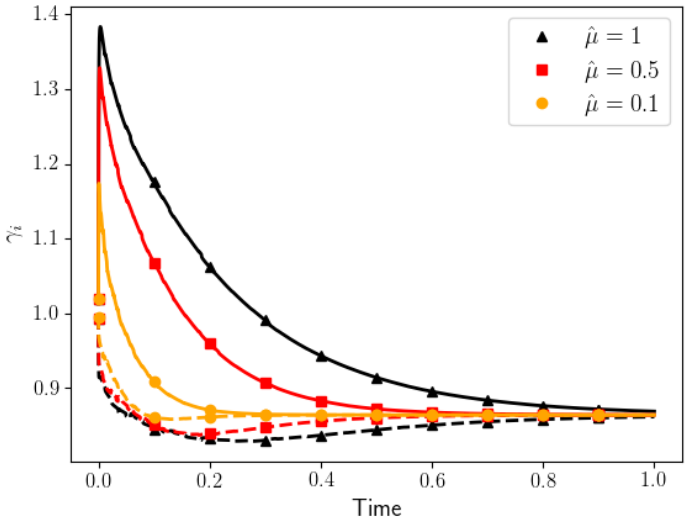

(c)

Moreover, since $\hat{D}_m$ influences the rate at which surfactant molecules move across the vertex, through Eq. (2.15), we observe how the surfactant transfer and therefore the variations in surfactant concentration occurs more quickly with small values of $\hat{\mu}$. On the other hand, on the shrinking film l_2 the surfactant transfer reduces variations in Γ. The consequent variations in surface tension γ (Figure 2.8c) are also smaller, so that the final equilibrium is reached more quickly at low $\hat{\mu}$.

As expected from the observation that soap films minimize their length [15], the total length at the final time is less than the total initial length. The number of surfactant molecules is conserved and the final value of the surfactant concentration is therefore higher than the initial (unit) value, as shown in Figure 2.8b.

2.5.3 The effect of surface elasticity

We now turn to the effect of the surface elasticity parameter, $\hat{E}$, on the evolution of the soap films. We fix the surface viscosity at $\hat{\mu} = 1$ and hence the coefficient $\hat{D}_m$ is constant. We vary $\hat{E}$ between 0.1 and 2, which affects the surface tension through the Langmuir equation of state, Eq. (2.14). With larger values of $\hat{E}$, the surface tensions acting at the vertex are weaker, and therefore the films take longer to reach their final length, as shown in Figure 2.9a.

In Figures 2.9b and 2.9c we report the average values of surfactant concentration and surface tension for the two films. The initial concentration on each film is one, but now the initial surface tension depends on $\hat{E}$ according to the Langmuir equation of state, Eq. (2.14). Similarly, the final value of surface tension, while equal on the two films, also depends on $\hat{E}$. Figures 2.9c and 2.10 show that the surface tension γ_i at equilibrium is inversely proportional to $\hat{E}$ as we expect from Eq. (2.14).

To summarise our results we calculate the time for the stretching film to reach 80% of its final length during the relaxation process. Figure 2.11 shows that increasing either the viscous effects ($\hat{\mu}$) or the surface elasticity ($\hat{E}$) results in an increase in the time required for the film to relax to equilibrium. For each value of $\hat{E}$, this relaxation time increases linearly with $\hat{\mu}$.

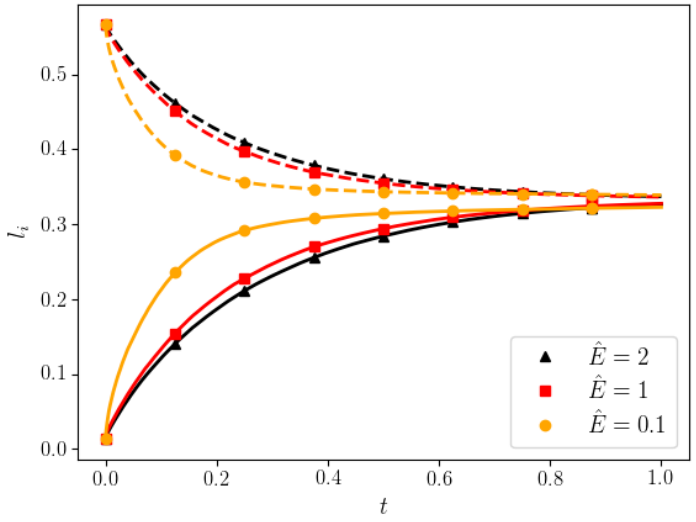

(a)

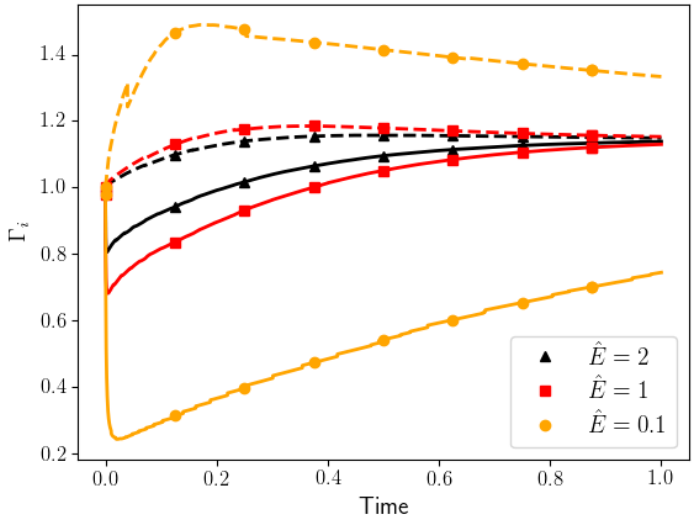

(b)

FIGURE 2.9: ST+VF model results with varying elasticity $\hat{E}$. Here $\hat{\mu} = \hat{D}_m = 1$. Notation and other simulation details as for Figure 2.7.

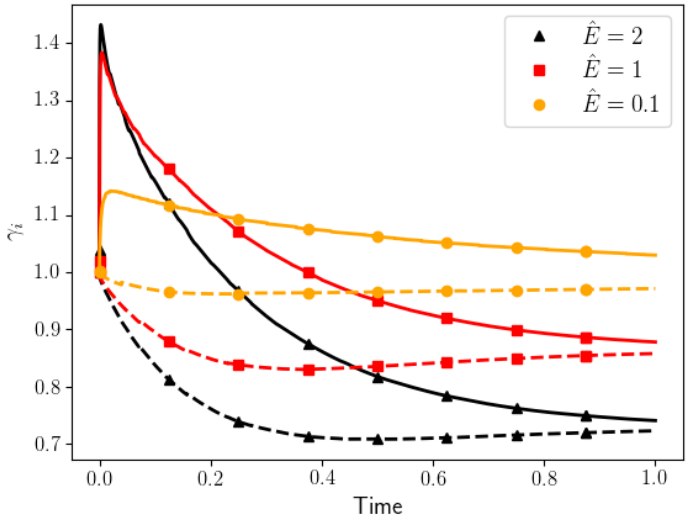

(c)

2.5.4 Experimental data fitting

2.5.4.1 Experimental details

The experimental setup is depicted in Figure 2.2. The device consists of two flat Plexiglass plates held a distance of 2cm apart by four metal pins. Two pins are fixed towards one end of the plates, a distance $d_1 = 4$cm apart. The other two pins are attached to a sliding rod which allows the distance d_2 from the fixed pins to be varied, as shown in Figure 2.2, up to about 10 cm. During the experiment, performed by Alexia Audebert from the INRA (Institut national de la recherche agronomique), the device is immersed in a solution of water and surfactant in order to create five films of the foaming solution that connect the pins. Moving the rod

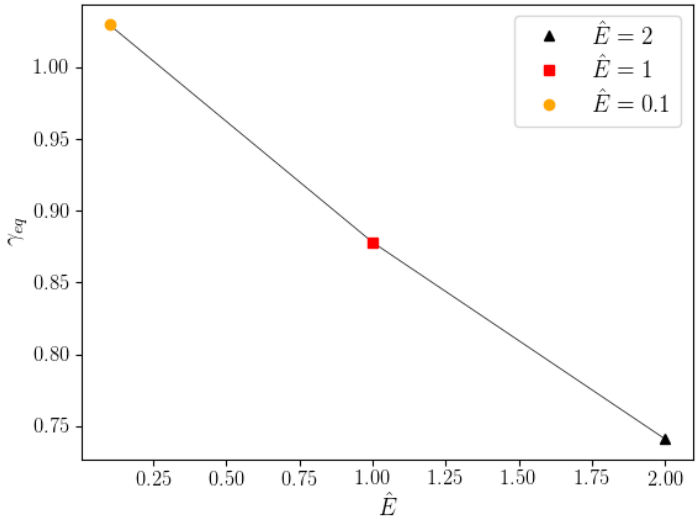

FIGURE 2.10: Values of the surface tension at the equilibrium versus the elastic parameter $\hat{E}$.

causes rearrangements of the films, and when pushed sufficiently far the rod induces a T1 process. To ensure the stability of the films, the rod was pushed (manually) slowly and as close to possible to a constant rate.

Image analysis of a video of the experiment was used to extract how the length of the film l_1 evolved after the T1. The film length is then normalized by its final length and plotted against time in seconds in Figure 2.12. In order to study the influence of the rheological interfacial properties on the T1 process we use two different foaming agents: Sodium dodecyl sulfate (SDS), at a concentration of $4.80g/l$, and β-Lactoglobulin (BLG), at a concentration of $50g/l$ and $pH = 7$. For the equilibrium

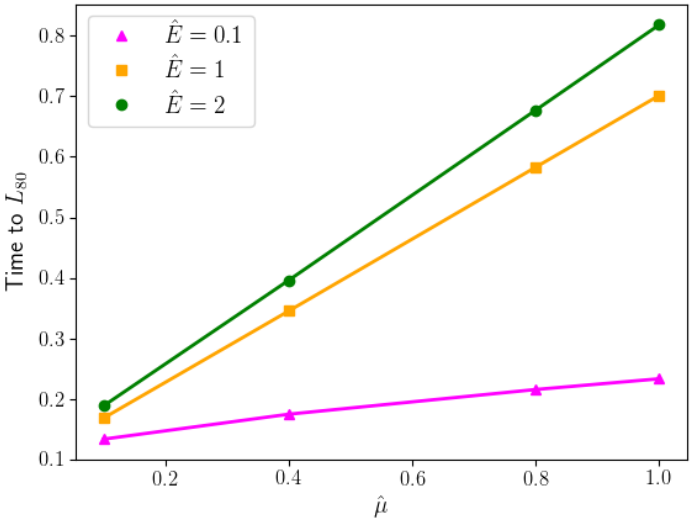

FIGURE 2.11: Variation of the time to reach 80% of the final length for the newly-created film l_1, as a function of $\hat{E}$ and $\hat{\mu}$.

surface tensions we take the values $38mN/m$ (SDS) [25] and $48mN/m$ (BLG) [2].

2.5.4.2 Validation of the VF+ST model

We validate the VF+ST model by fitting the experimental data for film length evolution after a T1 for each of these foaming solutions. The numerical model is used to simulate the film evolution, then a fitting procedure is used to extract a prediction of the material parameters.

As shown in Figure 2.12, the films made with SDS reach their final length much faster than with BLG. We first scale our numerical simulation results by choosing the time-scale T_λ to be the time at which the film length is 85% (BLG) or 99% (SDS) of its final equilibrium value. The different percentages are chosen to account for the different rates of relaxation, ensuring that for the faster evolution there are enough data points available for a good fit. As mentioned in section 2.4 we assume that the surfactant drag is weaker than the friction with the boundary, as a consequence we firstly rescale the data with the T_λ, specified above, determining the initial slope of the curves in Fig. 2.12. Successively, we use a Python optimization tool to find the optimal values for $\hat{\mu}$ and $\hat{E}$, which affect the bend point of the curves in Fig. 2.12.

Once we know T_λ we calculate $\lambda[kg\ m^{-1}sec^{-1}]$ through the definition $T_\lambda = \frac{\lambda {d_1}^2}{\gamma_{eq}}$ (Eq. (2.9)), taking the distance between the pins, as the reference length, $d_1 = 4$cm, and using the known equilibrium surface tension for SDS and BLG. Note that, as in the simple VF model [45], we consider the tension to be a force, we therefore multiply the surface tensions for SDS and BLG times the reference length d_1. The values obtained for the two samples are reported in Table 2.1.

We then convert the simulation data to real times and implement a nonlinear least-squares fit of our model to the experimental data with parameters $\hat{\mu}$ and $\hat{E}$. We impose a relative tolerance of 10^{-3} for the calculation. In Figure 2.12 we show the fit of the simulation for the normalized film length against time. In the case of BLG the fit doesn't exactly capture the early time evolution while at long times it reaches the final value

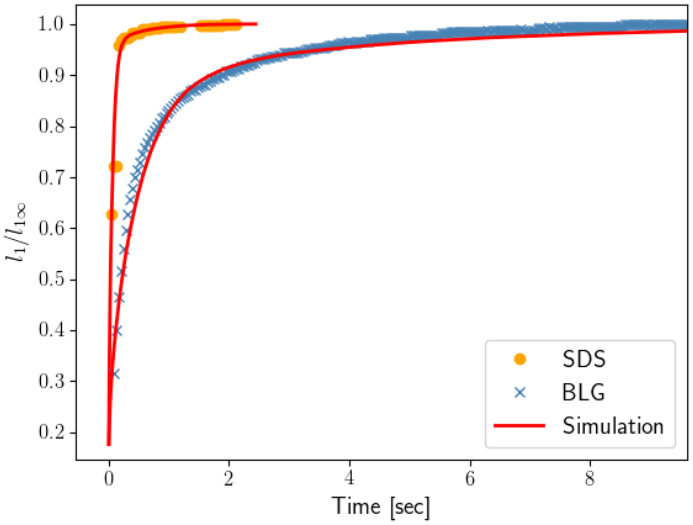

FIGURE 2.12: Experimental data for the length of the newly-created film l_1 after a T1 with surfactant solutions of SDS and BLG is compared with a simulation with the VF+ST model which has been optimized by fitting values for the parameters $\hat{\mu}$ and $\hat{E}$.

slightly slower than the experimental data, causing an overestimation of the surface viscosity.

Finally, given the optimized model parameters $\hat{\mu}$ and $\hat{E}$, we deduce $\mu = \lambda\hat{\mu}[mPa\ sec]$ and $E = \gamma_{eq}\hat{E}[mN/m]$. As we discuss in section 2.5.4.4 we compare our result with the predictions by Durand and Stone [25], we therefore multiply our μ times the reference length d_1 in order to have coherent dimensions $\mu = [mPa\ m\ sec]$. The values predicted for both the SDS and BLG solutions are reported in Table2.1; we discuss each prediction in the following sections.

TABLE 2.1: Drag coefficient (λ) surface viscosity (μ) and Gibbs elasticity (E) predicted by a fit of the VF+ST model to experimental data for solutions of SDS and BLG.

	λ $[Pa\ sec]$	μ $[mPa\ m\ sec]$	E $[mN/m]$
SDS	0.74 ± 0.02	9.96 ± 0.02	42.8 ± 0.02
BLG	3.80 ± 0.02	212 ± 0.02	156 ± 0.02

2.5.4.3 Predicting the drag coefficient λ

The values obtained for the drag coefficient λ are reported in Table 2.1: we find that λ is about six times greater for BLG compared to SDS, suggesting that λ is not a property just of the plates, but also of the solution.

Drenckhan *et al.* [23] used the VF model to simulate two-dimensional flowing foams and they predict a value for the drag coefficient λ which is slightly higher than our prediction. Their experimental setting was different, so we don't necessarily expect to find exactly the same value for λ. However, we repeated our fitting procedure for our experimental data using the VF model without surfactant transfer and, in agreement with Drenckhan's results, we find that the VF model on its own predicts a higher value for the drag coefficient: $\lambda_{SDS} = 1 Pa\ sec$ and $\lambda_{BLG} = 11 Pa\ sec$. In general, we suggest that applying the VF model on its own overestimates the drag coefficient.

Moreover, using the VF model without surfactant transfer, we notice that although at very short times the VF model is able to fit the data for anionic surfactants, at long times the introduction of additional surface

viscous factors within the VF+ST model is crucial in order to fit data for both anionic surfactants and proteins.

2.5.4.4 Predicting the surface viscosity μ

There are two contribution to the surface viscosity, which are included in μ in our model, namely shear and dilatation contributions. Edwards *et al.* [27] explain why the experimental measurement of the interfacial dilatational viscosity, k, is more challenging than the measurement of the interfacial shear viscosity, μ_s [27]. This is due to the coupling that arises between interfacial dilatational viscous and elastic effects. They also show how both components of the complex dilatational modulus, E' and E'' can be calculated as a function of the Gibbs elasticity E, a diffusion parameter τ and the frequency of oscillation during measurements ω.

In the case of an insoluble layer, when $\tau \to 0$, E' is reduced to the Gibbs elasticity while the ratio E''/ω goes to zero [27], and then the sum of the surface viscosities $\mu_s + k$, which corresponds to our μ, may be determined experimentally. Despite these considerations, it is not straightforward to find surface viscosity values in the literature. Therefore for the SDS anionic surfactant we compare our prediction for μ, in Table 2.1, with the DS model prediction [25]. They calculate $\mu_{SDS} \simeq 1.3[mPa\ m\ sec]$ while we found $\mu_{SDS} \simeq 10[mPa\ m\ sec]$. Given the large possible range of variation in the values, we conclude that the VF+ST model is consistent with earlier work in predicting the value of surface viscosity for SDS.

There is even less published data for BLG, due to the difficulties mentioned above, and it is not simple to find surface viscosity values in literature. This underlines the importance of having a tool such as the VF+ST model to predict such quantities. Nevertheless, we observe that our model probably overestimates the surface viscosity values, reported in Table 2.1, especially in the case of proteins. This suggest the possibility that there are still missing ingredients which have to be considered in order to model foaming solutions with proteins.

2.5.4.5 Predicting the Gibbs elasticity E

Finally we discuss our prediction for the Gibbs elasticity. We find a good agreement with the results of Durand and Stone for SDS. Their model predicts $E = 32mN/m$ [25], while we find $E = 42.8mN/m$.

Recall that, for an insoluble layer, the real component of the dilatational surface modulus, E', is equal to the Gibbs elasticity. In order to evaluate the accuracy of our prediction in the case of BLG, we seek characteristic values for its dilatational surface modulus.

The surface dilatational modulus of protein solutions is strongly dependent on the concentration and pH of the sample [56]. The BLG sample used in our experiments has a concentration of $50g/l$ and $pH = 7$, for which the real component of the dilatational surface modulus is $E' \approx 40$ [2], but values of up to 110 have been found [70]. Comparing these values with our prediction, reported in Table 2.1, we conclude that our prediction of the Gibbs elasticity has a reasonable order of magnitude.

2.6 Remarks

Two-dimensional dry foams have been widely studied and simulated, yet analysis of the viscous effects present in dynamical simulations still requires further investigation.

Here we analyse the advantages and disadvantages of existing models. We include different ingredients to create a model which simulates the film evolution taking into account surfactant transport. In particular we look at the film relaxation after a T1 rearrangement. We consider the variation of surfactant concentration, and therefore the variation of surface tension, along both stretching and shrinking films. As a consequence we introduce an additional dissipative term which represents the viscous effects deriving from gradients in the surface tension and we allow surfactant transfer between adjacent films. Our model is characterized by, in addition to the time scale T_λ, two free parameters $\hat{E}$ and $\hat{\mu}$, related to elastic and viscous effects respectively. We investigate the impact of these two characteristic parameters on film evolution and estimate the flow of surfactant molecules along and between the films as a function of both $\hat{\mu}$ and the surface tension gradient.

We validate our VF+ST model by fitting experimental data. In particular we look at foaming solutions with anionic surfactants and proteins. The VF+ST model is able to describe the film length evolution for both solutions. We apply the scaling factor T_λ to the simulation results in order to match the experimental data and calculate the drag coefficient λ for both samples. Then we conduct a model optimization in order to

find the best values for the parameters $\hat{E}$ and $\hat{\mu}$. Finally we predict relevant parameters, such as Gibbs elasticity and surface viscosity, for the experimental data.

The VF+ST model can now be applied to honeycomb and disordered foams, with many interacting bubbles, subjected to different strains.

Despite the promise of our model, a further extension may be the inclusion of a model for soluble interfaces. We could also introduce and analyse the action of the disjoining pressure within the film, and hence extend our work to the case of wet foams.

The film characterization proposed here can be extended to the foam scale. As Cantat *et al.* [14] highlight, in a fast-flowing foam the viscous dissipation due to the tangential velocity of surfactant molecules is not negligible. Our model can be used to investigate foams flowing at high velocities.

Chapter 3

Foam rheology with the VF+ST model

3.1 Introduction

Aqueous foams are visco-elasto-plastic materials. Although, many studies and simulations about foam's quasi-static regime already exist, there are still many characteristic behaviours to investigate in the case of a dynamical regime, which is as well a useful case of study [49].

Soft glassy materials such as emulsions, microgels, granular materials, colloidal suspensions and foams, when subjected to shear strain at constant shear rate, present a particular stress response. They are named yield stress materials and are characterized by a variation from a solid-like behaviour, at low shear stress, to a liquid-like one when the applied

stress is higher than a critical value [22]. The yield stress and the shear modulus are significant parameters which are used to characterize the rheological properties of such materials [71].

Moreover, a foam flowing at constant shear rate is well described by the Herschel-Bulkley constitutive law. Cantat presented a dynamical model in order to study the foam shear flow [13]. She predicted the Heschel-Bulkley coefficients and showed how the yield stress increases, due to the bubble deformation, with the shear rate. This is despite the fact that, differently from the present work, Cantat's model neglects the curvature of films.

Furthermore, when the foam is subjected to an oscillating strain it is possible to evaluate the storage and loss moduli of the foam as a function of either frequency or strain amplitude. Several experimental measurements are available in the literature on these matters [11, 52, 53, 64]. Thus, developing models which are able to predict experimental results is crucial to facilitate the investigation of the rheological properties of foam, which are important for applications in several fields, from the agro-industrial to the medical ones, as we explained in Chapter 1. With a model, for example, it is possible to decide what is happening in such a complex system and hence to adjust the experimental parameters to obtain the required properties.

In the present work we apply the VF+ST model to analyse the behaviour of ordered and disordered dry foams. The VF+ST model [74] has been described in detail in Chapter 2. In particular, the model extends the Viscous Froth model (VF) [45] introducing a Surfactant Transport model

(ST). In addition to a characteristic time-scale the model has two free parameters related to the viscous and elastic properties of the interfaces, which are defined in Section 2.4. Here we investigate how these two free parameters affect a foam's stress response for different strains and strain rates. In Section 3.2 we describe our results when the foam is subjected to simple shear strain, step strain and oscillating strain.

3.1.1 The shear stress

As mentioned in Chapter 1, the shear stress σ_{xy} gives us qualitative and quantitative information about a foam's behaviour allowing the calculation of its rheological parameters. The linear relationship between stress and strain at small strains tells us that a foam exhibits a solid-like behaviour and it allows the estimation of the elastic shear modulus. Increasing the strain the yield stress is reached, afterwards the stress relaxes to a plateau, this corresponds to the transition of the foam to a liquid-like behaviour. Starting from the plateau value it is possible to determine the yield stress.

Here the shear stress σ_{xy} is calculated by applying the formulation of Bachelor [3, 13]. Considering the resultant of the surface tensions from each segment over the total foam area A, for a foam with n bubbles we have

$$\sigma_{xy} = \frac{1}{A} \sum^{n} \sum^{i} \gamma_{n_i} l_{n_{ix}} l_{n_{iy}}, \tag{3.1}$$

where γ_{n_i} is the surface tension and $l_{n_{ix}}$ and $l_{n_{iy}}$ are the components of length of each segment i in the x and y directions respectively. The shear

stress is then normalized with a factor $\gamma_{eq}/\sqrt{A_{av}}$, where A_{av} is the average area of a single bubble in the foam. Starting from the area of each bubble we apply the ideal gas law to calculate the pressure in the bubble. For each bubble we consider $PA = w$ where w is a characteristic constant which has to be chosen big enough in order to maintain the area unvaried. In the present work we neglect the inter-bubble gas diffusion, known as coarsening, and bubble collapse (T2), therefore each bubble area is fixed. Despite this the areas of the bubbles undergoes an initial variation while the foam evolves from the Voronoi tessellation towards the equilibrated configuration, which are both plotted in Figure 3.2. Different to the system of five films which is analysed in Chapter 2, here we consider a foam and the pressure inside each bubble has to be taken in account. We therefore apply the full VF, Eq. (1.9), in which we use the pressure calculated through the ideal gas law.

3.1.2 Quasi two-dimensional foam

We consider a single layer of bubbles between two flat plates as shown in Figure 3.1. We assume that we have a foam flowing in a straight channel of width, h, and infinite length. Because the plates are flat and the distance between them, in the z direction, is negligible in comparison to the width, h, the bubbles are large compared to the depth, and as a consequence, we know that all the bubbles are prisms. Hence, the foam is identical at the contact with both plates and we can model the quasi two-dimensional foam as a purely two-dimensional system.

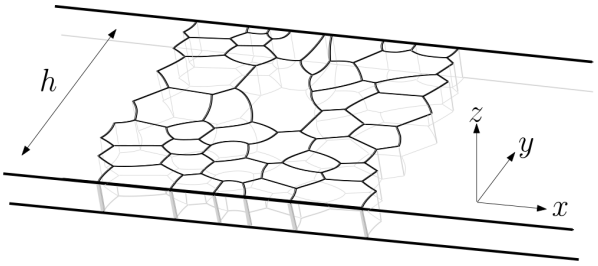

FIGURE 3.1: Two-dimensional dry foam between two-plates.

To create a disordered foam we start from the coordinates of n random points, and we generate a Voronoi tessellation through a dedicated Python library (see Appendix A.1). The VF+ST model is then applied to the Voronoi tessellation in order to evolve the starting configuration, in Figure 3.2a, towards a more realistic layout of an equilibrated foam. Particularly, Equations (1.9) and (2.3) are used to calculate the normal and tangential component of velocity of each point along each film, while Eq. (2.4) is applied to determine the vertex dynamics. The three films which converge in each threefold vertex are found through a dedicated function which is described in Appendix A.2. Furthermore, during the relaxation the foam undergoes topological rearrangements which are implemented as described in the Appendix A.4. Hence, the model's equations lead to the relaxation of each films and, meanwhile, the macroscopic system rearranges until the final configuration of equilibrium is reached, as shown in Figure 3.2b. We successively apply different type of strains to the equilibrated foam in order to investigate its rheological properties.

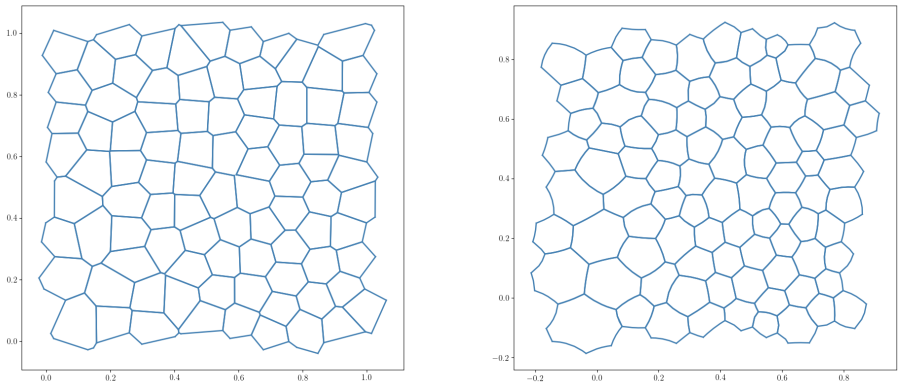

(a) (b)

FIGURE 3.2: a) Starting Voronoi tessellation. b) Starting configuration, which results from the equilibration of the foam. Note that the bubble areas change slightly in this equilibration, which is mentioned in Section 3.1.1.

3.1.2.1 The choice of boundary conditions

We use fully periodic boundary conditions (PBC), as shown in Figure 3.2 (for more informations see Appendix A.3). Nevertheless, we started our study applying periodic boundary condition only along the x axis, as shown in Figure 3.3.

In the case of partial periodic boundary conditions, during the starting phase of relaxation we allow slippage of the films in contact with the bottom and top boundaries, at $y = 0$ and $y = h$ respectively. In particular, we impose the angles between films and boundaries to be fixed at 90°. Then, once the foam is equilibrated, we shift to a no-slip condition

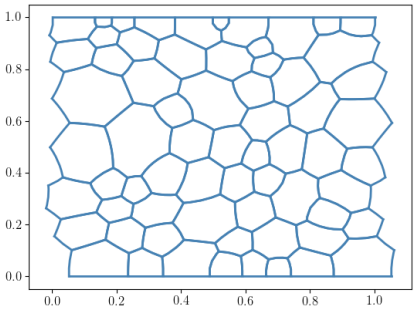

FIGURE 3.3: Starting configuration of the equilibrated foam, with periodic conditions only in the x direction.

at the boundaries $y = 0$ and $y = h$. These boundary conditions have been observed experimentally, for example, by Quilliet *et at.* who use an elastic band to confine a foam and to apply an affine strain to it [58].

The application of the 90° angle restriction at the boundaries is quite straightforward to implement. However, in our model we are considering the variation of the surface tension, or rather the displacement of surfactant molecules both along single films and across adjacent films. Looking at the distribution of the molecule concentration across the foam, we notice the presence of stagnant molecules at the boundaries. Hence, we find peaks of concentration at the boundaries which lead to negative values of the surface tension. Figure 3.4 shows the distribution of surface tension across the foam in the case of *partial* PBCs. We start with a uniform concentration of molecules in order to have a unit surface tension in the foam, as shown in Figure 3.4a. After the equilibration of the foam, the tension distribution, shown in Figure 3.4b, reaches either high or negative values at the boundaries. This behaviour is due to the displacement of

surfactant molecules across vertices. In our model we allow the exchange

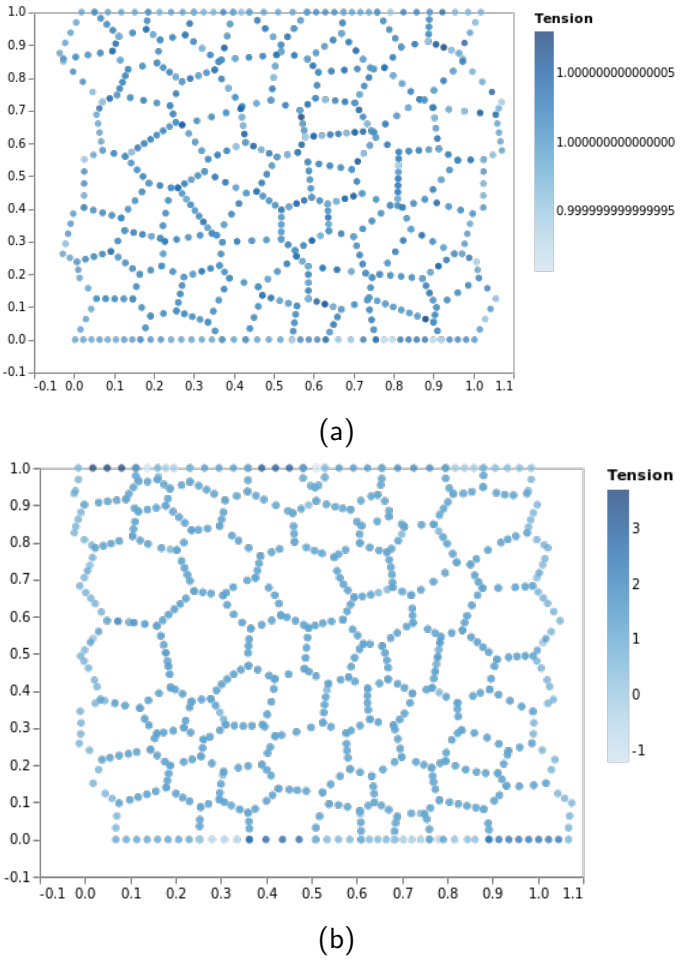

FIGURE 3.4: Foam with partial periodic boundary conditions in the x direction. a) The starting concentration of surface tension across the film is constant. b) Distribution of tension after the relaxation of the foam. At the boundaries $y = 0$ and $y = h$ the tension jumps from high values to negative values.

of molecules between adjacent films only at the vertices where three films meet.

To use the *partial* PBCs, then we would have need to introduce an additional criterion to implement the exchange of molecules between adjacent films at the boundaries. The same criterion would be necessary in order to simulate the case of a foam flowing past an object for example. On the other hand, starting from the same distribution of tension, shown in Figure 3.5a, in the case of full PBCs the variation of surface tension is never above 10^{-2}, see Figure 3.5b. Therefore, we decide to circumvent the issue of the surfactant molecule concentrations at the boundaries and to switch to full periodic boundary conditions, which are usually preferred for several type of simulations in order to avoid singularities at the borders. Nevertheless, further analysis of the constrained boundary condition could be interesting as a future step of the project.

Although the amplitude of the fluctuation of surface tension, in Figure 3.5b, might appear negligible, in the following sections, we investigate how the variation of tension affects the macroscopic behaviour of the foam, in terms of topological rearrangements and shear stress.

3.1.3 The applied strain

Once we have an equilibrated foam, we want to apply a deformation and study the response of the system. We consider three possible strains, simple shear, step strain and oscillatory strain, in order to predict rheological parameters for foams under different conditions.

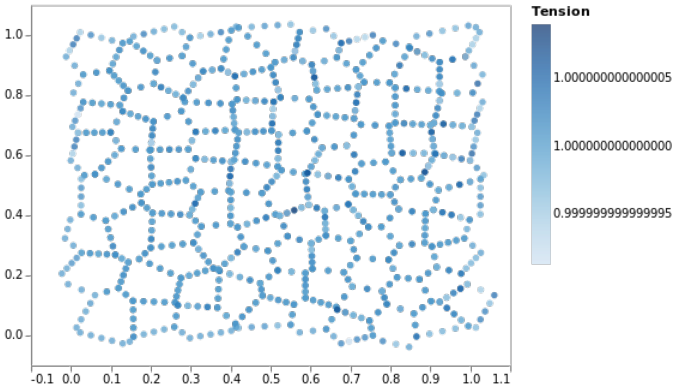

(a)

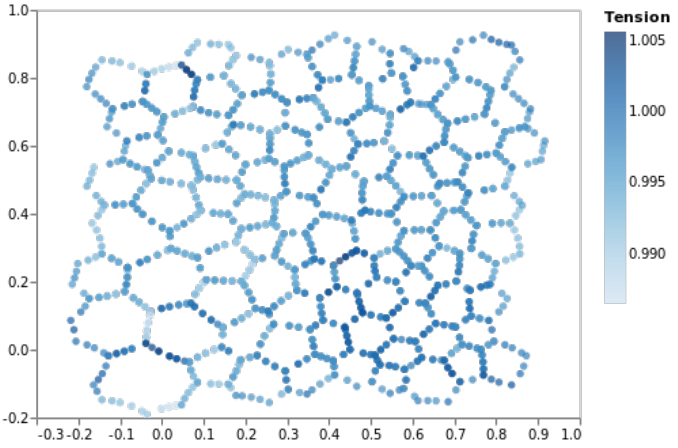

(b)

FIGURE 3.5: Foam with full periodic boundary conditions. a) Starting concentration of surface tension across the film. b) Distribution of tension after the relaxation of the foam.

Simple shear strain, ε_x, is applied with reference to the matrix of affine deformation which, in the case of simple shear, leads to the following simple linear system:

$$\begin{bmatrix} 1 & \varepsilon_x \\ 0 & 1 \end{bmatrix} \begin{bmatrix} x \\ y \end{bmatrix} = \begin{bmatrix} x + y\varepsilon_x \\ y \end{bmatrix}. \tag{3.2}$$

We are referring to a discrete node of the tessellation at $(x,\ y)$ and we determine its new position after the shear strain ε_x is applied. From Eq. (3.2), we calculate, at each iteration i, the new coordinate for each single node of the foam as follows:

$$x_i = x_{i-1} + y_i(\varepsilon_{x_i}), \tag{3.3}$$

$$y_i = y_{i-1}. \tag{3.4}$$

Nonetheless, the sheared structure is not exactly the stretched version of the initial configuration, the length of the films is redefined at each iteration evolving to the equilibrium configuration with the equilibrium 120° angles. As a consequence the deformation can not be defined as an affine deformation [71].

Imposing a time step, Δt, and the final amplitude of the strain we can calculate the shear rates, $\dot{\varepsilon} = \varepsilon_x/\Delta t$, and implement different shear rates, $\dot{\varepsilon}$, as we show in Section 3.2.1.

Furthermore, the same linear system, in Eq. (3.2), is considered to study the response of the foam to oscillating strain. In particular, we apply a sinusoidal strain of amplitude ε_0 and angular velocity $\omega = 2\pi f$, where f

is the frequency of the oscillation. The strain is therefore written as $\varepsilon_x = \varepsilon_0 \sin(\omega t)$, which corresponds to an angle of oscillation $\theta = \arctan(\varepsilon_x/h)$. In this case we decide to vary the amplitude of the final strain ε_0 or the frequency of the oscillation, in order to study the response of the foam under different conditions, as we show in Sections 3.2.5.1 and 3.2.5.2.

3.2 Results

3.2.1 Simple shear

As a first step, we strain the equilibrated foam at constant strain rate $\dot{\varepsilon}$. We choose a range of values for the shear rate between 0.1 and 1 in order to investigate the response of a foam in a dynamical regime; then the shear time-scale is in the range 1 to 10. The intrinsic time scale $T_\lambda \sim 0.1$ hence the relaxation within the foam is faster than the applied shear. Considering lower shear rates would lead to the opposite situation in which the shear happens faster than the relaxation in the foam. This condition implies that the foam does not have enough time to relax, on the other hand values of $\dot{\varepsilon}$ much higher than 1 would lead to a relaxation too much slower than the applied strain.

Fig. 3.6 shows the normalized component of shear stress, σ_{xy}, calculated through Eq. (3.1), as a function of the strain, ε, at different shear rates, $\dot{\varepsilon}$. In particular, we compare the results for two foams of different size, on the left side of Figure 3.6 a foam of 320 bubbles while on the right side a smaller foam of 15 bubbles.

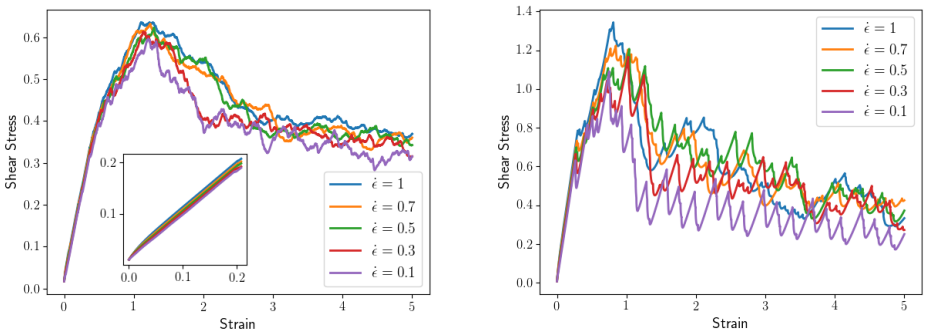

FIGURE 3.6: Shear stress within a dry foam subjected to steady shear at different shear rates $\dot{\varepsilon}$. The shear stress is normalized by the factor $\gamma_{eq}/\sqrt{A_{av}}$ and plotted against the strain. The elastic and drag parameters are $\hat{E} = 2$ and $\hat{\mu} = 1$ respectively. a) Shear stress versus strain for 320 bubbles, the insert show the stress-strain curves at small strain. b) Results for a foam of 15 bubbles.

Divoux *et al.* [22] explain that yield stress materials, such as foams, when subjected to shear strain exhibit a linear increase of shear stress at small strains. Divoux gained a deeper insight of the bulk behaviour by observing the velocity profile, in the case of carbopol microgel. They found that the initial regime, when the shear stress increases, does not correspond to purely elastic deformations but also plastic events, or rather non reversible deformations, may occur. In the inset of Figure 3.6a, we show how in our case there are no plastic events at small strain and we therefore assume the foam to be purely elastic in the starting regime.

At higher deformations, the stress reaches a maximum value, σ_M, and then it slowly decreases towards steady state or a fluid-like response. Similar stress overshoot phenomena are exhibited by all "jammed" materials

with complex microstructure which constitute soft deformable objects, like wet foams and emulsions. Divoux *et al.* [22] investigated the interplay between shear and the microstructure during this stress regime. They claimed that in such materials the maximum shear stress corresponds to the nucleation of a thin lubrication layer at the moving wall. Overall, Divoux highlighted that in quasi-static regimes, when $\dot{\varepsilon} < 10^{-3}$, σ_M remains roughly constant and independent of $\dot{\varepsilon}$, while, in the case of higher shear rates, σ_M increases as a weak power of $\dot{\varepsilon}$.

In the specific case of foams, the maximum shear stress, σ_M, has been found to increase with the gas volume fraction [46]. The stress overshoot has been observed in quasi-static regime and has been confirmed by Surface Evolver simulations [60], nevertheless, it is much more pronounced at high shear rates. At higher shear rate the dissipations in the foam delay the topological rearrangements, while after the stress reaches a maximum value the T1 events begin leading to the relaxation of the foam structure, hence, the stress decreases towards the plateau [14].

The present work exclusively focuses on dry foams in a non quasi-static regime. As shown in Figure 3.6, the shear stress exhibits an initial elastic regime at small strain. Moving to higher strains, we observe the overshoot phenomenon, and a variation of the maximum value of the shear stress σ_M, which increases with the shear rate, $\dot{\varepsilon}$. Afterwords, the shear stress decreases towards a plateau value.

Figure 3.6 shows how, the level of fluctuation in the shear stress decreases considering bigger foams. Indeed, the shear stress calculated from 320 bubbles foam is visibly smoother than the shear stress obtained for 15

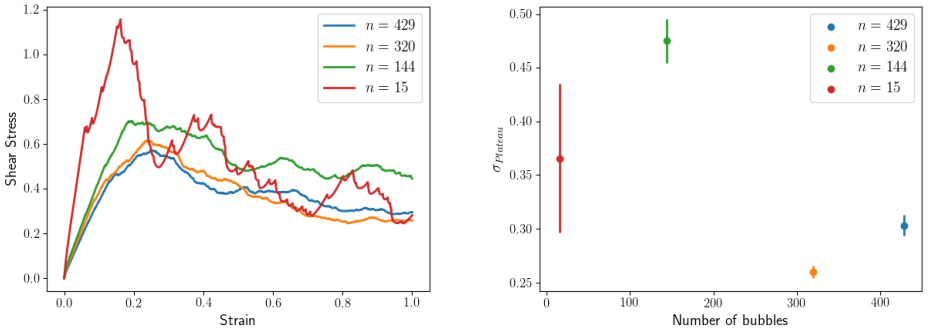

FIGURE 3.7: a) Shear stress against strain ε. The shear stress is normalized by the factor $\gamma_{eq}/\sqrt{A_{av}}$, while the strain is normalized with the final value of the applied deformation. The results are related to four foams of 15, 144, 320 and 429 bubbles. The elastic and drag parameters are relatively $\hat{E} = 2$ and $\hat{\mu} = 1$, while the shear rate is 1. b) Mean value of the shear stress for strain $\varepsilon > 0.7$. The results for the four foam are reported with the relative error bars. Note the restricted vertical scale.

bubbles but the plateau stress is about the same. In Figure 3.7a we include also the cases of bigger foams, which are made of 429 bubbles and 144 bubbles.

For the four considered foams we plot only the stress-strain curves obtained when the elastic and drag parameters are $\hat{E} = 2$ and $\hat{\mu} = 1$ and the shear rate is 1. Moreover, in Figure 3.7b we report the mean value of the shear stress when the $\varepsilon > 0.7$ for the four different foams with the related error bar.

Overall, the application of the strain to the smaller foam leads to broader and quicker elongation of the single bubbles which results in a higher

number of topological rearrangements and a more jagged shear stress. Hence, the elongation of the bubbles has an important effect on the shear stress. As a consequence, we decide to investigate and compare results related to foams of different size and polydispersity level. We characterize the polydispersity of the foam by the second moment of the distribution of the bubble area A:

$$p(A) = \left\langle \frac{A - \langle A \rangle^2}{\langle A \rangle^2} \right\rangle. \tag{3.5}$$

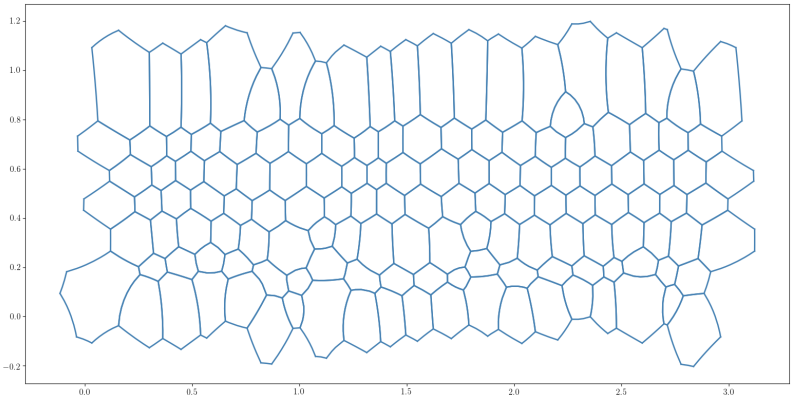

FIGURE 3.8: Foam of 144 bubbles with polydispersity $p(A) = 0.35$.

In the following Sections we analyse results related to the foams of 144 and 320 bubbles with a polydispersity of 0.35 and 0.22 respectively. The two foams of 144 and 320 bubbles are plotted in Figures 3.8 and 3.9, in particular, the first one is characterized by two rows of elongated bubbles at the top and the bottom.

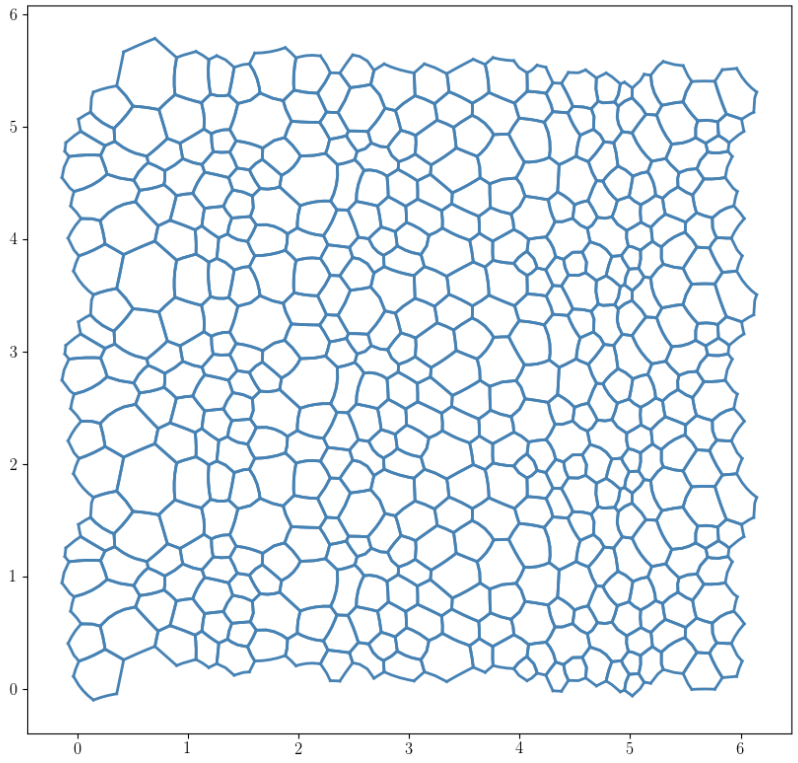

FIGURE 3.9: Foam of 320 bubbles with polydispersity $p(A) = 0.22$.

The choice of the foam size is driven by the computational performance of the simulation on a desktop pc. Considering a shear rate of 1 the simulation time is reasonably short while decreasing the shear rate to $\dot{\varepsilon} = 0.1$ the simulation for the foam of 320 bubbles takes more than 72 hours. We decide therefore to limit the present work to the analysis of relatively small foams. Increase the speed of the simulation is a future step to improve our model.

3.2.2 Does the variation of surface tension affect the shear stress?

As explained in Chapter 2, our model incorporates two parameters related to the elasticity and the surfactant drag within each film interface, which are defined in Section 2.4. As already mentioned, for quasi-static regime simulation the surface tension is usually assumed to be constant, but in the present work we allow surface tension to vary. This section therefore aims to highlight the difference between the two cases. In Figure 3.10 we plot the stress-strain curves obtained for the foam of 144 bubbles (shown in Figure 3.8). We compare the stress-strain relationship in start-up shear calculated for constant tension, which is plotted with dashed lines, with the shear stress obtained with different values of $\hat{\mu}$ and $\hat{E}$.

In the left column, Figures 3.10a, 3.10c and 3.10e, the continuous curves show how at higher values of Gibbs elasticity, which in our model is related to the parameter $\hat{E}$, the shear stress is reduced for given strain.

The elasticity of the films affects the surface tension, through Eq. (2.1), modifying the structure of the foam and the distribution of T1 events, see Figure 3.18b. Reducing our parameter $\hat{E}$, we move back towards the condition of a uniformly distributed tension, as shown in Figure 3.10e.

The same behaviour is observed by decreasing the surfactant drag parameter $\hat{\mu}$: when $\hat{\mu} = 1.5$ the shear stress almost overlaps the case of uniform surface tension, as Figure 3.10b shows, while reducing $\hat{\mu}$ and therefore reducing the drag effect due to the surfactant molecules in the film, we observe a gap between the shear stress and the case of constant surface tension, as shown in Figure 3.10f. In Figure 3.11 we report the results that we obtain with the foam of 320 bubbles. We find equivalent trends varying the elastic parameter $\hat{E}$, while the effect of the surfactant drag parameter $\hat{\mu}$ is less pronounced.

Starting from the shear stress we calculate rheological parameters that encapsulate a foam's behaviour. In particular, in the next section we present our results for the elastic shear modulus, G', and the yield stress σ_Y, which are calculated by varying the shear rate $\dot{\varepsilon}$ between 0.1 and 1.

3.2.3 Linear rheology

In order to study the viscoelasticity of foam structures we define two quantities, which are also valid for polymers as well as cellular tissues, of strain and stress in a medium regarded as a continuum [30]. In the case of simple shear the constitutive equation for linear viscoelasticity, which connects the strain ε_{xy} and the stress σ_{xy}, considers the additive effect of

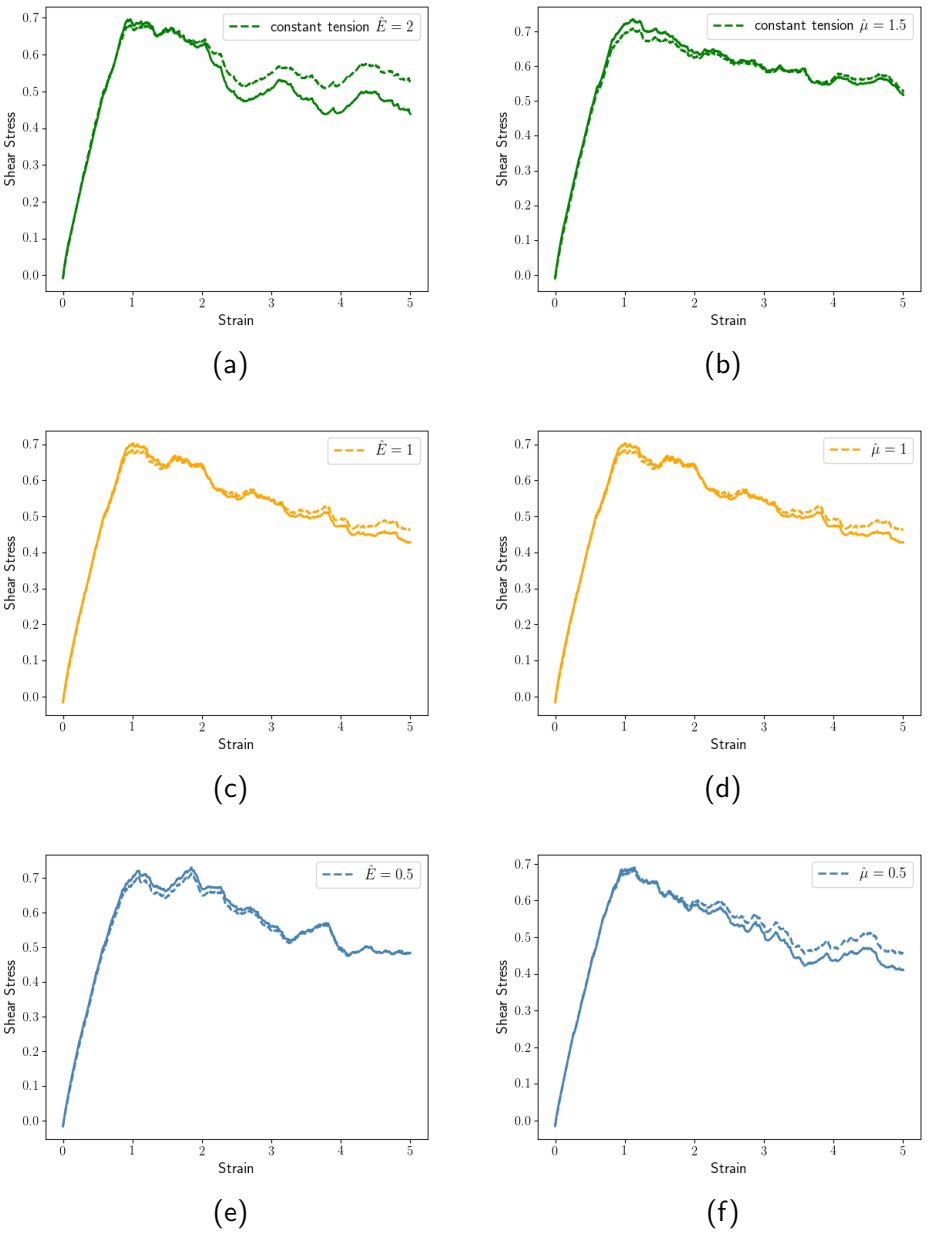

FIGURE 3.10: Shear stress versus strain for a dry foam of 144 bubbles subjected to steady shear at the shear rate $\dot{\varepsilon} = 1$. The shear stress is normalized by the factor $\gamma_{eq}/\sqrt{A_{av}}$. The dashed line is the shear stress that we calculate neglecting any variation of the surface tension. a) c) e) Shear stress obtained for $\hat{\mu} = 1$ and varying $\hat{E}$ from 2 to 0.5. b) d) f) Shear stress calculated for $\hat{E} = 1$ and varying $\hat{\mu}$ from 1.5 to 0.5. The plots show how higher elasticity and lower surfactant drag act to reduce the shear stress in the foam.

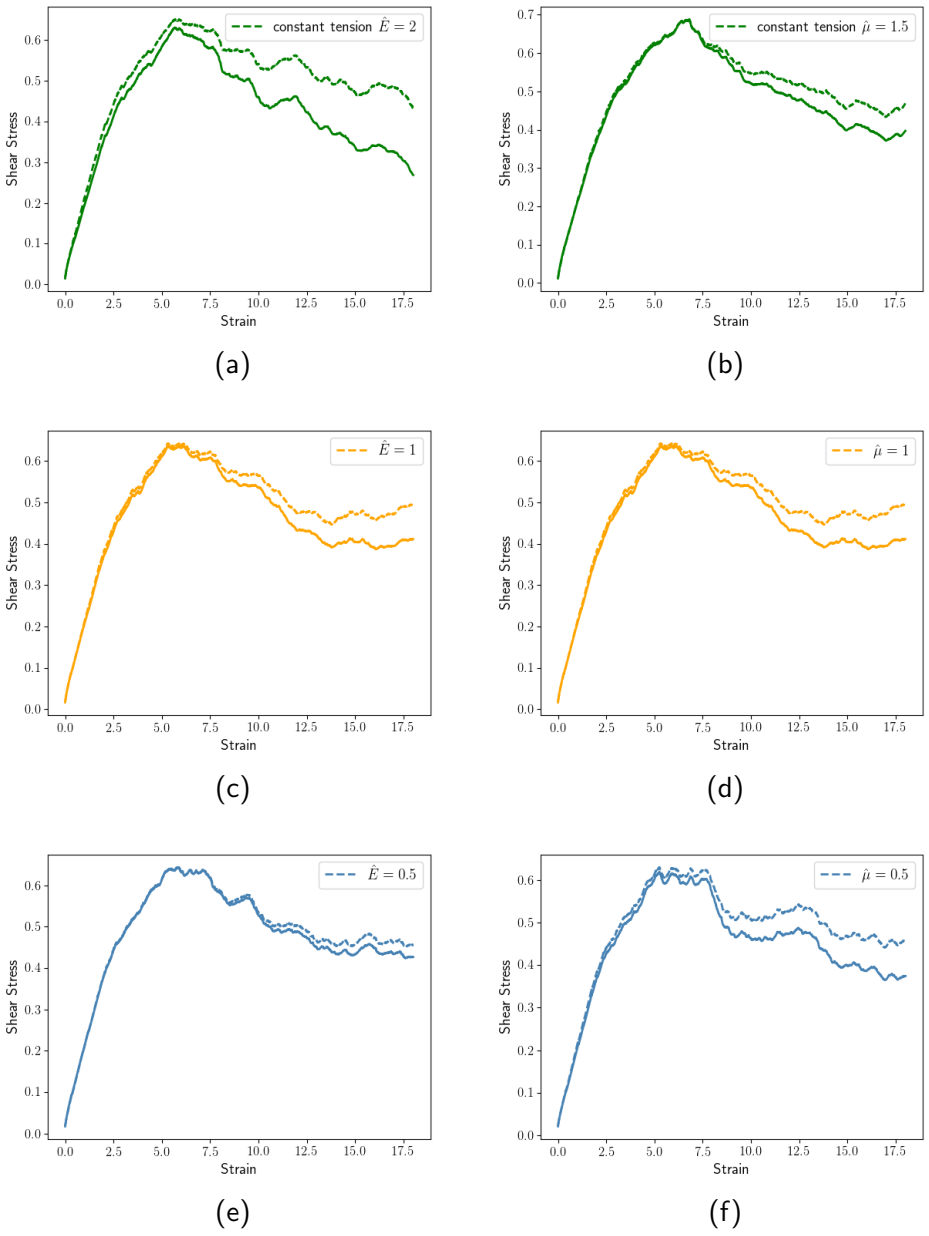

FIGURE 3.11: Shear stress versus strain for a dry foam of 320 bubbles subjected to steady shear at the shear rate $\dot{\varepsilon} = 1$. Notation and other simulation details as for Figure 3.10.

sequential changes,

$$\sigma_{xy} = \int_{-\infty}^{t} G(t-t')\dot{\varepsilon}_{xy}(t')dt', \tag{3.6}$$

where $G(t-t')$ is the relaxation modulus. When the strain is imposed within a short period at a constant shear rate the constitutive Eq. (3.6) is reduced to the following form

$$\sigma_{xy}(t) = \varepsilon_{xy} G'(t). \tag{3.7}$$

The ratio between the stress and the corresponding strain is called the elastic modulus, G', and the material behaves as an elastic matter. As mentioned in Chapter 1, complex fluids exhibit an elastic behaviour only at small strain, as shown in Figure 3.6. Hence, at small strain the relation between stress and strain in our numerical simulation is linear and the foam behaves like an elastic solid, therefore we can calculate the shear elastic modulus G' through Eq. (3.7).

3.2.3.1 Elastic Shear Modulus

We consider the slopes of the stress-strain curves at small deformations to calculate the shear elastic modulus G' through Eq. (3.7). We carry out the fit of the data through a dedicated python optimization tool (*scipy.optimize.curve-fit*).

In this section we report the results obtained for the foam of 320 bubbles, we look at the stress-strain curves estimated for various shear rates $\dot{\varepsilon}$,

plotted in Figure 3.6a, considering the stress for strain $\varepsilon < 0.2$. Fig. 3.12 shows the elastic shear modulus against the shear rate. In particular, in Figure 3.12a we plot the results obtained setting $\hat{\mu} = 1$ and varying $\hat{E}$, vice versa, in Figure 3.12b we show the elastic shear moduli obtained when $\hat{E} = 1$ and $\hat{\mu}$ is varied.

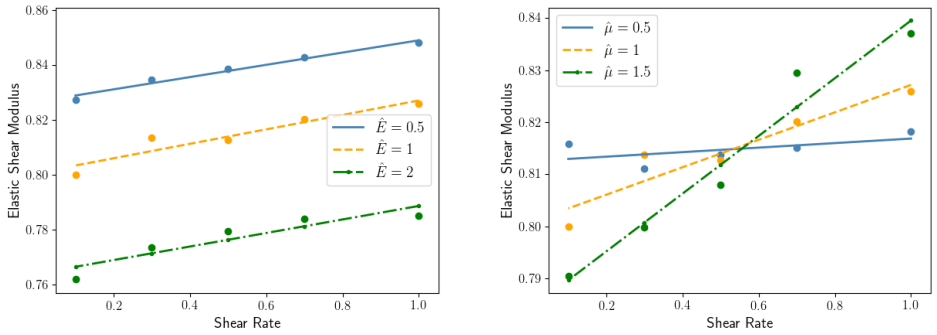

FIGURE 3.12: Elastic shear modulus versus shear rate for a disordered dry foam of 320 bubbles and polydispersity p(A)=0.22, the linear fit are also plotted. a) We set the surfactant drag parameter $\hat{\mu} = 1$ and vary $\hat{E}$ between 0.5 and 2. b) We set the elastic parameter $\hat{E} = 1$ and vary $\hat{\mu}$ between 0.5 and 1.5.

We apply a linear fit to the elastic shear moduli versus shear rate, we plot the results in Figure 3.12. Finally we extract the slopes of the lines and we report them in Figure 3.13 versus the two parameters $\hat{E}$ and $\hat{\mu}$.

The slopes of the lines in Figure 3.12a are not significantly affected by the elastic parameter. Vice versa in Figure 3.12b the slopes of the lines slightly increase with the surfactant drag coefficient.

We decide to report also the results that we obtain for the foam of 144 bubbles and higher polydispersity , in Figure 3.13. In this case we notice that not only decreasing the surfactant drag but also assigning higher elasticity to the films makes the foam behaviour at small strain less dependent on the shear rate. This suggests that increasing the viscosity of the foam or decreasing the elasticity the foam behaviour will depend more on the shear rate, particularly in case of foams with higher polydispersity.

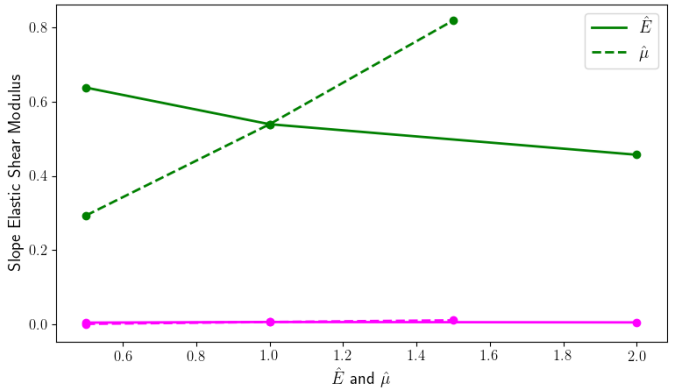

FIGURE 3.13: Slopes of the lines which fit the Elastic shear modulus versus the shear rate, varying the parameters $\hat{E}$ and $\hat{\mu}$. Magenta and green lines are the results for the foams of 320 and 144 bubbles respectively.

For a honeycomb foam the shear modulus can be predicted with the formulation available in literature $G' = \gamma/\sqrt{3}l$, where γ is the surface tension of the films and l the lenght of the sides of the hexagons [71]. Several numerical results exist in literature, in particular Princen [57] found, in the case of a hexagonal foam with negligible film thickness, the shear stress to be proportional to the ratio γ/R_h, where R_h is the

radius of the circle inscribed within a single hexagon. Moreover, Princen readily derived the elastic shear modulus for small stresses, i.e., in the region which precedes the yielding, where the foam can be approximated as a purely elastic material. Princen also found that the elastic shear modulus can be rescaled with the same factor γ/R_h.

In the present work we consider a disordered foam with a polydispersity of 0.22. Cox and Whittick [18] showed that the shear modulus of a foam decreases with increasing the disorder. For our disordered foam the shear modulus is expected to be slightly lower than for a honeycomb. Considering the average length of the films of 0.2 we predict the shear modulus for our foam, through the $G' = \gamma/\sqrt{3}\langle l \rangle$. After normalizing the results with the Laplace pressure $\gamma_{eq}/\sqrt{A_{av}}$, where the average area $A_{av} = 0.09$, we calculate $G' = 0.86$. The results of our simulation shown in figure 3.12 are slightly lower than the predicted value and they are in agreement with the results obtained with Surface Evolver simulations [18].

We conclude that the response of a disordered foam which is less elastic or more viscous, is more significantly affected by the rate of application of the shear, particularly in case of foams with higher polydispersity.

3.2.3.2 Yield stress

At larger strains the stress-strain curve is quite jagged, as shown in Figure 3.6. We calculate the mean and standard deviation for the curves for strains $\varepsilon > 2$, considering the disordered foam of 320 bubbles. In Figure

3.14 the results are plotted together with the related error bars against the shear rate $\dot{\varepsilon}$.

As we already mentioned in Chapter 1, the Herschel-Bulkley constitutive equation, $\sigma = \sigma_Y + \alpha\dot{\varepsilon}^{\beta}$, is often used in relation to foams.

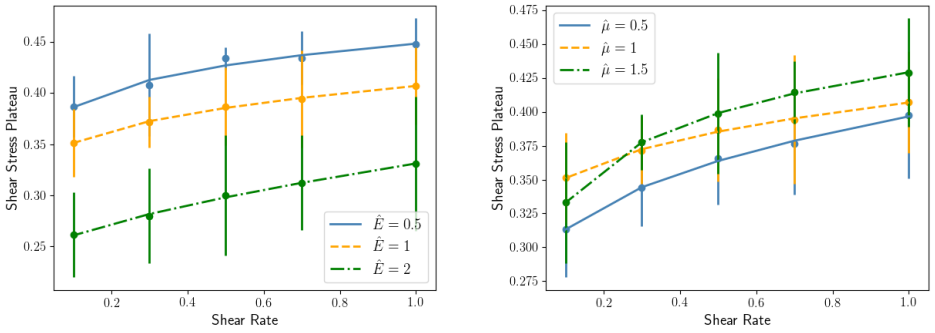

FIGURE 3.14: The mean values of the normalized shear stress plateau, $\varepsilon > 2$, are reported against the shear rate, for the foam of 320 bubbles. Each result is obtained fixing $\hat{\mu}$ and $\hat{E}$ but varying $\dot{\varepsilon}$. The results are fitted with the Herschel-Bulkley law. a) We set the surfactant drag parameter $\hat{\mu} = 1$ and vary $\hat{E}$ between 0.5 and 2. b) We set the elastic parameter $\hat{E} = 1$ and vary $\hat{\mu}$ between 0.5 and 1.5.

According to the Herschel-Bulkley law, the shear stress can be decoupled into two components: a rate-independent variable, σ_Y, the yield stress or elastic stress, and a rate-dependent component $\alpha\dot{\varepsilon}^{\beta}$ [21]. The latter term involves the foam consistency α and the power law index β. Considering uni-axial deformation of a foam with small amplitudes, Schwartz and Princen [68] found a value for the power law index of $\beta = 2/3$, similar to the value predicted by Cantat in case of simple shear [14], while in

the case of sheared emulsions Princen and Kiss [57] found $\beta = 1/2$. Our predictions for the yield stress σ_Y, the consistency α and the power β are reported in Table 3.1.

TABLE 3.1: Yield stress, σ_Y, consistency α and the power β predicted for the Herschel-Bulkley equation for the foam of 320 bubbles.

$\hat{E}$	σ_Y	α	β
0.5	0.25	0.19	0.16
1	0.30	0.10	0.33
2	0.24	0.09	0.67

$\hat{\mu}$	σ_Y	α	β
0.5	0.25	0.14	0.36
1	0.30	0.10	0.33
1.5	-0.47	0.90	0.05
1.5	0.34	0.07	0.70

Setting $\hat{\mu} = 1$ and varying $\hat{E}$ we find the values in Figure 3.14a. On the left side of Table 3.1 we summarize the values predicted for the three curves in Figure 3.14a. We estimate the yield stress σ_Y, the consistency α and the power β applying the Herschel-Bulkley model to fit the data.

The yield stress, which in our results oscillates around 0.28, is smaller than the stress at the plateau (for $\varepsilon > 2$) confirming that at high strain the foam has a fluid-like behaviour. The power β is smaller than one indicating that we are dealing with a shear-thinning fluid [49]. Furthermore, β increases with $\hat{E}$ and particularly for the case of $\hat{E} = 2$ the value of β is similar to the results in literature by Princen and Kiss [57]. Vice versa, in Figure 3.14b we plot the results obtained setting $\hat{E} = 1$ and varying $\hat{\mu}$. Again the data are fitted through the Herschel-Bulkley equation. In terms of yield stress we find an anomalous value when $\hat{\mu} = 1.5$. This discrepancy is due to the average of the shear stress plateau, which as shown in Figure 3.14b, when $\dot{\varepsilon} = 0.1$ is smaller than we would expect consistently with the other two cases. Excluding the shear stress for

$\dot{\varepsilon} = 0.1$ from the fit we obtain the values which are reported in the last row on the right side of the Table 3.1.

3.2.3.3 T1 distribution

In order to highlight further the effect of our free parameters $\hat{E}$ and $\hat{\mu}$ on the foam flow, we investigate the variation of T1 distribution. In Figure 3.15, we plot the cumulative number of T1s versus strain, when the foam of 320 bubbles is sheared at constant shear rate, $\dot{\varepsilon} = 0.3$. The plots display how the T1 distribution is not directly affected by the parameters $\hat{E}$ and $\hat{\mu}$, respectively in Figures 3.15a and 3.15b. Hence, in both the panels in Figure 3.15 the curves are broadly similar.

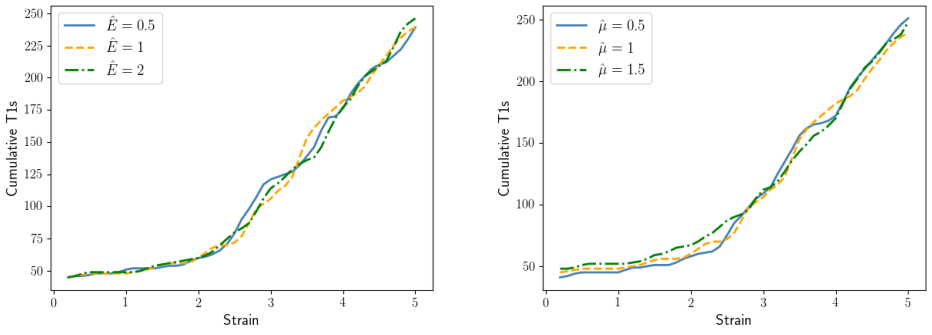

FIGURE 3.15: Cumulative number of topological rearrangements (T1s) against strain with shear rate, $\dot{\varepsilon} = 0.3$, for the foam of 320 bubbles. The results, which are obtained by varying the parameters $\hat{E}$ and $\hat{\mu}$, are reported in a) and b) respectively.

We therefore decide to look at the distribution of the T1 events in time and space. Wyn *et al.* studied the localization of T1 in case of linear Couette shear flow in a channel, which is the equivalent of the case of partial periodic boundary conditions that we address in Section 3.1.2.1. They found that in the case of monodisperse foam, topological rearrangements are mostly localized in a narrow band close to the walls, analogous results have been found also for polydisperse foams [42]. Moreover, Wyn *et al.* found that T1s happen further from the wall and affect a broader band of the channel as the polydispersity of the foam increases [73]. Similarly to these results, we find that T1 events are localized in a narrow band nearby the wall, when we subject the disordered foam with partial periodic boundary conditions, in Figure 3.3, to simple shear. As expected, shearing an hexagonal foam (see Figure 3.19) we observe the localization of T1s exactly along a straight line.

In the present Chapter we investigate the specific case of full periodic boundary condition. As a consequence, we do not consider the contact between the foam and the walls, therefore we are neglecting the related friction effects and we would expect to find a more uniform distribution of T1 events. Nevertheless, as explained by Wyn *et al.*, the localization of the T1 events is highly affected by the starting configuration of the foam.

Figures 3.16 and 3.17 show the location of topological rearrangements that we obtain applying a simple shear along the x axis to our foam of 320 bubbles, whose polydispersity is $p(A) = 0.22$. On the left sides of Figures 3.16 and 3.17 we plot the y coordinate of the T1s against time,

while on the right columns we plot the location of the T1s in the Cartesian plane. In particular, plotting the T1 distribution versus time we observe a localization of T1s at time zero, which is due to the initial rearrangement of the foam. Hence, starting from a Voronoi tessellation, which is generated from a random distribution of points, we find that the foam undergoes an extensive rearrangement at time zero. As a consequence, we observe a line of spots at time $t = 0$ in the left columns of Figures 3.16 and 3.17.

We investigate what happens when we set the surfactant drag parameter $\hat{\mu} = 1$ and varying $\hat{E}$ or vice versa fixing $\hat{E}$ and varying $\hat{\mu}$. The two cases are respectively plotted in Figures 3.16 and 3.17. As already shown in Figure 3.15 we find that the variation of the two parameters do not affect in a significant way the distribution of T1s.

Nonetheless, considering a different starting configuration the results are different. We consider the foam of 144 bubbles, in Figure 3.8, with a polydispersity of $p(A) = 0.35$, which presents two rows of elongated bubbles at the top and the bottom. For this configuration the topological events happen to be mostly localized at smaller and larger y coordinates, in correspondence of the elongated bubbles, as shown in Figure 3.18a where we plot the coordinates of the T1 events versus time. Furthermore, increasing the elastic parameter, $\hat{E}$, to allow a greater elongation of the bubbles, or rather, to increase the non-uniform distribution of tension in the foam, leads to a smaller number of T1 events, as Figure 3.18b shows. Finally, Figure 3.18c shows that also for this configuration the surfactant drag parameter $\hat{\mu}$ does not affect the T1 distribution.

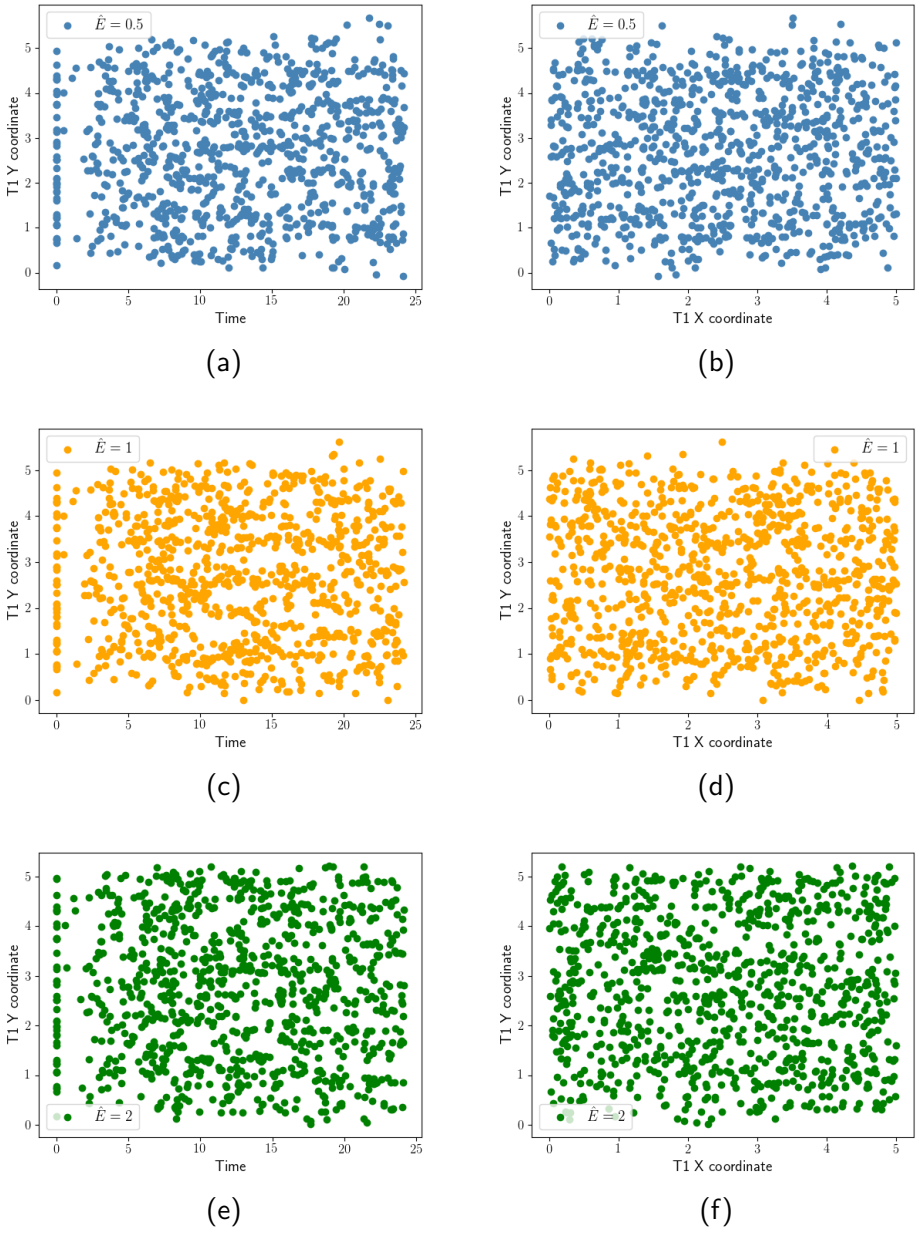

FIGURE 3.16: a) c) e) y coordinates of the topological rearrangements T1 are plotted against time. b) d) f) y coordinates versus x coordinates of T1 events. All the panels refer to the case of shear rate $\dot{\varepsilon} = 0.3$. The elastic parameter $\hat{E}$ is varied between 0.5 and 2, while $\hat{\mu} = 1$.

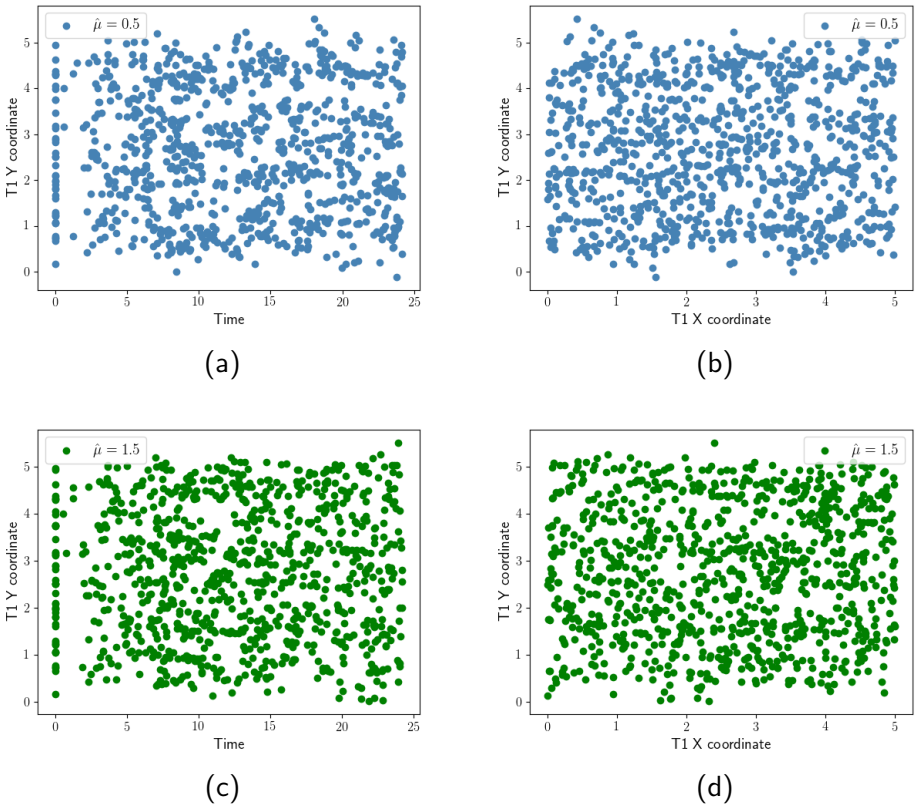

FIGURE 3.17: a) c) y coordinates of the topological rearrangements T1 are plotted against time. b) d) y coordinates versus x coordinates of T1 events. All the panels refer to the case of shear rate $\dot{\varepsilon} = 0.3$. The elastic parameter $\hat{\mu}$ is varied between 0.5 and 1.5, while $\hat{E} = 1$.

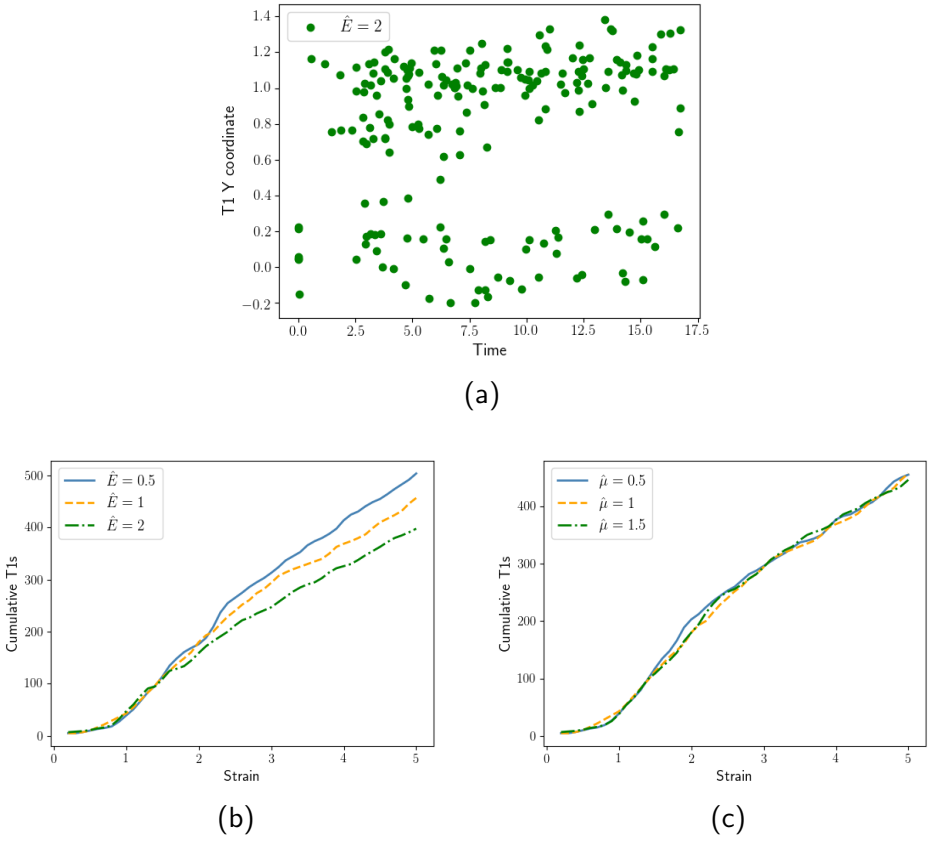

FIGURE 3.18: Results related to a foam of 144 bubbles with row of elongated bubbles at the top and the bottom. a) y coordinates of the topological rearrangements T1 plotted against time. The results refers to the case of shear rate, $\dot{\varepsilon} = 0.3$, $\hat{\mu} = 1$ and $\hat{E} = 2$. b) and c) Cumulative T1 versus strain varying the parameter $\hat{E}$ and $\hat{\mu}$ respectively.

In terms of topological rearrangement we conclude that the isotropy in the foam inhibits the effect of the parameters $\hat{E}$ and $\hat{\mu}$. In fact we observe the effect of the elastic parameter in the case of foam with higher polydispersity. Moreover, in agreement with the results in literature we find that the T1 distribution is highly affected by the initial configuration of the foam. In particular, we find that the topological rearrangements mainly happen in response to elongated bubbles.

Overall in Section 3.2.1 we carry out the calculation of rheological parameters starting from the shear stress of the foam. We investigate the effect of both the shear rate and our model parameters $\hat{E}$ and $\hat{\mu}$ on the behaviour of the foam at a macroscopic level. Foams with higher polydispersity and elongated bubbles are more clearly affected by our elastic parameter $\hat{E}$, while in foams with lower polydispersity the effect of $\hat{E}$ and $\hat{\mu}$ seems to be inhibited by the isotropy of the foam. In terms of shear rate we found, in agreement with the literature, that the maximum of the shear stress increase with $\dot{\varepsilon}$.

3.2.4 Step strain - stress relaxation experiment

To characterize a complex fluid, as we mentioned in Chapter 1, we need to know not only the shear viscosity but also other strain-rate dependent parameters as for example the shear modulus. In the present Section we demonstrate how such rheological parameters can be predicted also starting from simple experiments. Particularly we simulate the specific case of stress relaxation experiment. The experiment consists in imposing, within an extremely brief or instantaneous period of time, a constant

affine strain. Although, other kind of stress relaxation experiments exist, the step strain is more commonly performed because of its simplicity. We therefore decide to simulate such type of experiment with our model in order to predict rheological parameters of a foam.

We choose to consider an ordered foam with the highest volume fraction, $\Phi_l = 0.01$, that is a dry hexagonal foam. Here we present our results, which are obtained applying the VF+ST model to the hexagonal foam in Figure 3.19. We apply an instantaneous affine strain to the foam and then

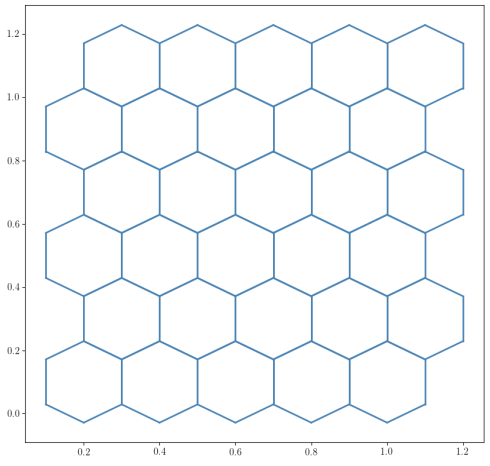

FIGURE 3.19: Hexagonal foam, used to study the step strain case.

we let the foam relax. We assume the foam to be a viscoelastic material, starting from our numerical results we calculate the shear stress, through Eq. (3.1), and successively the storage and loss moduli to quantify the energy which is stored or lost by the foam during the deformation.

Ferry illustrated how to calculate one experimentally observable function from another [30]. Particularly, in the case of viscoelastic materials the complex dynamic modulus can be derived from Eq. (3.6) through the Fourier transform. Hence, moving from time to the frequency domain the Fourier transform allows the calculation of storage and loss shear moduli, G' and G'' respectively, as a function of frequency. Then

$$G'(\omega) = G_{eq} + \omega \int_0^\infty [G(t) - G_{eq}] \sin(\omega t) \mathrm{d}t, \tag{3.8}$$

$$G''(\omega) = \omega \int_0^\infty [G(t) - G_{eq}] cos(\omega t) dt, \tag{3.9}$$

where G_{eq} is the equilibrium modulus and ω is the angular velocity dependent on the frequency f, ($\omega = 2\pi f$). As a first step, to evaluate Equations 3.8 and 3.9, we calculate the modulus function $G(t) = \sigma(t)/\varepsilon$. We deduce G_{eq} from the value of the stress at the plateau.

In the present section we evaluate the shear modulus by applying Equations 3.8 and 3.9, specifically examining a range of frequencies between 10^{-2} and 10^{1}.

3.2.4.1 How the free parameters $\hat{\mu}$ and $\hat{E}$ affect the shear stress

Figure 3.20a shows the normalized shear stress versus time after the instantaneous strain is applied to the hexagonal foam. The magnitude of the step strain has an effect on the stress, so we decide to consider a small step strain $\varepsilon_s = 0.1$. Moreover, we set $\hat{\mu} = 1$ and vary $\hat{E}$. During the foam relaxation the stress decreases towards a plateau value, with a rate

proportional to $\hat{E}$, in agreement with the results previously described in Chapter 2.

In Figure 3.20b, we plot the shear moduli, obtained through Eq. (3.8) and (3.9), against the frequency on logarithmic axes. The evolution of G' and G'' in Figure 3.20b agrees with the typical behaviour of viscoelastic materials, for example experimental measurements for emulsions [11] and Gilette shaving cream [37]. Similarly to the experimental results we find that at small frequencies the storage modulus is almost constant while the loss modulus increases with frequency. In addition, our model allows the prediction of the shear moduli for higher frequencies, values which are often difficult to measure experimentally. We find that increasing the frequency the storage modulus slightly increases while the loss modulus drops to smaller amplitude.

For concentrated emulsions, Bressy *et al.* detected an increase of both storage and loss modulus with the emulsion concentration [11]. Here we report the results obtained through the application of our VF+ST model. As explained in Chapter 2, the VF+ST model leads to lower tensions, which correspond to higher concentration of surfactants, as soon as $\hat{E}$ drops, due to Eq. (2.1). As a consequence, we would expect to find greater values of the moduli G' and G'' when decreasing $\hat{E}$. Nevertheless, we observe a similar trend only for frequencies < 1, shown in Figure 3.20b.

Regarding the variation of the surfactant drag parameter, increasing $\hat{\mu}$ slows down the relaxation of the foam, leading to a slower evolution of the stress towards the final plateau value. In Figure 3.21a we plot the

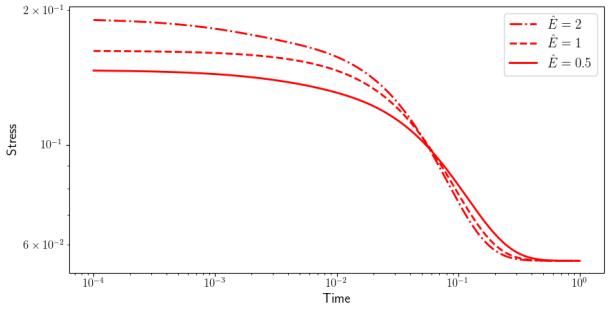

(a)

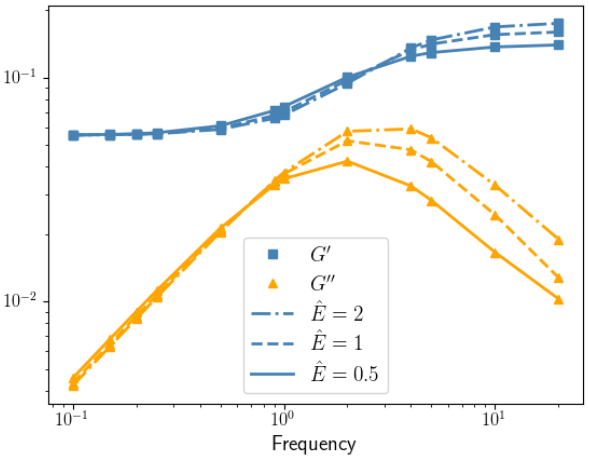

(b)

FIGURE 3.20: Effect of elastic parameter $\hat{E}$ when $\hat{\mu} = 1$. a) Shear stress of a hexagonal foam subjected to step strain $\varepsilon = 0.1$. b) Shear moduli obtained through a Fourier transform.

normalized shear stress versus the time, showing how the plateau value of the stress is approached more slowly for higher $\hat{\mu}$.

In Figure 3.21b we show the storage and loss moduli versus frequency in logarithmic axes. In this case, we set $\hat{E} = 1$ and vary $\hat{\mu}$ in order to investigate the effect of the surfactant drag on the shear moduli. When the surfactant drag increases, the VF+ST model leads to higher tension on stretching films and lower tension on shrinking films [74]. In a flowing foam, clearly, both phenomena occur and overall increases in the surfactant drag parameter $\hat{\mu}$ tend to slow down the foam relaxation. As a consequence, the shear stress approaches more slowly to the final plateau, as in Figure 3.21a. Similarly to the previous case, starting from the shear stress we calculate the storage and loss moduli through Equations 3.8 and 3.9. The results, in Figure 3.21b, exhibit how increasing the surfactant drag the storage and loss moduli maintain the same shape and are shifted to the left. Hence, the reduction of $\hat{\mu}$ acts to delay the characteristic loss and storage in the foam. The effects of surfactant drag are less well explored in terms of experimental results than other parameters and therefore it is not straightforward to compare our numerical results with real data.

Finally, in order to estimate the precision of our numerical calculation we fit the relaxation function $[G(t) - G_{eq}]$, in Eq. (3.8), with a negative exponential function. We calculate the exact integrals in Eq. (3.8) and Eq. (3.9) and verify the precision of our numerical solution which results to be of the order of 10^{-8}.

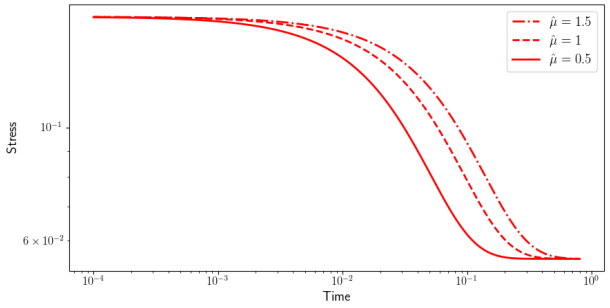

(a)

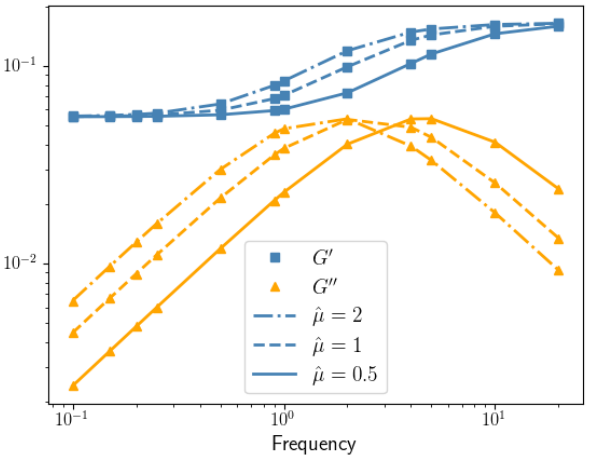

(b)

FIGURE 3.21: Effect of surfactant drag parameter $\hat{\mu}$ when $\hat{E} = 1$. a) Shear stress of a hexagonal foam subjected to step strain. b) Shear modulus obtained through the Fourier transform.

3.2.4.2 The case of a disordered foam

In Figures 3.22 and 3.23 we plot the normalized shear stresses and the shear moduli obtained when a disordered foam is subjected to a step strain $\varepsilon_s = 0.1$. Due to the topological rearrangements in the foam the shear stresses and the shear moduli are not smooth. On the other hand, the overall trends caused by the variation of $\hat{E}$, in Figure 3.22, and $\hat{\mu}$, in Figure 3.23, are in agreement with the results calculated for the hexagonal foam.

3.2.5 Oscillating strain

3.2.5.1 Shear moduli as a function of frequency

Experiments show that when an oscillating deformation $\varepsilon = \varepsilon_0 \sin(\omega t)$, where ε_0 is the maximum strain amplitude, is applied, if the material presents a linear viscoelastic behaviour, the corresponding stress is a sinusoidal function of amplitude σ_0 shifted by an angle δ , $\sigma = \sigma_0 \sin(\omega t + \delta)$. Thus, considering the sinusoidal strain ε, we calculate $\dot{\varepsilon} = \omega \varepsilon_0 \cos(\omega t)$ and substitute it in the constitutive equation Eq. (3.6) obtaining the two frequency dependent functions

$$\sigma(t) = \varepsilon_0 (G' \sin(\omega t) + G'' \cos(\omega t)). \tag{3.10}$$

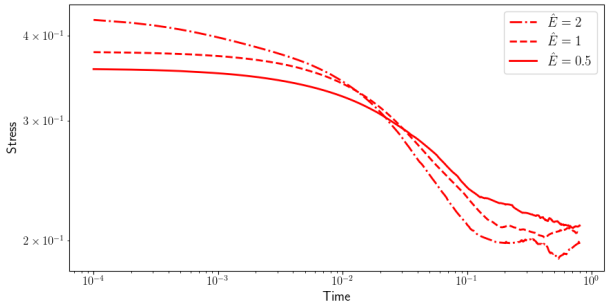

(a)

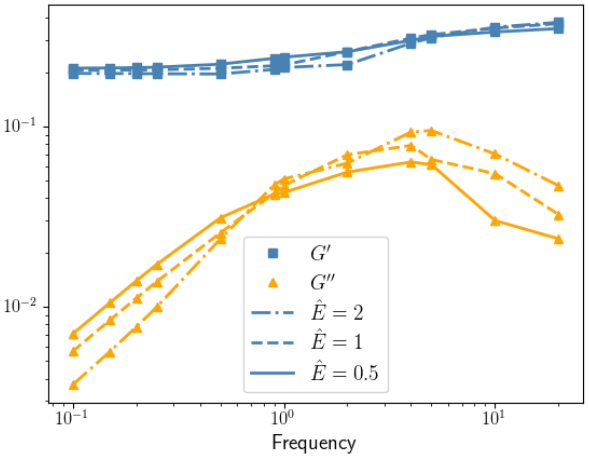

(b)

FIGURE 3.22: Effect of elastic parameter $\hat{E}$ when $\hat{\mu} = 1$. a) Shear stress of a disordered foam subjected to step strain $\varepsilon_s = 0.1$. b) Shear moduli obtained through a Fourier transform.

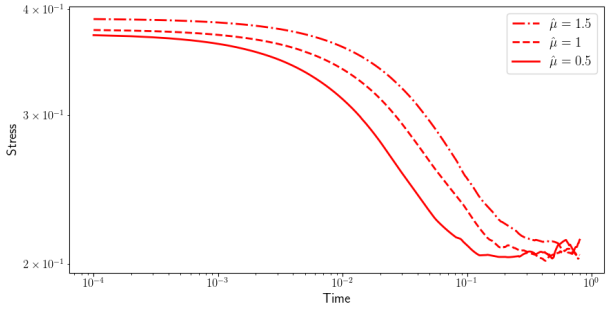

(a)

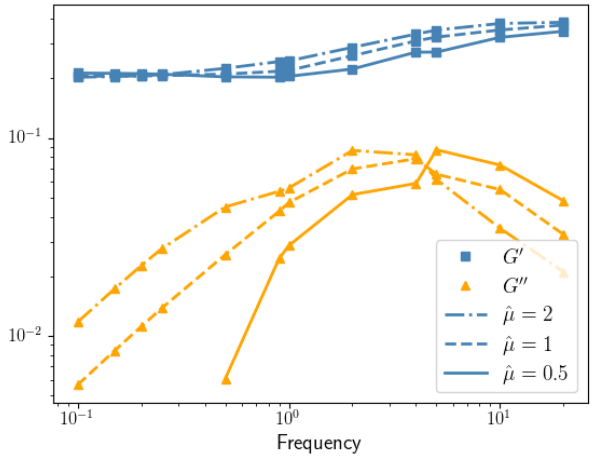

(b)

FIGURE 3.23: Effect of surfactant drag parameter $\hat{\mu}$ when $\hat{E} = 1$. a) Shear stress of a disordered foam subjected to step strain $\varepsilon_s = 0.1$. b) Shear modulus obtained through the Fourier transform.

We then write the storage and loss modulus respectively as

$$G' = \frac{\sigma_0}{\varepsilon_0}\sin(\delta),\ G'' = \frac{\sigma_0}{\varepsilon_0}\cos(\delta). \tag{3.11}$$

Starting from a disordered foam at equilibrium we apply an oscillating deformation, through Eq. (3.3), and we calculate the corresponding shear stress, by means of Eq. (3.1). By fitting the numerical shear stress with a sinusoidal function we find the unknown variables σ_0 and δ, and deduce the shear moduli through Equations (3.11).

Considering the same range of frequencies of the previous section we analyse the shear modulus for a disordered foam subjected to an oscillating strain.

In Figure 3.24a we plot the normalized shear stress as a function of time, when the frequency of oscillation is varied between 0.1 and 10, while the maximum strain amplitude, ε_0, is unitary. In particular, we consider two periods of oscillation, in order to neglect the initial transient of the first period. Figure 3.24a shows how after the plastic events at small times, the foam starts to behave like an elastic material. As a consequence, the hysteresis cycle of the foam exhibits an elliptic shape, as shown in Figure 3.24b, where we plot the shear stresses versus strain considering only the second period of oscillation. We are therefore able to fit the shear stress with a sinusoidal function and calculate the storage and loss moduli through Equations 3.11. Moreover, the elliptical shape of the hysteresis cycle confirms the viscoelastic behaviour of the foam and tells

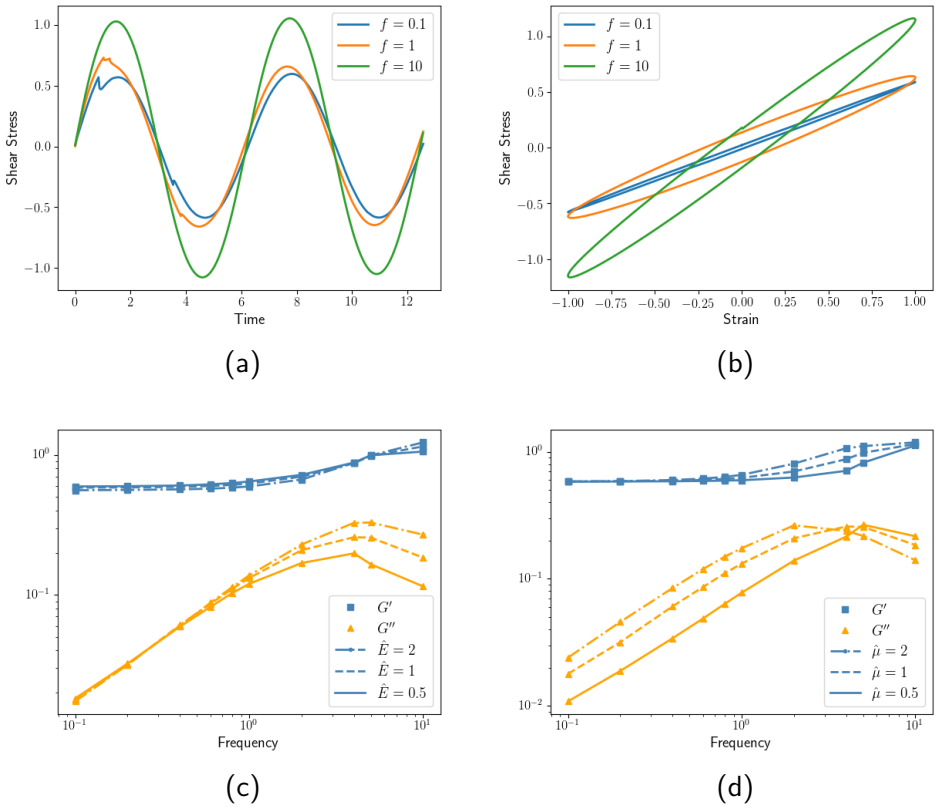

FIGURE 3.24: a) Normalized shear stress versus time. The maximum amplitude of the strain, ε_0, is unitary while the frequency (f) of oscillation is varied between 0.1 and 10. The elastic and drag parameters are relatively $\hat{E} = 1$ and $\hat{\mu} = 1$. b) Hysteresis cycles for different frequencies. c) d) Shear moduli against frequency, calculated varying the two parameters, $\hat{E}$ and $\hat{\mu}$. b) c) and d) are related to the second period of oscillation.

us that the dissipation of the elastic foam is predominantly of viscous origin.

Figures 3.24c and 3.24d show the storage and loss moduli as function of frequency, relatively when $\hat{\mu} = 1$ and $\hat{E}$ is varied or vice versa, $\hat{E}$ is set to unity and $\hat{\mu}$ is varied. The last results agree with the values we found for the case of hexagonal foam subjected to step strain, see Figures 3.20 and 3.21. Hence, increasing the elastic parameter $\hat{E}$ increases the modulus of the loss modulus at high frequencies, Figure 3.24c, while decreasing the surfactant drag $\hat{\mu}$ reduces both the storage and loss modulus, see Figure 3.24d.

3.2.5.2 Shear moduli as a function of the amplitude of strain

In this Section we focus on the nonlinear viscous, elastic and plastic response of a two-dimensional foam when the applied strain induces a transition between solid-like and liquid-like behaviour. In Section 3.2.5.1 we showed the solid-like behaviour of the foam by applying an oscillatory strain at small amplitude, or rather, below the yield strain. In this section we increase the amplitude of the oscillatory strain beyond the yield strain in order to investigate the nonlinear response of the foam.

Contrarily from the case of small strain amplitudes, when the shear stress can be approximated as a sinusoidal function, for larger strain amplitudes a strong strain hardening is observed at each strain cycle, which leads to non-negligible non-linearity in the stress. The transition from the linear to the nonlinear response is due to the plastic events, which, as we

explained previously, in foams are the strain-induced irreversible bubble rearrangements.

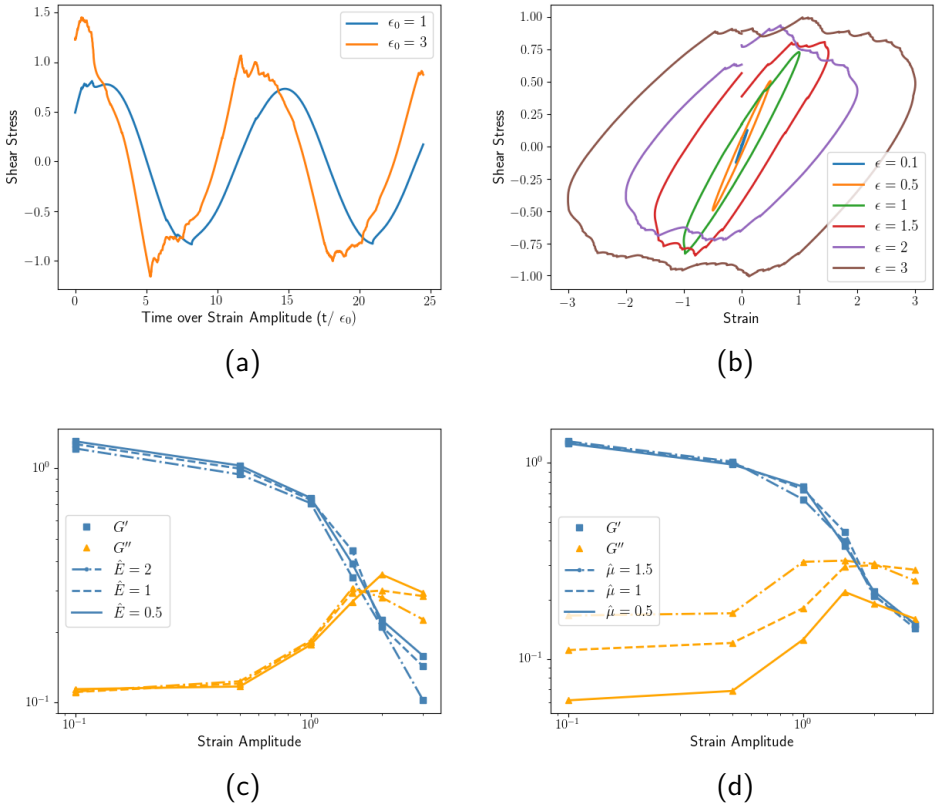

FIGURE 3.25: a) Normalized shear stress versus time. The frequency of oscillation is unitary, while the amplitude of the maximum strain is varied. The elastic and drag parameters are $\hat{E} = 1$ and $\hat{\mu} = 1$ relatively. b) Hysteresis cycles for different strain amplitudes. c) d) Shear moduli against amplitude, calculated varying the two parameters, $\hat{E}$ and $\hat{\mu}$. b) c) and d) are related to the second period of oscillation.

Hence, we keep the frequency fixed without loss of generality and we consider the Fourier decomposition of the stress response [53], in order

to calculate the shear modulus:

$$\sigma(t) = \varepsilon_0 \sum_{n=1}^{\infty} [G'_n \sin(n\omega t) + G''_n \cos(n\omega t)]. \tag{3.12}$$

In complex notation storage and loss moduli are defined as the in-phase and out-phase part of the response, or rather the first term of the Fourier series [52]. Particularly, we consider the following definitions of the storage and loss moduli G' and G'' for each harmonic n:

$$G'_n = \frac{2}{\varepsilon_0} \int_0^T \sigma(t) \sin(n\omega t) dt \tag{3.13}$$

$$G''_n = \frac{2}{\varepsilon_0} \int_0^T \sigma(t) \cos(n\omega t) dt \tag{3.14}$$

where T is the period of oscillation. We only take into account the first harmonic, when $n = 1$.

We apply a periodic oscillatory shear, and in Figure 3.25a we plot the normalized shear stress against time, when the frequency of oscillation is one and the maximum amplitude of strain, ε_0, is varied. We report only the stresses related to the second period of oscillation against the strain, considering the variation of the maximum strain amplitude, ε_0, between 0.1 and 3. The increment of ε_0 above the yield strain leads to the transition of the hysteresis cycle shape from an ellipse to a parallelogram, in agreement with theoretical and experimental results [53, 64]. This tells us that the dissipation in the foam has no longer only a viscous origin but also a plastic one.

In Figures 3.25c and 3.25d we report the shear moduli, which are calculated through Equations 3.13 and 3.14, versus the strain amplitude in logarithmic axes. As expected, we find the storage and loss moduli are roughly constant for small amplitudes and present a cross-over at high amplitude where both the storage and the loss moduli decrease. In Figure 3.25c we explore the effect of the elastic parameter, setting $\hat{\mu} = 1$ and varying $\hat{E}$. We find that the storage modulus slightly decreases for higher $\hat{E}$, while the effect on the loss modulus is not well defined. Vice versa, in Figure 3.25d we set $\hat{E} = 1$ and we find that, this time, the curves of the storage modulus overlap, while the loss modulus clearly increases with the drag of the surfactant molecules, $\hat{\mu}$.

3.3 Remarks

In this Chapter we describe our results when the VF+ST model is applied to simulate a flowing two-dimensional dry foam. After the equilibration of the foam a simple shear strain or an oscillating strain is applied to the foam. The aim is to study the response of the foam in terms of stress and to calculate the rheological parameters of the foam.

We report our results for two foams with different sizes and different polydispersity level. When the strain is applied to a smaller foam, it undergoes a quicker and broader deformation, as a consequence the foam exhibits a shear stress with higher level of fluctuations. We therefore decided to analyse a foam of bigger size which presents a smoother stress-strain curve.

The two-dimensional foam is simulated considering full periodic boundary condition in order to generalize the problem and to exclude singularities due to the contact of the foam with a solid wall. Moreover, we implement the displacement of mass across the vertices and, as we discuss in Section 3.1.2.1, in case of full PBCs our models for the transport of mass across the vertices can be applied to all the vertices without the necessity to implement additional particular cases.

The simple VF model, which is used to simulate dry two-dimensional foams, assumes the surface tension to be constant. In contrast, in the present work we extend the VF with a surfactant transport model and as a consequence we consider the variation of the surface tension. The first question to address is therefore how the variation of surface tension affects the stress response of the foam. We compare the stress-strain curves calculated when the surface tension is constant with the curves obtained varying the surface tension. In particular we consider the different cases obtained varying the elastic and the surfactant drag interafacial parameters. We find that either increasing the elastic parameter or decreasing the surfactant drag leads to a drop in the shear stress drops at higher strains.

Furthermore the stress-strain curves give us qualitative and quantitative information about the foam properties and their dependence on the rate of application of the strain. At small strain we predict the elastic shear modulus G'. We obtain that with smaller surfactant drag the G' becomes rate independent. Similar results are also found increasing the elastic parameter, when considering foams with higher polidispersity.

Starting from the stress-strain curves at high strain we evaluate the yield stress, using the Herschel-Bulkley constitutive equation to fit our numerical results. We find that the yield stress is smaller than the average shear stress, confirming that the foam is behaving as a fluid and the exponent β is less than one, therefore the fluid is shear-thinning. We investigate the influence of the two parameters $\hat{E}$ and $\hat{\mu}$ of our model on the complex fluid behaviour. It results that the increment of the elastic parameter leads to a bigger β while the variation due to the surfactant drag is not clear.

Looking at the topological rearrangements we find a dependence of their distribution on the polydispersity of the foam. In the case of low polydispersity the distribution of T1s does not present a clear order. Vice versa in foams with higher polydispersity, the topological rearrangements mainly happen in correspondence of the elongated bubbles.

Overall through the analysis of the foam subjected to shear strain, we demonstrate how our model can be used as a tool to predict characteristic rheological parameters such as the elastic shear modulus and the yield stress. Concerning the effect of the elastic and the surfactant drag parameters we conclude that it is weaker for monodisperse foams.

Finally we propose our model to predict the shear modulus. The storage and loss moduli can be calculated as a function of the frequency of application of the strain or the amplitude of the applied strain.

In terms of frequency, we show that is possible to predict the shear modulus starting from either the step strain or oscillating strain experimental

data. In both cases we find that the smaller interfacial elasticity leads to higher drop in the loss moduli at higher frequencies. In terms of surfactant drag we observe that decreasing the surfactant drag delays the loss moduli. Varying the amplitude of the applied strain instead leads to plastic irreversible deformations. The elasticity at the interface does not affect the shear modulus while the decrement of the surfactant drag leads to lower energy loss.

Chapter 4

VF+ST application to biological tissues

The morphogenesis of biological tissues is driven by several processes and it is essential for embryo and organ formation in plants and animals. Each cell exhibits a mechanical response to biochemical signals, contributing to the tissue remodelling and organism shaping. The cell mechanics explains how intracellular and extracellular forces control the cell structure. A further understanding of mechanics of cell shape is crucial to extend our knowledges of morphogenesis [50].

In this Chapter we apply our VF+ST model to simulate the forces in a biological tissue. We investigate if the VF+ST model might be a better tool than the simple vertex model, which is usually applied, to simulate biological tissues [29]. In particular, we want to know if the relaxation

that occurs in the tissue is rapid enough for ST effects to be significant and if curvature of cell walls, and therefore the VF effects need to be considered.

4.1 Analogies between fluids and tissues

Biological tissues present not only a robust architecture which ensures stability and resistance to stresses but also significant plasticity which allows active rearrangements of cell junctions. The interplay between robustness and plasticity relies on cell mechanics and allows the tissue to attain homeostasis, or rather its condition of mechanical equilibrium. The variation of the homeostasis condition has been proved to be an important step during morphogenesis and tissue renewal [35]. Thus, enhancing numerical and analytical tools to characterize biological tissues might lead to important predictions and medical innovations.

Among the many intracellular forces, adhesion plays a central role for the formation and stabilization of epithelial layers. Specifically, intracellular adhesion controls cell sorting and an analogy between fluids and tissues can be considered in order to model it [50]. In particular, it is possible to introduce the concept of surface tension in relation to the control of cell shape. During the development of a biological tissue, groups of cells evolve in a succession of equilibrium states driven by the physical cell properties and the physical constraints acting on the cells. A tissue deforms elastically when a deformation is applied on a short time-scale. On the other hand, in the case of slow deformations the elastic response

of cells can be neglected and the cell can be approximated as a viscous fluid whose equilibrium shape is due to the action of surface tension [35].

Figure 4.1 a) shows how in the bulk of a liquid, molecules are subjected to cohesive forces from the surrounding molecules. Conversely, at the surface the interactions between molecules are no longer equilibrated and surface-tension forces arise. The resultant of these forces tend to bring the molecules on the surface back to the bulk, tensing the surface. Thanks to this process a drop of water exhibits a spherical shape minimizing both its surface area and the contact area with the surroundings. The increase of surface area requires an energy which is proportional to the area increment through a coefficient, called surface tension.

Similarly, in the case of tissues, cells separate from each other into two immiscible populations as a consequence of different adhesive properties, as Figure 4.1 b) shows. In general, cells aggregate according to the level of adhesive molecules, known as cadherins, at their surface, see Figure 4.1 d). A cell with fewer cadherin molecules presents less favourable interactions with similar cells and it moves at the interface of contact with a different cell population, Figure 4.1 c). The sorting behaviour due to the different level of cadherins results in tissue surface tension.

Ultimately, it is possible to claim with approximation that cells in tissues behave like molecules in fluids [50]. Thus, cells aggregate in clusters minimizing the surface area; moreover, different cell populations sort themselves in two phases like immiscible fluids [50]. Similarly to fluids it is possible to define a tissue surface tension to study phenomena of

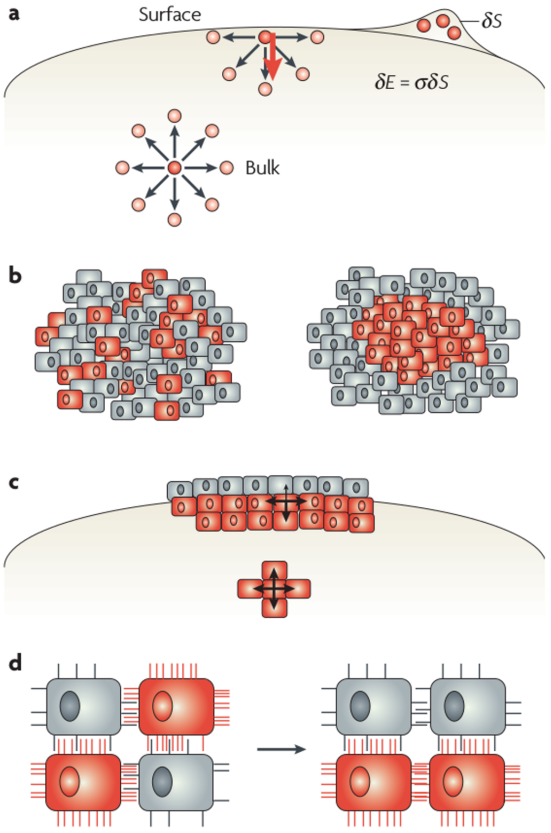

FIGURE 4.1: (From [50]) a) Explanation of the surface tension in a liquid, at a molecular level. Surface tension σ relates the energetic cost δE related to the change of the liquid surface area δS. b) Cells aggregate according to the level of cadherins at their surface, which leads cell sorting. c) A red cell in the tissue has more favourable interactions with similar cells than a red cell at the interface. This results in tissue surface tension. d) The different level of cadherins which is expressed at the cell surface leads to the sorting behaviour of the cells.

aggregation and sorting of cells. In light of this we apply our VF+ST model to simulate a biological tissue.

4.2 Laser ablation on drosophila

Measurements of *in situ* forces and stresses are shown to be important to delineate the role of mechanics in tissue morphology [69]. Genetic information is translated via biochemical signals which regulate cell activities such as proliferation, migration and differentiation. Moreover, cells exhibit mechanical forces and stresses that are able to pull and push on their neighbours to ultimately deform the tissue. The level of stiffness, for example, affects the cell differentiation, especially in bones, muscles or blood vessels. Achieving a comprehensive picture of tissue and organ development will have a significant impact on studies of tissue homeostasis, regeneration and disease.

In the last decades, image acquisition tools to record dynamic changes in cells and tissue shapes have been considerably developed [36]. An increasing number of methods are performed and described in the literature to measure forces and stresses in cell cultures. Here we consider the laser ablation technique which allows to study tissue mechanics *in vivo*, especially during development [69].

In sub-cellular laser ablation, a laser is focused on a particular cell structure to disrupt the cell-cell junctions. Severing the structure causes the displacement of the ablated junctions which move apart, pulled by the

tension of adjacent junctions. The analysis of the rate of displacement is used to calculate the cell-cell junction tension which existed before the ablation. The calculation doesn't account for the viscous drag effects due to the geometry and the viscosity of the cells interfaces, which also affect the dynamics of cell-cell junctions.

Cell-scale laser ablation experiments revealed that the contractile tension at the cell junction drives cell intercalation and elongation [29, 62]. Moving to the tissue-scale, laser ablation can be used to ablate a line of cells generating a wound [1, 39], then it is possible to analyse the rate of the healing in order to measure the stress-to-viscosity ratio within the tissue. Alternatively, annular ablations [6, 28] reveal the anisotropy of the stress and its principal directions [69].

In the present work we address the experimental measurements published by Bonnet *et al.* [6]. They investigated the dorsal thorax epithelium of *Drosophila* pupa. The pupa is the middle life stage of the fly which metamorphoses from a larva to an adult, Figure 4.2 a) represents the three life stages. The dorsal thorax is a single layer of cells, composed by a large anterior region, called the scutum, and a posterior tip, the scutellum. During the metamorphosis the scutellum undergoes extensive morphogenesis and it therefore constitutes a useful model to investigate the mechanics of morphogenesis during tissue development [6, 7]. Figure 4.2 b) represents the tissue from the scutellum of a *Drosophila* pupa. The tissue exhibits symmetry across the axis drawn in Figures 4.2 a) and b) by the dashed line. Bonnet *et al.* [6] carried out the laser ablation to sever the cell-cell junctions in the annular region between the blue

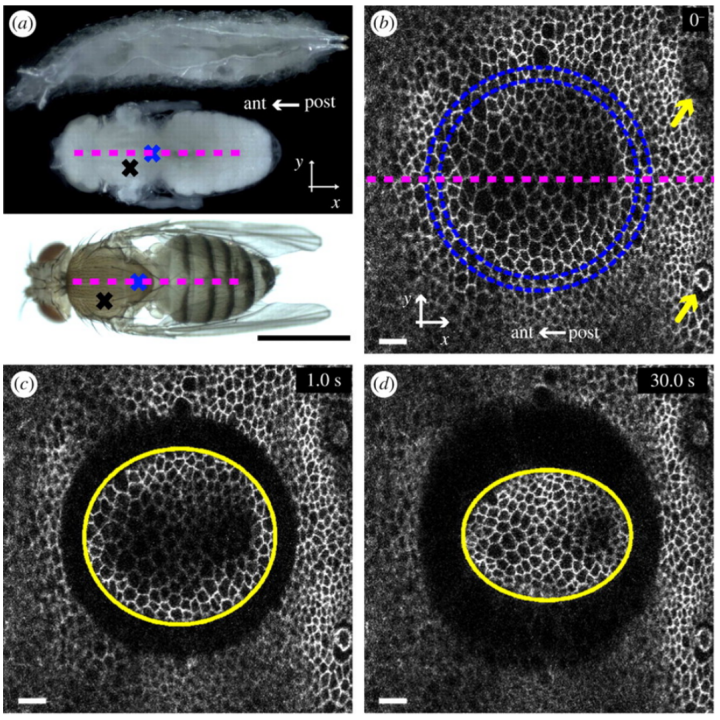

FIGURE 4.2: (From [6]) Annular ablation in a *Drosophila melanogaster* dorsal thorax. a) Developmental stages of the fruitfly. Top: larva. Middle: pupa. Bottom: adult. The dashed line represents the symmetry axis while the blue cross is the position of the cutting. b) Epithelial before cutting for a *Drosophila* pupa. The blue circles define the annular severed region, the distance between the concentric circles is approximately one cell size and the circular area contains 100 cells. The yellow arrows indicate the reference points to locate the severed area. c) 1 second after the ablation, the fitted ellipse is plotted in yellow. d) 30 seconds after the ablation.

concentric circles in Figure 4.2 b), generating a circular tissue domain of about a hundred cells, as shown in Figure 4.2 c). After waiting for the mechanical relaxation of the tissue they found that both the inner and outer wound margins exhibit similar rate of displacement and anisotropy. Moreover, they noticed that the outer ellipse boundary presents minor and major axes orthogonal to the minor and major axes of the inner ellipse, as shown in Figure 4.2 d). They repeated the experiment at three different ages of the pupa, they fitted the retracting domains by an ellipse and calculated the ellipse semi-axes as a function of time. The laser ablation technique allows the ablation of several cell-cell junctions at once leading to a direct measurement of the components of the stress-to-viscosity ratio tensor. Furthermore, by isolating the epithelium domain they set well-defined conditions to analyse the tissue through a continuous model. They indeed conclude that the epithelial domain can be described as a continuous, linear, visco-elastic material. In the present Chapter we apply our VF+ST model to reproduce the same experiment, as discussed below.

4.3 VF+ST model versus vertex model

Thanks to the analogies between fluids and tissues, foam models are often used to study biological tissues, particularly the vertex model and the Potts model, introduced in Chapter 1. Farhadifar *et al.* [29], for example, developed a vertex model to study the physical basis of epithelial cell packing in the larval wing disc of *Drosophila*. In their model, cells are

described as polygons with cell edges defined as straight lines connecting vertices. Much is known about the epithelial layer, which contains many proteins with both adhesive and contractive functions. Farhadifar *et al.* [29] therefore developed a physical description of the tissue which takes into account cell elasticity and junctional forces arising from cortical contractility and adhesion.

The model presented by Farhadifar *et al.*, considers the interface elasticity, the line tension at junctions between individual cells and the contractility of the cell perimeter. The network of vertices obeys a force balance, or rather the net force acting on each vertex vanishes. All the forces considered can be represented by an energy function, which is similar to the energy functions used in previous works [32, 38], and any stable and stationary configuration of the network of vertices corresponds to a local minimum of the energy function. Moreover, the cell volume is assumed to be constant and while the single cell is described as an elastic object the whole network takes into account junction remodelling and it is therefore considered as a elasto-plastic material. Furthermore, Farhadifar *et al.* carried out a laser ablation on the tissue of the *Drosophila* wing disc. Through comparison of experiment and theory they identify a range of parameters which allows the vertex model to account for the observed vertex movements induced by the laser ablation.

Similarly to the vertex models dedicated to the study of foam, the model described above neglects the curvature of the cell walls. In the present Chapter we present the results given by our model where the curvature of the cell wall and the related friction effect are considered. The aim

is investigate how the pressure inside the cells and the friction effects influence the morphology of the tissue.

4.4 Results

4.4.1 VF+ST to simulate Drosophila tissue

We decide to use the VF+ST model to reproduce the experiments published by Bonnet *et al.* [6], who investigated the dorsal thorax epithelium of *Drosophila* pupa when an annular laser ablation is applied. The question that we want to address is if the additional elastic and viscous effect introduced with our model affect the tissue anisotropy, which has been observed through the experiments.

As a first step we relax the tissue to reproduce the condition of initial mechanical equilibrium of the tissue. We define an annular region considering the position of the centre of cells, in particular the region has the thickness of two cells. Then we instantaneously remove the cell-cell junctions in the annular region (see Appendix A.5) and let the tissue relax again towards mechanical equilibrium.

In order to simulate the ageing of the pupa, we apply a pre-strain p_s to the tissue along the x-axis. The pre-strain applied is an extensional shear in order to conserve the total area, thus the total length along the x-axis is $x' = x(1 + p_s)$ and analogously the total length on the y-axis is $y' = y/(1 + p_s)$. The aim is to reproduce the stretch that the tissue

undergoes during its development. We assume that the tissue extension during the pupa ageing is not wider than the 30% of the initial tissue size. Thus, we pre-strain the tissue of 7%, 15%, 22% and 30% of the initial tissue width, to simulate different stages of the pupa evolution.

In Figure 4.3 we show the four steps: the initial relaxation of the tissue, the application of the pre-strain and further relaxation, the annular ablation and the final relaxation of the tissue after the ablation is applied.

Figure 4.4 shows the final configuration of the tissue after the ablation and the relaxation are carried out, when no pre-strain is applied. We mark the three-fold vertices on the boundaries of the ablated area, and these points are then used to fit the ellipses for both the internal and the external margins of the annular area. We plot the external ellipse with a dashed line in Figure 4.4 .

In Figures 4.5a and 4.5b we plot the configuration we obtain with a pre-strain of 15% and 30% respectively.

We again plot the centres of the cells at the wound margins and the fitted ellipses. In agreement with experimental results we find that the eccentricity of the ellipses increases with the pre-strain applied, or rather the age of the pupa. In Figure 4.6 we plot the eccentricity of the internal and external ellipses versus the applied pre-strain. The external ellipse exhibits major and minor axes approximately orthogonal to the major and minor axes of the internal ellipse, in agreement with the experimental results, see Figure 4.2 d). This results confirms the viscoelastic nature

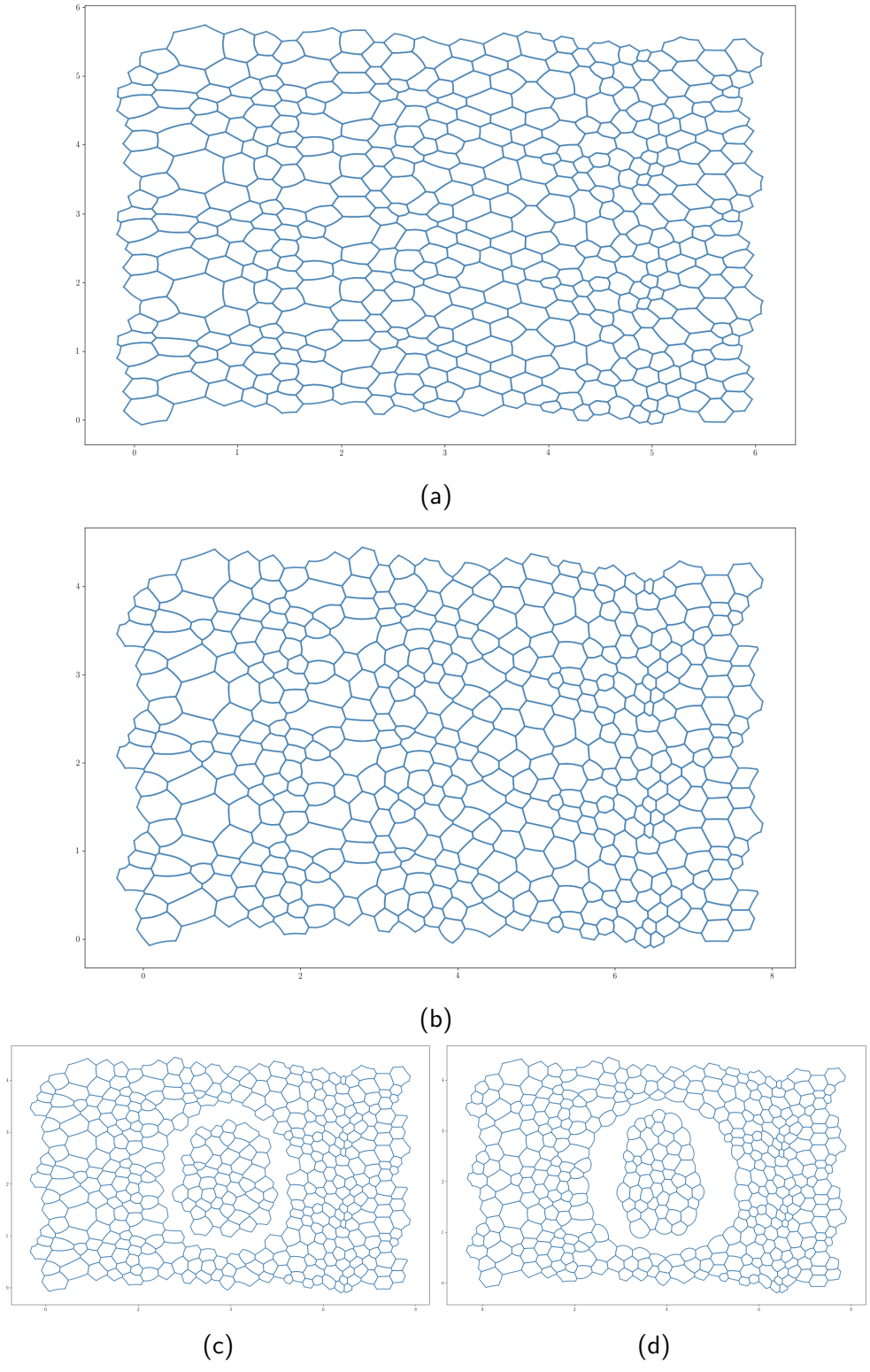

FIGURE 4.3: a) Initial tissue relaxation. b) Tissue after application of a pre-strain of 30 % and further relaxation. c) Ablation of an annular region. d) Relaxation of the tissue after the ablation.

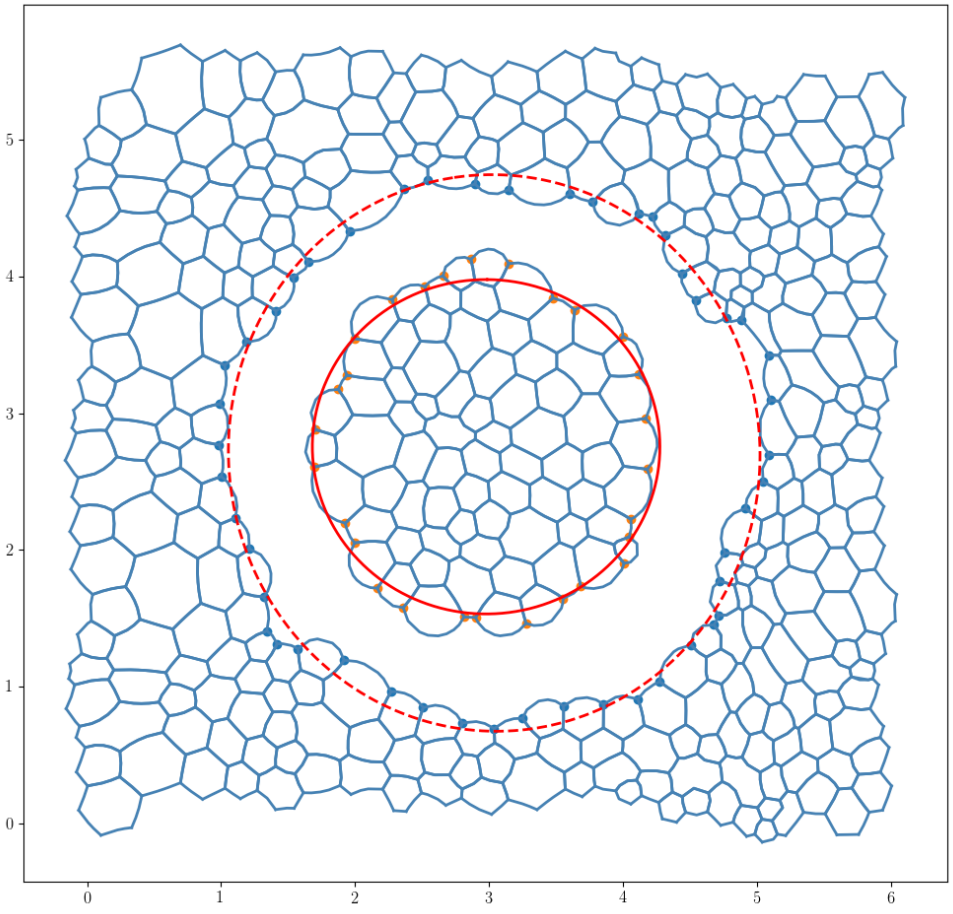

FIGURE 4.4: Tissue configuration after severing of cell-cell junctions in an annular region. The ellipses which fit the threefold vertices (orange and blue dots) of the cells at the boundaries are plotted, with continuous and dashed lines for the internal and external ellipse respectively.

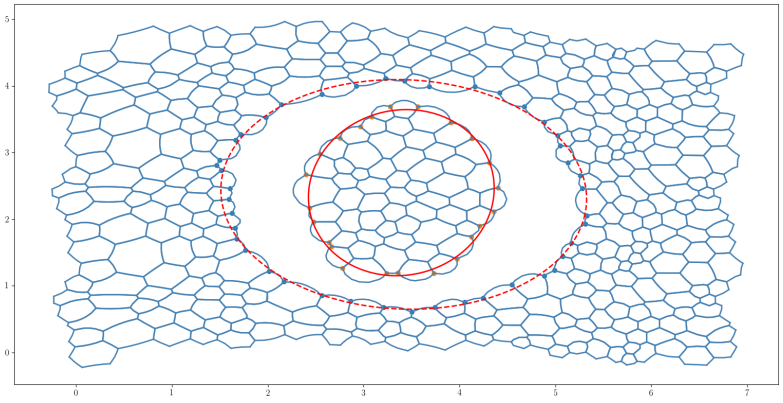

(a)

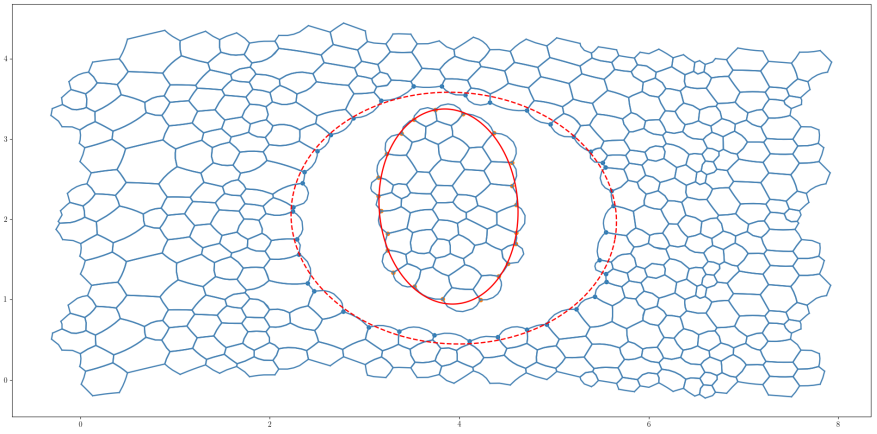

(b)

FIGURE 4.5: In order to simulate the pupa ageing, a pre-strain of 15% and 30% of the initial width is applied to the tissue, in a) and b) respectively. After cutting cell-cell junctions in an annular region, the tissue is relaxed until the condition of mechanical equilibrium. The vertices of the cells at the boundary are plotted and fitted through ellipses. We plot the internal and external ellipses with continuous and dashed lines respectively.

of the tissue and, broadly speaking, the appropriateness of our model to describe it.

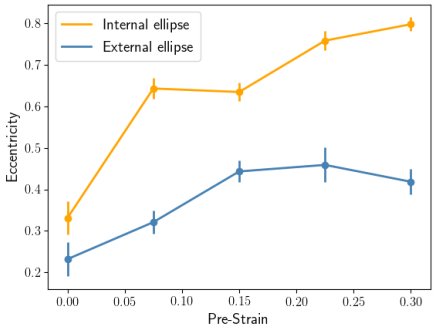

FIGURE 4.6: Eccentricity of the internal and external ellipses versus the applied pre-strain with the related error bars.

In order to show the evolution of the ellipses in time during the relaxation after ablation, we report the maximum and minimum axis lengths of the internal and external ellipses in Figures 4.7a and 4.7b. All the values are re-scaled with the lengths of the related axis at time zero. Particularly, we report the minimum and the maximum axis lengths versus time for the applied pre-strain of 0, 15% or 30%. After the ablation both the internal and the external ellipses evolve towards a final steady state configuration. The jumps in the curves, in Figures 4.7a and 4.7b, correspond to the topological rearrangements happening at the boundary of the ablated area.

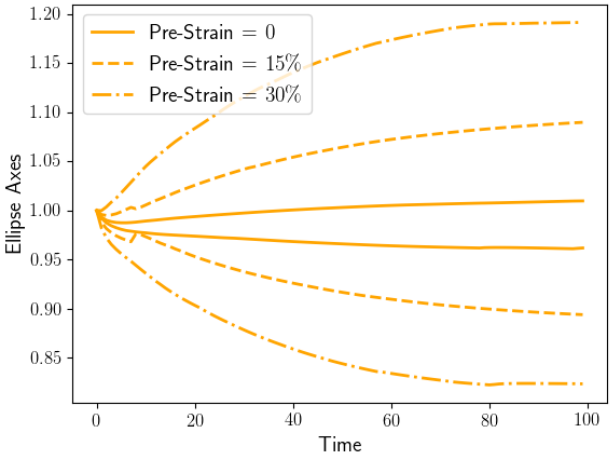

(a)

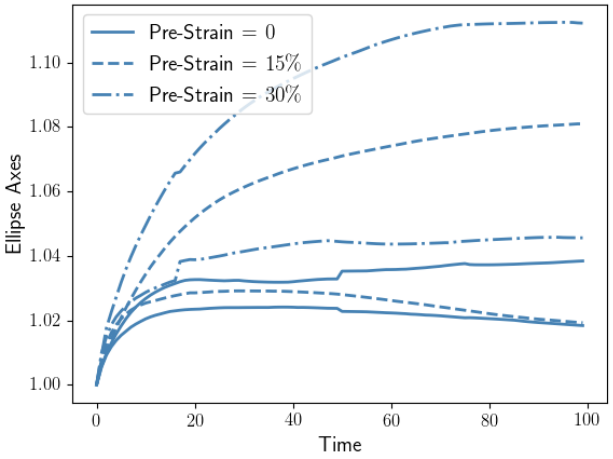

(b)

FIGURE 4.7: We report the maximum and minimum axis lengths of the ellipses versus time, all the values are re-scaled with the lengths of the related axes at time zero. Particularly, we plot in a) the axes of the internal ellipse and in b) the axes of the external ellipse. Both panels contain the results for the tissues with a pre-strain of 0, 15% or 30%, which are plotted in Figures 4.4, 4.5a and 4.5b respectively.

4.4.2 How $\hat{E}$ and $\hat{\mu}$ affect the anisotropy

As we did in the previous Chapter, here we aim to investigate how the free parameters of our model, that is the elasticity of the cells walls and the drag on the cell walls, affect the dynamics of the tissue. Moreover, we look at the distribution of the anisotropy of the tissue structure after cutting of the cell-cell junctions in the annular area. The results presented in Section 4.4.1 were calculated using the parameters $\hat{E} = 1$ and $\hat{\mu} = 1$. In this section we present the results obtained running the simulations for different values of $\hat{E}$ and $\hat{\mu}$.

In Figure 4.8 we report the eccentricity of the ellipses fitted at the boundary of the ablated area, after the equilibrium configuration of the tissue is reached. The elastic parameter $\hat{E}$ takes the values 0.1, 0.5, 1 and 2, while $\hat{\mu} = 1$. We see that the two parameters $\hat{E}$ and $\hat{\mu}$ have little effect on the final structure.

In Figure 4.9 we report the variation in time of the axes of the internal and external ellipses after the ablation of the annular region is applied. This time we fix the pre-strain and we plot the variation of the axes due to the different elasticity at the interface of the cell-cell junctions. We therefore set $\hat{\mu} = 1$ and we assign the values 0.1, 1 and 2 to $\hat{E}$. In Figure 4.9a and 4.9b we show the results for the ellipses when no pre-strain is applied to the tissue. We observe that the eccentricity of the ellipses is slightly more pronounced when the tissue has smaller elasticity.

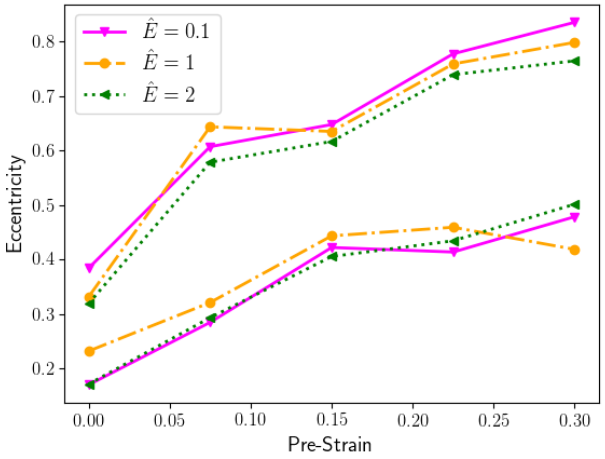

(a)

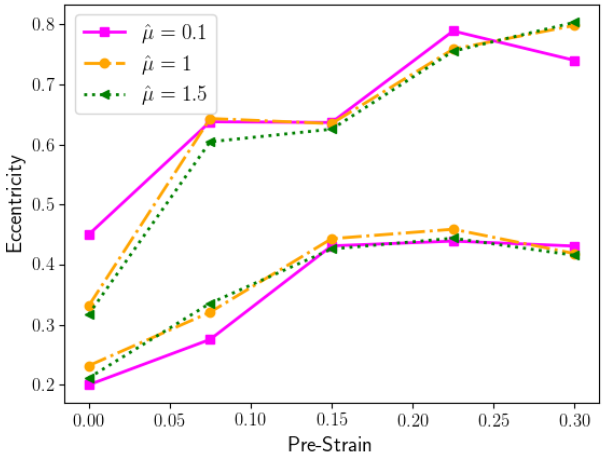

(b)

FIGURE 4.8: Eccentricity of ellipses fitted at the boundary of the ablated area, after the mechanical equilibrium configuration of the tissue is reached. a) refers to the internal and external ellipses relatively, when $\hat{\mu} = 1$ while the values 0.1, 1 and 2 are taken for $\hat{E}$. Vice versa b) refers to the internal and external ellipses, when the parameter $\hat{E} = 1$ while the values 0.1, 1 and 1.5 are taken for $\hat{\mu}$.

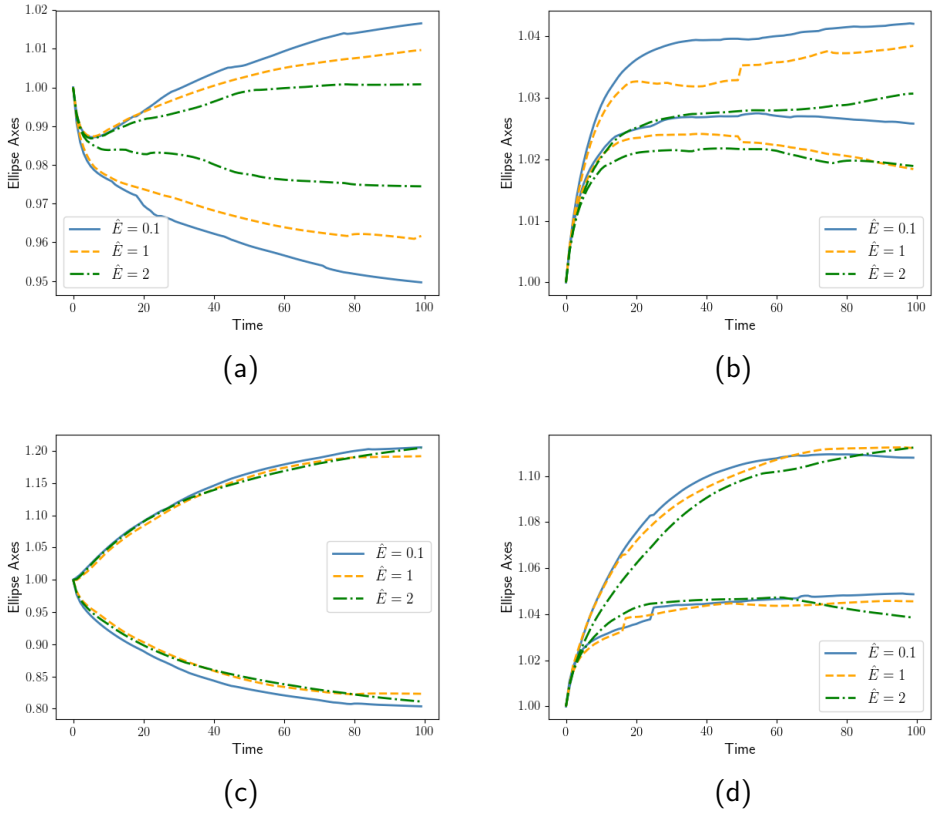

FIGURE 4.9: We report the maximum and minimum axis lengths of the ellipses versus time, all the values are re-scaled with the lengths of the related axes at time zero. $\hat{\mu} = 1$ while the values 0.1, 1 and 2 are taken for $\hat{E}$. a) and b) show the axes of the internal and external ellipses when the pre-strain is zero, while c) and d) show the results obtained when the pre-strain is 30%

Diversely in 4.9c and 4.9d we plot the results obtained for the tissue with a pre-strain of 30%. In this second case the variation of elasticity does not affect the evolution of the axes lengths.

From Chapter 3 we have the idea that, in case of foams, bubble disorder is important and an isotropic foam can accommodate local variations in tension without affecting global response. In Chapter 2, where we examine the dynamics at the film scale, we see that this is not the case. Here we find that over a very small distance, most of the dynamics are a slow relaxation to equilibration (Figure 4.7) and so $\hat{E}$ and $\hat{\mu}$ are probably only important at early times.

4.5 Remarks

After developing the VF+ST model we address the question of testing the suitability of the model to simulate a biological tissue.

The choice of a foam model to study a biological tissue can be justified by accounting for the analogies between fluids and biological tissues. We decide to reproduce specifically the experiments published by Bonnet *et al.* concerning the dorsal thorax epithelium of *Drosophila* pupa [6]. The set-up of their experiments is clearly presented and we decided that reproducing these experiments could be a straightforward way to test the appropriateness of our model to investigate biological tissues.

After the ablation of cell-cell junctions within an annular region of a pre-strained tissue, the relaxation of the tissue towards the configuration of

mechanical equilibrium stimulates the transition of the ablated area from a circular to an elliptical shape. We successively fit the boundaries of the ablated areas with ellipses and calculate the eccentricity of the ellipses to quantify the initial structural anisotropy in the tissue.

In agreement with the experimental results we find that the anisotropy of the tissue, or rather the eccentricity of the ellipses, increases with the age (pre-strain) of the pupa. Furthermore, our model catches the viscoelastic behaviour of the tissue since it shows that the outer ellipse becomes stretched in a direction approximately orthogonal to the inner ellipse.

The surfactant level parameters of the VF+ST model have little effect on the final state of the tissue, so it is difficult to decide on the suitability of our model to answer biological questions.

Overall although the similarity between foams and tissues which we mentioned earlier, there are also significant differences, which perhaps should be taken into account. The main one is that in a tissue the molecules which determine the contractile and adhesive tensions are not only localized in the cell-cell junction but also in the rest of the cell. The presence of such molecules causes fluctuations that are not considered in our model. Considering these additional components might be a future step for the present work.

Chapter 5

Conclusion

In this thesis we built a numerical model to simulate the dynamics of two-dimensional dry foams.

In the first Chapter we explained our motivations, describing possible foam applications from oil recovery to varicose veins treatments. We offered an overview of the well known fundamental laws for foam physics and of a few rheological key concepts. Furthermore, we briefly described some of the existing models, which have been developed to simulate and investigate foam behaviour. Even if those models are able to capture several foam properties, none of them can completely predict all phenomena which affect foam dynamics. In this thesis we presented our new contribution to the foam state of art.

There are some applications, for example micro-fluidic foams, in which the foam flows at high velocities and the variation of surface tension and

the related dissipation effects can not be neglected. In the present work we decided to consider the dissipations due to the displacement of surfactant molecules along the films. We therefore relaxed the assumption of constant surface tension which is suitable for quasi-static models.

We developed an extension of the Viscous Froth model introducing the variation of the surface tension along the films in order to consider the drag related to the surfactant molecules in the thin layer at the film interface. As a first step we simulated a system of five films which is shown in Figure 2.1. In particular we analysed the topological rearrangement of the five films: after triggering the T1 we tracked the evolution of the lengths of the newly created central film and the shrinking lateral films. Despite its simplicity the five films system allows us to investigate the variation of film lengths and the molecules distribution as the system evolves towards the final equilibrium configuration.

To ensure the conservation of mass we assumed that the molecules in the shortest film before the T1 are instantaneously moved to the newly created film. Moreover, starting from uniform distribution of molecules (Γ_{eq}) in order to allow the relaxation of the films towards the final equilibrium we implement a displacement of molecules across the vertices.

Using a simple device, experiments to track the lengths of the films after a T1 were carried out for two different foaming solution with different viscosity. We then applied our numerical model to fit the experimental data and to predict physical parameters for the two considered solutions. We found that the additional dissipation effects introduced in our model

are crucial to describe the evolution of the films in the case of solutions with higher viscosity.

The same experiment that we used to study the evolution of the film lengths after a T1 could be also applied to analyse the thickness of the evolving films, and carry out further studies about drainage which was neglected in the present work.

Studying the five films system was a very useful stating point to refine our model. Moreover we defined the two free parameters related to the Gibbs elasticity and the surfactant transport at the interface of the film and we analysed their effect on the film's evolution. We learned that films with either higher viscosity or higher elasticity present a slower evolution towards the final configuration of equilibrium. Furthermore, as a consequence of the Langmuir Eq. (2.1), films with higher elasticity exhibit a lower surface tension at equilibrium.

After applying our VF+ST model to investigate the foam at a surfactant level we moved to the bubble scale. We analysed a more complex system, that is a quasi-two-dimensional foam.

We implemented dedicated libraries in Python to build the foam and to simulate its flow. In particular we developed dictionaries where we store all the necessary informations about the films, the vertices, the pressure and the adjacency between neighbouring cells. We decided to consider full periodic boundary conditions to keep the analysis general and avoid the particular cases due to the interaction between the foam and solid walls.

We proposed our model as a tool to predict rheological parameters for a foam. We applied a simple shear to a foam to calculate the stress-strain curve which gives us important information about a foam's behaviour. At small strain, where a foam behaves like an elastic solid, the curve allows the calculation of the elastic shear modulus. While in correspondence of higher strains the curve shows the expected transition of the foam to a fluid-like material behaviour and it leads to the estimation of the yield stress. Concerning the effect of the elastic and the surfactant drag parameters we noticed that the isotropy of the structure inhibits their effect on the foam.

As known from the theory, a complex fluid requires several strain-rate dependent parameters to be characterized, including the shear modulus. We decided therefore to apply our model to predict it.

From an experimental point of view it is possible to apply an oscillating strain or a step strain to the foam. We apply our model to simulate both cases, we calculate the stress response of the foam and we predict the shear modulus.

In the case of an oscillating strain, it is possible to fix the amplitude of the strain and vary the frequency of oscillation or vice versa. In the latter case plastic deformation will be induced. Alternatively, an easier experiment can be carried out by applying a step strain. In this case the Fourier transform allows to convert the experimental results from the time to the frequency domain in order to estimate the shear modulus.

We wanted to know how the characteristic parameters of our model related to the elasticity and the surfactant drag at the film interface affect

the foam behaviour. We found that smaller elasticity correspond to a reduction of both the storage and the loss moduli when the frequency increases. On the other hand, reducing the surfactant drag coefficient leads to the shift of the storage and loss moduli. Finally, considering the variation of the amplitude of the applied strain we noticed no effects related to the variation of the elastic parameter and a drop of loss energy when the surfactant drag is reduced.

After studying the application of our VF+ST model to two-dimensional dry foams we chose to investigate the suitability of the model to answer biological questions. We decided to reproduce experiments for biological tissues. Usually the Vertex model and the Q-Potts model are used to simulate biological tissues, in the present work we investigated if the additional dissipative effects implemented in our model can enhance the simulation of the tissues.

We simulated the evolution of the dorsal thorax epithelium of *Drosophila* pupa after an annular ablation is applied. In order to simulate the ageing of the tissue we applied an uni-axial pre-strain to the tissue then we repeated the simulation at the different pre-strains (ages). We measured the evolution in time of the ablated area which evolves from a circular to an elliptical shape. The eccentricity of the ellipse was used as a measure of the anisotropy of the tissue. Experimental results show that in the final state after the ablation and the relaxation of the tissue to the configuration of mechanical equilibrium, the anisotropy of the structure increases with the age of the *Drosophila* pupa. The results from our simulation agreed with the experimental data, confirming that our model is able

to reproduce the visco-elastic behaviour of the tissue. Nevertheless, the variation of our model parameters, related to elasticity and surfactant drag, seemed to have an influence only at short times during the first stage of tissue relaxation after the ablation. Moreover, this influence decreases when higher pre-strain is applied.

Our model, which has been developed for foams, involves the elastic and frictional properties at the interface of the films. Differently in tissues the molecules involved in tensile, contractile and adhesive interactions are not exclusively localized at the cell-cell interface but also in the rest of the cell. As a possible next evolution of the model it would be interesting to include the fluctuations which are induced by the concentration of molecules in the cell body on the cell-cell interactions.

Appendix A

Implementation of the numerical model

A.1 Data structure

In order to create the initial configuration of the foam, we generate a random array of points and then we apply the library *pyvoro* to calculate a starting dictionary in which to store the information that we need. One dictionary is generated for each bubble. In particular the dictionary contains arrays with the coordinates of both the vertices and the centre of the bubble and its area. Moreover, we store information about the neighbours, hence we need to know the adjacent bubble for each film. The latter information is used to calculate the pressure difference across each film.

As a second step we fix the critical lengths: we choose a minimum l_{min} and a maximum l_{max} length of segments which ensure the numerical stability of the simulation. Starting from the vertices for each bubble we create the films and their tessellation, inserting or deleting points as necessary. Starting from the segments we can calculate the curvature along the films as $K = \frac{\beta_2 - \beta_1}{(l_1+l_2)/2}$ where β are the angles calculated with respect to the horizontal axes x and l are the lengths of the segments, as shown in Fig.A.1

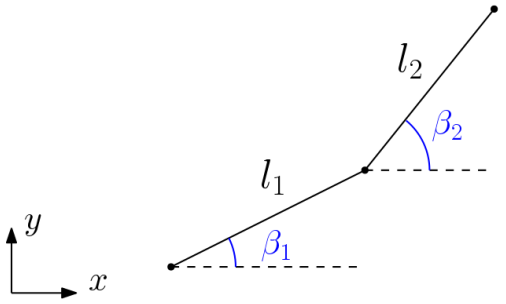

FIGURE A.1: Two segments within a film, we indicate the angles β and the lengths l used to calculate the curvature.

Once we have the tessellation we proceed assigning a number of molecules to each segment and we calculate the surfactant concentration and the tension for each segment. We append the lists of the additional information to the original dictionary for each bubble.

Finally, we apply the ideal gas law to calculate the pressure of each bubble starting from the known areas. For a bubble of area A_b we have $P_b A_b = C_w$ where C_w is a characteristic constant which has to be chosen big enough to keep the area fixed. For the considered foam we choose $C_w =$

50, value which ensure to avoid the shrinking of the bubbles. Increasing further the value of the constant C_w does not damage the simulation neither gives any advantage. Note that the areas of the bubbles undergo an initial variation while the foam evolves from the Voronoi tessellation towards the equilibrated configuration. The bubble areas does not change once the foam has reached its initial equilibrated configuration. Also the pressure information are stored in a dedicated list.

During the relaxation of the foam each film undergoes stretching or shrinking, we need therefore to update most of the information at each step. On the other hand, the information about the neighbour bubbles needs to be updated only after a topological rearrangement.

A.2 Vertex dynamics

The dynamics of vertices requires as a first step to identify the films of different bubbles which meet at the same vertex. We create a function which takes as input the coordinates of all the nodes in the foam and the domain's dimensions and returns a list of arrays, one for each vertex.

Each array contains the coordinates of the first node of the three films merging in the same vertex i and the indices to identify the related bubbles. Because the films in all the bubbles are sorted in anticlockwise we decide to store only information related to the first node within the first segment for each film, as each film is made by more segments which are refined at each iteration. In Figure A.2 we sketch a few bubbles with

the direction of the films indicated. Each edge represents two films from two adjacent bubbles. As a consequence, we can calculate the tessellation and the concentration of surfactant molecules separately for each bubble. Moreover considering only the first segment for each film we avoid the

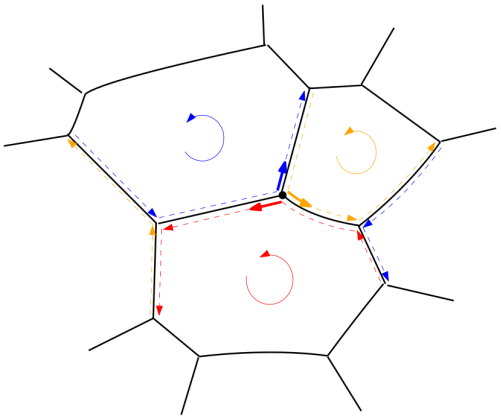

FIGURE A.2: Sketch of a few bubbles. We indicate the anticlockwise direction of the films. Some films are indicated in dashed lines, furthermore, we plot in continuous line the segments which we consider to calculate the dynamics of the vertex.

need to consider overlapped nodes since there are only three films which start from the same vertex. Once we have the list of threefold arrays we apply Eq.(2.4) to calculate the dynamics for each vertex and Eq. (2.5) to implement the displacement of surfactant molecules across each vertex. Unless a topological rearrangement happens we don't need to update the list of arrays at each iteration.

A.3 Periodic Boundary Conditions

Particular attention is necessary for the case of bubbles at the border of the considered domain where we have vertices with two films on one side and the third film on the opposite side of the domain, as shown in Figure A.3.

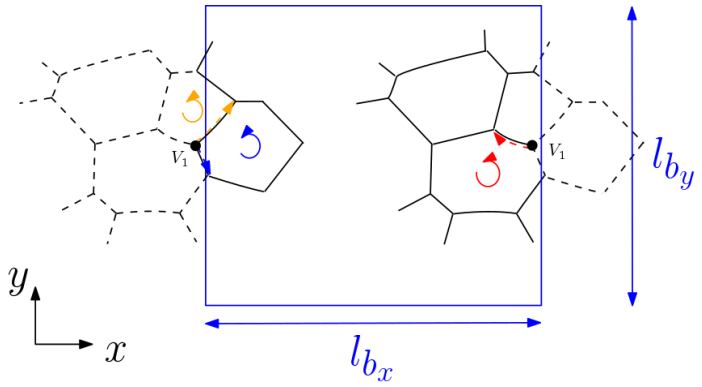

FIGURE A.3: Periodic boundary condition along the x-axis. The blue square is the domain of the foam of size l_{b_x} and l_{b_y}. We indicate on the left side the blue and orange films which merge in the vertex V_1 and on the right side the red film related to the same vertex V_1.

To address the periodicity of the system, together with the indices related to films and cells we store for each vertex two coefficients related to the periodic conditions. The coefficients are $-l_b$, 0 or $+l_b$ depending on whether the node of the film is on the left/right side, within or on the bottom/upper side of the boundaries. l_b is the length of the domain along the x-axis or the y-axis, as shown in Figure A.3. Hence, we store two coefficients for both the x and the y coordinates which are necessary to

implement the full periodic boundary condition. To check the position of the points we use a tolerance of 10^{-4}.

When the periodic coefficient is different than zero we create a copy of the coordinate, we translate it by l_b times -1 or $+1$ depending on the sign of the periodic coefficient. The translated copy of the coordinate is used to calculate the dynamic of the vertex.

The same procedure is also used for segments involved in topological rearrangements which may happen at the borders (see A.4).

An additional condition that needs to be considered is related to the corners, if both the periodic coefficients are different from zero it means that the vertex is located at one corner of the boundaries. In this case we implement an additional translation of the coordinates, in the direction indicated by the periodic coefficient, before storing them in the dedicated list. This also allows the implementation of topological rearrangements which may happen at the corners.

Finally, we implement the variation of the list due to the application of the boundary shear. We apply the shear to the boundaries and we use the strained boundaries as reference to check the position of each vertex and store the new periodic coefficients.

A.4 Topological rearrangement T1

From a numerical point of view the first consideration to implement a T1 is related to the critical length l_{crit} which has to be coherent with the minimum length l_{min} of the tessellation, which we define in Section 2.2. We choose a critical length which is slightly longer than the minimum length l_{min}. Then we need to spot the eventual presence of the films shorter than the critical length. The topological rearrangement will necessarily involve films with a single segment between two vertices. As a consequence to spot the films with critical length, instead of checking all the segments of the foam, we only iterate through the list of threefold arrays that we use for the vertex dynamics. Successively, we store the indices related to the films and the relative bubbles with critical lengths. We use the list of neighbours to spot the two bubbles and the vertices in which we need to insert the new film after the T1.

We create a new film in a direction perpendicular to the deleted film. We assume that surfactant molecules on the deleted film are instantaneously transferred to the new film. Considering the anticlockwise definition of the films in each bubble, as shown in Figure A.2, we insert the new film in the coherent direction. As mentioned in the previous section A.3, it might happen that the critical films are at the border of the domain, as a consequence we use the periodical coefficients related to the two vertices involved in the topological rearrangement to check the periodic conditions and eventually to translate the new film as necessary.

As a final step we need to update the information of adjacency related to the four bubbles involved in the topological rearrangement, and to delete and add a row coherently with the removed and the introduced film relatively. Moreover, we need to update the threefold arrays to calculate the vertex dynamics, thus all the indices of the four bubbles involved in the T1 and the indices of the surrounding bubbles will be different.

A.5 Ablation cell-cell junction

In Chapter 4 we present our results related to the application of the VF+ST model to simulate biological tissues. In particular we decided to simulate the ablation of edges, which in case of tissue are referred as cell-cell junctions.

From a numerical point of view we had to introduce a new function to ablate the cell-cell junctions. We define an annular region and find the cells within the area considering the centres of the cells, which are plotted in blue in Figure A.4. By means of the list of adjacent cells we deduce which are the cell edges in contact with the ablated area and which edges we need to merge in a single one after cutting the cell-cell junctions. We merge the edges which are connected by red vertices shown in Figure A.4.

In addition to the arrays of coordinates we need to merge also the lists of values related to the lengths of the segments of the tessellation, the information about the surfactant molecules concentration and the surface tension. We need to update the list related to the adjacent cells and the

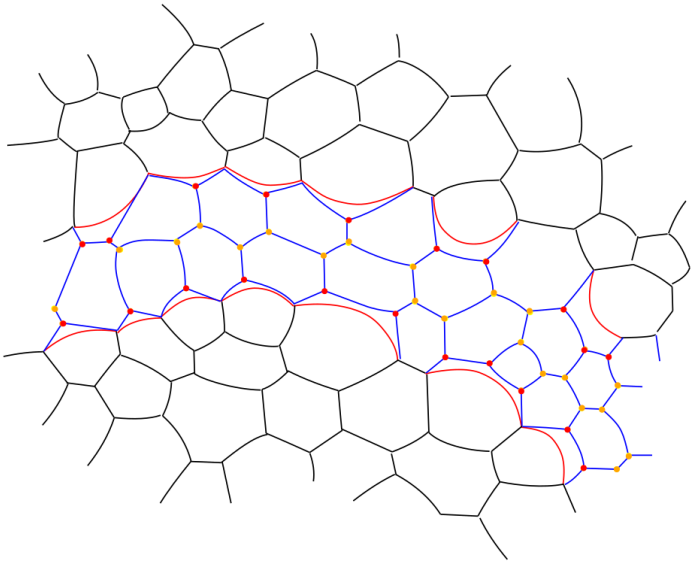

FIGURE A.4: Portion of the simulated tissue. The cells in blue are in the ablated area. The edges connected by the red vertices are merged in single edges, which are plotted in red. The blue cells are deselected from the calculation and both the red and the orange vertices are deleted from the list to estimate the vertex dynamics.

list of threefold arrays for dynamics of vertices, particularly we delete the vertices plotted in red and orange in Figure A.4. After updating all the data we store in a new list the indices of the cells in the ablated area, plotted in blue in Figure A.4, and we deselect them from the further iterations, in this way we don't change the indices in the main dictionary and therefore we don't have to recalculate all the indices.

Finally we need to define the pressure in the ablated area, a value that we need to calculate the pressure drop across all the films in contact with the abated region. We choose as pressure in the ablated region the average of the pressures in the ablated cells.

Bibliography

[1] L. Almeida, P. Bagnerini, A. Habbal, S. Noselli, and F. Serman. A mathematical model for dorsal closure. *Journal of theoretical biology*, 268(1):105–119, 2011.

[2] A. Audebert, S. Beaufils, V. Lechevalier, C. Le Floch-Fouéré, A. Saint-Jalmes, S. J. Cox, F. Zaccagnino, and S. Pezennec. Topological rearrangements and surface rheology: a multi-scale approach to dairy protein foams. *In preparation*, 2018.

[3] C. K. Batchelor and G. Batchelor. *An introduction to fluid dynamics*. Cambridge university press, 1967.

[4] F. Bolton and D. Weaire. Rigidity loss transition in a disordered 2d froth. *Physical review letters*, 65(27):3449, 1990.

[5] F. Bolton and D. Weaire. The effects of Plateau borders in the two-dimensional soap froth. ii. general simulations and analysis of rigidity loss transition. *Phil. Mag.*, 65(1):473–487, 1992.

[6] I. Bonnet, P. Marcq, F. Bosveld, L. Fetler, Y. Bellaïche, and F. Graner. Mechanical state, material properties and continuous description of an epithelial tissue. *Journal of The Royal Society Interface*, 9(75):2614–2623, 2012.

[7] F. Bosveld, I. Bonnet, B. Guirao, S. Tlili, Z. Wang, A. Petitalot, R. Marchand, P.-L. Bardet, P. Marcq, F. Graner, and Y. Bellaïche.

Mechanical control of morphogenesis by fat/dachsous/four-jointed planar cell polarity pathway. *Science*, 336(6082):724–727, 2012.

[8] F. Bosveld, B. Guirao, Z. Wang, M. Rivière, I. Bonnet, F. Graner, and Y. Bellaïche. Modulation of junction tension by tumor suppressors and proto-oncogenes regulates cell-cell contacts. *Development*, 143(4):623–634, 2016.

[9] K. Brakke. The surface evolver. *Exp. Math.*, 1:141–152, 1992.

[10] K. A. Brakke. 200,000,000 random voronoi polygons. 1986.

[11] L. Bressy, P. Hebraud, V. Schmitt, and J. Bibette. Rheology of emulsions stabilized by solid interfaces. *Langmuir*, 19(3):598–604, 2003.

[12] D. Buzza, C.-Y. Lu, and M. Cates. Linear shear rheology of incompressible foams. *Journal de Physique II*, 5(1):37–52, 1995.

[13] I. Cantat. Gibbs elasticity effect in foam shear flows: a non quasi-static 2d numerical simulation. *Soft Matter*, 7(2):448–455, 2011.

[14] I. Cantat, N. Kern, and R. Delannay. Dissipation in foam flowing through narrow channels. *EPL (Europhysics Letters)*, 65(5):726, 2004.

[15] I. Cantat, S. Cohen-Addad, F. Elias, F. Graner, R. Höhler, O. Pitois, F. Rouyer, and A. Saint-Jalmes. *Foams: structure and dynamics*. OUP Oxford, 2013.

[16] D. Carugo, D. N. Ankrett, X. Zhao, X. Zhang, M. Hill, V. O'Byrne, J. Hoad, M. Arif, D. D. Wright, and A. L. Lewis. Benefits of polidocanol endovenous microfoam (varithena®) compared with physician-compounded foams. *Phlebology*, 31(4):283–295, 2016.

[17] S. Cohen-Addad, H. Hoballah, and R. Höhler. Viscoelastic response of a coarsening foam. *Physical Review E*, 57(6):6897, 1998.

[18] S. Cox and E. Whittick. Shear modulus of two-dimensional foams: The effect of area dispersity and disorder. *The European Physical Journal E*, 21(1):49–56, 2006.

[19] S. J. Cox. Simulations of bubble division in the flow of a foam past an obstacle in a narrow channel. *Colloids and Surfaces A: Physicochemical and Engineering Aspects*, 473:104–108, 2015.

[20] I. T. Davies and S. J. Cox. Sedimenting discs in a two-dimensional foam. *Colloids and Surfaces A: Physicochemical and Engineering Aspects*, 344(1-3):8–14, 2009.

[21] N. D. Denkov, V. Subramanian, D. Gurovich, and A. Lips. Wall slip and viscous dissipation in sheared foams: Effect of surface mobility. *Colloids and Surfaces A: Physicochemical and Engineering Aspects*, 263(1-3):129–145, 2005.

[22] T. Divoux, C. Barentin, and S. Manneville. Stress overshoot in a simple yield stress fluid: An extensive study combining rheology and velocimetry. *Soft Matter*, 7(19):9335–9349, 2011.

[23] W. Drenckhan, S. J. Cox, G. Delaney, H. Holste, D. Weaire, and N. Kern. Rheology of ordered foams—on the way to discrete microfluidics. *Colloids and Surfaces A: Physicochemical and Engineering Aspects*, 263(1):52–64, 2005.

[24] M. Durand. Statistical mechanics of two-dimensional foams: Physical foundations of the model. *The European Physical Journal E*, 38 (12):137, 2015.

[25] M. Durand and H. A. Stone. Relaxation time of the topological T1 process in a two-dimensional foam. *Physical Review Letters*, 97(22): 226101, 2006.

[26] D. J. Durian. Foam mechanics at the bubble scale. *Physical Review Letters*, 75(26):4780, 1995.

[27] D. A. Edwards, H. Brenner, and D. T. Wasan. *Interfacial transport processes and rheology*. Boston, 1991.

[28] R. Etournay, M. Popović, M. Merkel, A. Nandi, C. Blasse, B. Aigouy, H. Brandl, G. Myers, G. Salbreux, F. Jülicher, and S. Eaton. Interplay of cell dynamics and epithelial tension during morphogenesis of the drosophila pupal wing. *Elife*, 4:e07090, 2015.

[29] R. Farhadifar, J.-C. Röper, B. Aigouy, S. Eaton, and F. Jülicher. The influence of cell mechanics, cell-cell interactions, and proliferation on epithelial packing. *Current Biology*, 17(24):2095–2104, 2007.

[30] J. D. Ferry. *Viscoelastic properties of polymers*. John Wiley & Sons, 1980.

[31] H. Frost, C. Thompson, C. Howe, and J. Whang. A two-dimensional computer simulation of capillarity-driven grain growth: preliminary results. *Scripta Metallurgica*, 22(1):65–70, 1988.

[32] F. Graner and J. A. Glazier. Simulation of biological cell sorting using a two-dimensional extended potts model. *Physical Review Letters*, 69(13):2013, 1992.

[33] P. Grassia, C. Oguey, and R. Satomi. Relaxation of the topological T1 process in a two-dimensional foam. *The European Physical Journal E: Soft Matter and Biological Physics*, 35(7):1–12, 2012.

[34] P. Grassia, E. Mas-Hernández, N. Shokri, S. Cox, G. Mishuris, and W. Rossen. Analysis of a model for foam improved oil recovery. *Journal of Fluid Mechanics*, 751:346–405, 2014.

[35] C. Guillot and T. Lecuit. Mechanics of epithelial tissue homeostasis and morphogenesis. *Science*, 340(6137):1185–1189, 2013.

[36] C.-P. Heisenberg and Y. Bellaïche. Forces in tissue morphogenesis and patterning. *Cell*, 153(5):948–962, 2013.

[37] R. Höhler and S. Cohen-Addad. Rheology of liquid foam. *Journal of Physics: Condensed Matter*, 17(41):R1041, 2005.

[38] L. Hufnagel, A. A. Teleman, H. Rouault, S. M. Cohen, and B. I. Shraiman. On the mechanism of wing size determination in fly development. *Proceedings of the National Academy of Sciences*, 104 (10):3835–3840, 2007.

[39] M. S. Hutson, Y. Tokutake, M.-S. Chang, J. W. Bloor, S. Venakides, D. P. Kiehart, and G. S. Edwards. Forces for morphogenesis investigated with laser microsurgery and quantitative modeling. *Science*, 300(5616):145–149, 2003.

[40] S. Hutzler, D. Weaire, A. Saugey, S. J. Cox, and N. Peron. The physics of foam drainage. In *Proceedings of MIT European Detergents Conference, Wurzburg*, pages 191–206. Citeseer, 2005.

[41] Y. Jiang, P. J. Swart, A. Saxena, M. Asipauskas, and J. A. Glazier. Hysteresis and avalanches in two-dimensional foam rheology simulations. *Physical Review E*, 59(5):5819, 1999.

[42] A. Kabla and G. Debrégeas. Local stress relaxation and shear banding in a dry foam under shear. *Physical Review Letters*, 90(25): 258303, 2003.

[43] T. Kähärä, T. Tallinen, and J. Timonen. Numerical model for the shear rheology of two-dimensional wet foams with deformable bubbles. *Physical Review E*, 90(3):032307, 2014.

[44] J. Kermode and D. Weaire. 2d-froth: a program for the investigation of 2-dimensional froths. *Computer Physics Communications*, 60(1): 75–109, 1990.

[45] N. Kern, D. Weaire, A. Martin, S. Hutzler, and S. J. Cox. Two-dimensional viscous froth model for foam dynamics. *Physical Review E*, 70(4):041411, 2004.

[46] S. A. Khan, C. A. Schnepper, and R. C. Armstrong. Foam rheology: III. measurement of shear flow properties. *Journal of Rheology*, 32 (1):69–92, 1988.

[47] A. M. Kraynik, D. A. Reinelt, and F. van Swol. Structure of random foam. *Physical Review Letters*, 93(20):208301, 2004.

[48] V. J. Langlois, S. Hutzler, and D. Weaire. Rheological properties of the soft-disk model of two-dimensional foams. *Physical Review E*, 78(2):021401, 2008.

[49] R. G. Larson. *The Structure and Rheology of Complex Fluids*. Oxford University Press: New York, 1999.

[50] T. Lecuit and P.-F. Lenne. Cell surface mechanics and the control of cell shape, tissue patterns and morphogenesis. *Nature reviews Molecular cell biology*, 8(8):633, 2007.

[51] X. Liu and J. H. Duncan. The effects of surfactants on spilling breaking waves. *Nature*, 421(6922):520, 2003.

[52] P. Marmottant and F. Graner. An elastic, plastic, viscous model for slow shear of a liquid foam. *The European Physical Journal E*, 23 (4):337–347, 2007.

[53] P. Marmottant and F. Graner. Plastic and viscous dissipations in foams: cross-over from low to high shear rates. *Soft Matter*, 9(40): 9602–9607, 2013.

[54] R. Miller, V. Fainerman, M. Leser, and M. Michel. Kinetics of adsorption of proteins and surfactants. *Current opinion in colloid & interface science*, 9(5):350–356, 2004.

[55] T. Okuzono and K. Kawasaki. Intermittent flow behavior of random foams: a computer experiment on foam rheology. *Physical Review E*, 51(2):1246, 1995.

[56] D. Peng, J. Yang, J. Li, C. Tang, and B. Li. Foams stabilized by β-lactoglobulin amyloid fibrils: Effect of pH. *Journal of Agricultural and Food Chemistry*, 65(48):10658–10665, 2017.

[57] H. Princen and A. Kiss. Rheology of foams and highly concentrated emulsions: IV. an experimental study of the shear viscosity and yield stress of concentrated emulsions. *Journal of Colloid and Interface Science*, 128(1):176–187, 1989.

[58] C. Quilliet, S. Ataei Talebi, D. Rabaud, J. Kaefer, S. J. Cox, and F. Graner. Topological and geometrical disorders correlate robustly in two-dimensional foams. *Philosophical Magazine Letters*, 88(9-10): 651–660, 2008.

[59] C. Raufaste, B. Dollet, S. J. Cox, Y. Jiang, and F. Graner. Yield drag in a two-dimensional foam flow around a circular obstacle: Effect of liquid fraction. *The European Physical Journal E*, 23(2):217–228, 2007.

[60] C. Raufaste, S. J. Cox, P. Marmottant, and F. Graner. Discrete rearranging disordered patterns: Prediction of elastic and plastic

behavior, and application to two-dimensional foams. *Physical Review E*, 81(3):031404, 2010.

[61] M. Rauzi and P.-F. Lenne. Cortical forces in cell shape changes and tissue morphogenesis. In *Current topics in developmental biology*, volume 95, pages 93–144. Elsevier, 2011.

[62] M. Rauzi, P. Verant, T. Lecuit, and P.-F. Lenne. Nature and anisotropy of cortical forces orienting drosophila tissue morphogenesis. *Nature cell biology*, 10(12):1401, 2008.

[63] D. A. Reinelt and A. M. Kraynik. Simple shearing flow of a dry kelvin soap foam. *Journal of Fluid Mechanics*, 311:327–343, 1996.

[64] F. Rouyer, S. Cohen-Addad, R. Höhler, P. Sollich, and S. Fielding. The large amplitude oscillatory strain response of aqueous foam: Strain localization and full stress fourier spectrum. *The European Physical Journal E*, 27(3):309–321, 2008.

[65] D. K. Sarker and P. J. Wilde. Restoration of protein foam stability through electrostatic propylene glycol alginate-mediated protein–protein interactions. *Colloids and Surfaces B: Biointerfaces*, 15(3-4): 203–213, 1999.

[66] R. Satomi, P. Grassia, S. J. Cox, G. Mishuris, and L. Lue. Diffusion of curvature on a sheared semi-infinite film. *Proc. R. Soc. A*, 469 (2159):20130359, 2013.

[67] R. Satomi, P. Grassia, and C. Oguey. Modelling relaxation following T1 transformations of foams incorporating surfactant mass transfer

by the Marangoni effect. *Colloids and Surfaces A: Physicochemical and Engineering Aspects*, 438:77–84, 2013.

[68] L. Schwartz and H. Princen. A theory of extensional viscosity for flowing foams and concentrated emulsions. *Journal of Colloid and Interface Science*, 118(1):201–211, 1987.

[69] K. Sugimura, P.-F. Lenne, and F. Graner. Measuring forces and stresses in situ in living tissues. *Development*, 143(2):186–196, 2016.

[70] V. Ulaganathan, I. Retzlaff, J. Won, G. Gochev, D. Gunes, C. Gehin-Delval, M. Leser, B. Noskov, and R. Miller. β-lactoglobulin adsorption layers at the water/air surface. 2 Dilational rheology: Effect of pH and ionic strength. *Colloids and Surfaces A: Physicochemical and Engineering Aspects*, 521:167–176, 2017.

[71] D. Weaire and S. Hutzler. *The physics of foams*. Oxford University Press, 2001.

[72] J. Wejchert, D. Weaire, and J. Kermode. Monte Carlo simulation of the evolution of a two-dimensional soap froth. *Philosophical Magazine B*, 53(1):15–24, 1986.

[73] A. Wyn, I. T. Davies, and S. J. Cox. Simulations of two-dimensional foam rheology: localization in linear couette flow and the interaction of settling discs. *The European Physical Journal E*, 26(1-2):81–89, 2008.

[74] F. Zaccagnino, A. Audebert, and S. J. Cox. Simulation of surfactant transport during the rheological relaxation of two-dimensional dry foams. *Phys. Rev. E*, 98:022801, 2018.

Acknowledgements

I would like to thank the Prof. Simon Cox for supervising my work and for being always kindly available for discussions. I'm also grateful to the Prof. Gennady Mishuris and to the Aberystwyth University for giving me the incredible opportunity to get this doctorate.

I thank my siblings Angelo and Silvia whose strength and determination are inspiring for me and my friends who are always able to support me despite the distance. I'm grateful for all the gifts that Aberystwyth gave me, starting from my partner Stephen, to the other beautiful human beings that I had the pleasure to meet.

Finally, just for completeness, I have to thank the sea and the Welsh land which donated me amazing landscapes enriching the quality of my stay.